MACHINE LEARNING STRATEGIES TO ANALYZE QUANTITATIVE ULTRASOUND MULTI-PARAMETRIC IMAGES FOR PREDICTION OF THERAPY RESPONSE IN BREAST CANCER PATIENTS

HAMIDREZA TALEGHAMAR

A THESIS SUBMITTED TO
THE FACULTY OF GRADUATE STUDIES
IN PARTIAL FULFILLMENT OF REQUIREMENTS
FOR THE DEGREE OF
MASTER OF SCIENCE

GRADUATE PROGRAM IN
ELECTRICAL ENGINEERING & COMPUTER SCIENCE
YORK UNIVERSITY
TORONTO, ONTARIO

April 2021

Abstract

In this thesis project, two novel machine learning strategies were investigated to predict tumor response to neoadjuvant chemotherapy (NAC) at pre-treatment using quantitative ultrasound (QUS) multi-parametric images. The ultrasound data for analytical development and evaluation of the methodologies investigated in this project were acquired from 181 patients diagnosed with locally advanced breast cancer (LABC) and planned for NAC followed by surgery. The QUS multi-parametric images were generated using spectral analyses on the raw ultrasound radiofrequency (RF) data acquired before starting the NAC. In the first machine learning approach investigated in this project, distinct intra-tumor regions were identified within the parametric maps using a hidden Markov random field (HMRF) and its expectation-maximization (EM) algorithm. Several hand-crafted features characterizing the tumor, intra-tumor regions, and the tumor margin were extracted from different parametric images. A multi-step feature selection procedure was applied to construct a QUS biomarker for response prediction. Evaluation results on an independent test set indicated that the developed biomarker using the characteristics of intra-tumor regions and tumor margin in conjunction with a decision tree model with adaptive boosting (AdaBoost) as the classifier could predict the treatment response of patients at pre-treatment with an accuracy of 85.4% and an area under the receiver operating characteristic (ROC) curve (AUC) of 0.89. In the second machine learning approach investigated in this project, two deep convolutional neural network (DCNN) architectures including the residual network (ResNet) and residual attention network (RAN) were explored for extracting optimal feature maps from the parametric images, with a fully connected network for response prediction. Results demonstrated

that the developed model with the RAN architecture to extract feature maps from the expanded parametric images of the tumor core and margin had a superior performance with an accuracy of 0.88 and an AUC of 0.86 on the independent test set. Also, survival analysis demonstrated a statistically significant difference between survival curves of the two response cohorts identified at pre-treatment based on both the conventional machine learning method and the deep learning model. Obtained results in this study demonstrated a great promise of QUS multi-parametric imaging integrated with both unsupervised learning methods in identifying distinct breast cancer intra-tumor regions and traditional classification techniques, as well as deep convolutional neural networks in predicting tumor response to NAC prior to start of treatment.

Originality Statement

This thesis has been written by Hamidreza Taleghamar under supervision of Dr. Ali Sadeghi-Naini. Parts of the material presented in this thesis have been published in a peer-reviewed journal paper or are in preparation for submission in form of a journal paper, as listed below. The research presented in each publication has been performed by the principal author, supervised/supported by the senior author, and in collaboration with other co-authors who participated in project design and/or data acquisition/preprocessing.

- The material in Chapter 2 has been presented in: H. Taleghamar, H. Moghadas-Dastjerdi, G. J. Czarnota, and Ali Sadeghi-Naini. *Characterizing intra-tumor regions on quantitative ultrasound parametric images to predict breast cancer response to chemotherapy at pre-treatment.* Scientific Reports, vol. 11, 14865, 2021.

- The material in Chapter 3 has been presented in: H. Taleghamar, A. Jalalifar, G. J. Czarnota, and Ali Sadeghi-Naini. *Deep learning of quantitative ultrasound multi-parametric images at pre-treatment to predict breast cancer response to chemotherapy.* Manuscript in preparation for submission, 2021.

Acknowledgements

I would like to acknowledge everyone who played a role in my academic accomplishments. First I would like to express my deep gratitude to my supervisor, Dr. Ali Sadeghi Naini, who directed and supported all the research work on my thesis. Also, special thanks go to Dr. Tzerpos and Dr. Tabatabaei for serving on my examining committee. Moreover, I would like to thank other lab members Shirin Saednia, Seyed Ali Jalalifar, and Hadi Moghadas for their help.

Lastly, this thesis is dedicated to my parents for their endless love, support, and encouragement.

Table of Contents

List of Tables

List of Figures

Chapter 1

Introduction

1.1. Breast Cancer

1.1.1. Breast Cancer, Diagnosis and Treatment

Breast cancer is the most frequent cancer and the leading cause of cancer-related death among women [1]. In the United States, one in 8 women will be diagnosed with breast cancer in her lifetime, and about 25% of all new cancer cases diagnosed among women annually is breast cancer [2], [3]. Breast cancer can be detected through screening using different imaging modalities including x-ray mammography, ultrasound, and magnetic resonance imaging (MRI). The gold standard approach for breast cancer diagnosis is histopathological assessment of biopsy specimens. Once a cancer diagnosis is confirmed, the stage and condition of the disease will be determined using diagnostic information from imaging, histopathology, and other clinical examinations, and an appropriate treatment process would be prescribed, accordingly.

A crucial part of planning an effective treatment for each patient is cancer staging which is defined as the process of examining the condition and properties of the breast tumor and checking whether the cancer has spread to the other part of body. The breast cancer stage is determined based on multiple factors including the size and location of the primary tumor, and degree of cancer spread.

The most common system used for staging tumor is TNM system [4]. In the TNM staging system, three characteristics of disease which TNM stands for, determine the stage:

T: Tumor (The size and extend of the tumor)

N: Lymph Node (The number, size and location of the lymph nodes where cancer has spread)

M: Metastasis (Checking the spread of cancer to other parts of body)

The tumor grading system is another system used to assess tumor condition and it shows how quickly a breast tumor is likely to grow and spread. In this system cancer cells are examined to determine how similar they are to normal cells and how fast they grow compared to normal cells [5].

Also, breast cancer cells are tested to see if they have certain proteins including the estrogen or progesterone receptors. Breast cancer cells may have one, both, or none of these receptors that attach to the estrogen and progesterone hormones, and signal the cells to grow [6]. Breast cancers that have estrogen receptors are called ER-positive (ER+). Breast cancers with progesterone receptors are called PR-positive (PR+). Based on the hormone receptor status, hormone therapy can be used to either lower the hormone levels or stop them from acting on breast cancer cells [7]. Also, breast cells are tested to check the level of human epidermal growth factor receptor 2 (HER2) protein on breast tumor cells. HER2 is a growth-promoting protein on the breast cells, and breast cancer cells with higher than normal levels of HER2 are called HER2-positive. The cancer cells identified as HER-positive tend to grow and spread faster than other breast cancers, and they are much more likely to respond to treatment with drugs that target the HER2 protein [8].

After examining and staging breast cancer the treatment process will be planned and prescribed by clinicians. In general, there are five treatment options for breast cancer patients including surgery, radiation therapy, hormone therapy, chemotherapy, and targeted therapy, and mostly a combination of these treatments are prescribed for patients [9]. Some treatments including radiation therapy and targeted therapy are local and they target only the area around the tumor, and other treatments like chemotherapy and hormone therapy are systemic which target the cancerous cells in whole body with anti-cancer agents.

Chemotherapy is a drug treatment used to destroy cancer cells or slow down the growth of disease cells [10]. Chemotherapy is offered to most patients based on the cancer stage and tumor examination in conjunction with other treatment methods such as hormonal and targeted therapies [11]. Also, chemotherapy can be used prior to surgical resection with the goal of making the tumor operable, or shrinking and down-staging it before surgery, and in this case it is called neoadjuvant chemotherapy (NAC).

Another treatment option for breast cancer is radiation therapy that uses high-energy radiation beams to destroy cancer cells [9]. Radiation therapy is considered as a local treatment and only affects cells in the part of the body that is treated with radiation. Also, it can be used to eliminate any remaining cancer cells that remain in the breast area after the surgery in order to reduce the risk of cancer recurring or metastasis [12].

Hormone therapy is another type of treatment for breast cancer patients [9]. Glands such as gonads and adrenals produce hormones like estrogen and progesterone to help body regulation. However, sometimes these hormones can cause cancer cells to grow and spread faster. In this case, the pathologist will examine the breast cancer cells to determine if they have certain receptors that feed on estrogen or progesterone, stimulating their growth. If the cancer cells have these receptors, the doctor may prescribe hormone therapy drugs, such as blockers or inhibitors in order to destroy cancer cells or reduce their growth by removing their supply of hormones.

Targeted therapy is a relatively new treatment option for breast cancer [13]. The targeted drugs administrated in this treatment can attack specifically the breast cancer cells with minimal harm to normal cells. Breast cancer targeted therapy uses drugs that target specific parts of cancer cells, such as proteins or genes that help cancers grow and spread, in specific ways like blocking the

action of an growth-promoting protein like HER2 that stimulates the growth of breast cancer cells [13].

1.1.2. Locally Advanced Breast Cancer (LABC)

LABC is an aggressive type of breast cancer and includes tumors with a size of greater than 5 cm, extensive regional lymph node involvement, or direct involvement of the skin or underlying chest wall [14]. Up to 20% of patients diagnosed with breast cancer annually present with LABC [15]. These patients suffer from poor prognosis, high risk of cancer relapse, and low survival rates.

In the past, mastectomy, adjuvant chemotherapy, and post mastectomy radiotherapy were the standard treatment for operable LABC patients [16]. Currently, neoadjuvant chemotherapy has become the preferred method of treatment for operable LABC in order to downstage the disease and shrink the tumor before surgery. Moreover, neoadjuvant chemotherapy is used for inoperable breast cancer to make the disease operable.

Whereas LABC response to NAC has demonstrated high correlations with overall survival [17], about 30% of LABC tumors do not respond to NAC and approximately 10-20% of them show a complete pathological response [15]. Response of LABC tumors to NAC is currently evaluated at the end of the several months of chemotherapy based on changes in tumors dimensions using anatomical imaging as well as histopathology on surgical specimens [14]. Early prediction of LABC tumors response to NAC can facilitate adjusting standard treatments for individual patients. There have been several studies that showed treatment modification and switching to more effective treatment procedure can improve disease-free survival [18], [19]. A personalized paradigm for LABC treatment is expected to improve patient response to neoadjuvant therapies, to spare patients from unnecessary side effect of ineffective treatment, and to improve their overall survival and quality of life.

In biological studies, it has been shown that immunohistochemical markers such as Ki-67, human epithelial growth factor receptor 2 (HER2) and circulating tumor nucleosomes could be correlated to the likelihood of breast tumors response to NAC prior to the start of treatment [20]–[22]. A number of other studies have demonstrated that circulating tumors DNA and RNA-integrity measurements [23] as well as functional imaging methods including diffuse optical imaging (DOI) [24], MRI [25] and positron emission tomography (PET) [26] have the potential of predicting the treatment response early after the start of chemotherapy. These methods are associated with a number of limitations. Assessing for molecular, genomic and proteomic markers requires invasive acquisition of tissue samples that is not always feasible or practical, and needs processing equipment that is not always accessible. The functional imaging methods mentioned above are relatively expensive, require long scan times, and usually need injection of contrast agent that restrict their application in therapy response prediction/monitoring.

1.2. Imaging in Breast Cancer Management

Different imaging modalities are used in breast cancer management for disease detection, characterization and staging, and therapy outcome evaluation. Each of these modalities has its own advantages and limitations that make them appropriate for different applications. In this section, several modalities including MRI, mammography, PET and ultrasound imaging that are routinely applied in breast cancer management are described.

In MRI, a strong static magnetic field is applied to make hydrogen protons in the body aligning with the field. By emitting a radiofrequency pulse, the hydrogen protons are stimulated and spin out of equilibrium, straining against the pull of the magnetic field. Subsequently, when the

radiofrequency field is turned off, the receiver coils detect the energy released as the protons realign with the magnetic field. The time it takes for the protons to realign with the magnetic field, as well as the amount of energy released, is dependent on the environment and chemical characterization. Physicians can identify differences between various types of tissues based on these magnetic properties. For breast imaging often gadolinium contrast enhanced MRI is used to detect tumors which has a high sensitivity for the detection of breast cancer [27].

MRI plays an important role in breast cancer screening and diagnosis [28], [29]. Moreover, the potential of MRI in therapy response prediction has been investigated in several studies [30]–[32]. It has been shown that features derived from intra-tumor regions on magnetic resonance (MR) images of the breast cancer could be used for chemotherapy response prediction [33]. Also, it has been demonstrated that texture features extracted from MR images carry valuable information for response prediction [34]. Nevertheless, MRI has some limitations that should be considered while being used. People with implants particularly those containing ferromagnetic materials should not enter an MRI machine. Also, injection of imaging contrast agents may have adverse side effects in some cases [35].

X-ray mammography is commonly used for breast cancer screening [28], [36]. In mammography, after securing patient's breast within two compression plates, an x-ray machine emits a burst of x-rays that pass through the breast and received by a detector located on the opposite side. The produced images are called mammograms. On a mammogram, low density tissues such as fat, seem semi-transparent and darker, while areas of dense tissue like connective tissue or tumors look brighter. In some cases, mammograms are hard to interpret. For instance, dense breasts are more difficult to image and assess for tumor diagnosis [37]. In some cases that mammograms are not accurate enough other image modalities should be used for tumor screening [38].

PET is a nuclear medicine imaging technique to obtain 3D functional images of body. In PET imaging, a radionuclide contrast agent is injected to body that emits pairs of γ photons through β^+ radioactive decay. The γ photons are received and detected by the machine to generate the PET images. The radionuclides used in PET scans are made by attaching a radioactive atom to chemical substances that are used naturally by the particular organ or tissue during its metabolic process. PET scan can provide information about the chemical functions and metabolism inside the organs and tissues. Since the tumors have higher levels of metabolism compared to normal tissue, there is a good contrast between tumor and normal tissues in PET images. Potential of PET images for screening and diagnosing breast cancer have been explored in few studies [39], [40]. Also, PET scans have been used to predict treatment response in some cancer studies [26], [41], [42]. It should be considered that PET is very expensive, and its image resolution is not high. Furthermore, the patient is subjected to radiation exposure that may cause health risks.

Another imaging technique which is used for detecting breast lesions and cancer screening is ultrasound [28]. In order to produce ultrasound B-mode (brightness-mode) image, ultrasound pulses are produced by a transducer, which can both emit ultrasound pulses and detect the ultrasound echoes reflected back. As emitted ultrasound waves passes through tissues with different acoustic properties (echogenicity), partial energy of ultrasound pulses is reflected back to the probe in form of ultrasound echoes. Since the speed, direction, and distance the ultrasound pulses travel differ depending on the tissues micro-structure they run through, a computer can represent sonographic information of tissues as a two-dimensional image known as B-mode on the screen, while the brightness is controlled by the strength of the echo received from the tissue. For instance, the skin is highly reflective and appears as a bright line in the image, and fatty tissues cause low-level echoes and appear dark in the image. Also, by moving the transducer over the

breast, continuous real-time images can be captured. Ultrasound imaging can be used for other imaging applications including Doppler imaging [43] and elastography [44]. Ultrasound imaging has many advantages that make it a favorable modality for tumor screening and therapy response evaluation [45]. It is a safe, relatively inexpensive, portable, and rapid imaging modality that does not need injection of imaging contrast agents.

1.3. Quantitative Ultrasound

Quantitative ultrasound (QUS) techniques have been developed to derive quantitative measures that are independent of instrument and imaging parameters and with a lower level of operator dependence for tissue characterization applications [46]. The QUS techniques can be used in conjunction with sliding window analysis to generate color-coded parametric images that represent the underlying tissue characteristics [47]. The contrast in QUS parametric images is principally based on the underlying tissue's biophysical properties, and can give richer and more robust information about tissue micro-structure compared to the conventional B-mode images. Since different tissues consists of components with various shapes, spatial organization, and mechanical properties, QUS methods aim to estimate these properties using appropriate models and theory of how ultrasound interacts with soft tissues.

Initial studies on QUS developed basic theories to process ultrasound signals to obtain QUS parameters describing soft tissue properties and remove system dependence. In particular, Lizzi et al. [48] and Insana et al. [49] introduced QUS methods based on the backscatter coefficient. In addition, other QUS studies were performed which relied on measurement approaches not directly related to the backscatter coefficients. Some of these studies include using scanning acoustic

microscopy [50], inverse and forward scattering models of ultrasound tomography [51], and also envelope-statistics modeling and quantification [52]. QUS techniques have been used in several tissue characterization applications including prostate cancer diagnosis and characterization [53][54], monitoring chronic remodeling in liver tissue [55] and breast mass characterization [56]. Moreover, QUS has been used for monitoring tumor response to cancer treatments including radiation therapy [57], chemotherapy [58] and ultrasound-stimulated microbubble therapy [59]. In particular, these studies have demonstrated the association of QUS parameters and histology in different tissue characterization applications [46].

In order to estimate the QUS spectral and backscatter parameters, the mean power spectrum can be acquired by averaging the square magnitude of the fast Fourier transform (FFT) of window $e_s(t, x_i)$ through ultrasound radiofrequency (RF) lines, where $e_s(t, x_i)$ is defined as Hanning-gated RF echo segment as a function of time and lateral position. Next, the average power spectrum is normalized using the average power spectrum of a reference phantom with known attenuation coefficient within window $e_p(t, x_i)$ to remove the effects of system transfer functions and transducer beam-forming [60], [61]. The calculation of normalized power spectrum can be written as following:

$$P(f) = log \frac{\Sigma_i \left| FFT\left(e_s(t, x_i)\right)\right|^2}{\Sigma_i \left| FFT\left(e_p(t, x_i)\right)\right|^2} \qquad (1.1)$$

In the next step, through a linear regression analysis, the best fit line to the normalized power spectrum will be acquired within the -6 dB bandwidth centered at the transducer center frequency. The -6 dB bandwidth is estimated from the power spectrum of the reference phantom. Spectral slope (SS) and spectral intercept (SI) are the slope and extrapolated 0-MHz intercept of the line of

best fit, and midband fit (MBF) is the value of the line-approximated power spectrum at the center of the -6 dB frequency bandwidth (f_c). Therefore, SS, SI and MBF can be written as following:

$$P(f) = SS * f + SI \qquad (1.2)$$

$$MBF = P(f_c) \qquad (1.3)$$

The backscatter parameters including the effective scatterer diameter (ESD) and effective acoustic concentration (EAC) can be estimated by fitting a form factor model (e.g. spherical Gaussian model) to the backscatter coefficient (BSC) [62], [63]. BSC could be acquired as following:

$$\sigma_s(f) = P(f)\sigma_p(f)e^{4(\alpha_s-\alpha_p)\left(R+\frac{\Delta z}{2}\right)} \qquad (1.4)$$

where subscripts s and p indicate sample and reference phantom, respectively. α is the attenuation coefficient, Δz is the gate length, and R is the distance between the transducer and the proximal surface of the gate. The BSC of the reference phantom (σ_p) can be calculated by setting it as the sample in Equation (1.4) and setting the reference as another phantom characterized previously.

It has been demonstrated that QUS parametric images including those of MBF, SS and SI can be used for tissue characterization [64], [65]. Also, it has been shown that QUS parameters such as ESD and EAC can be related to the microscopic histological characteristics of the underlying tissue [66]. For example, it has been demonstrated that ESD is related to the average size of cellular structures in a study on two tumor phenotypes grown in animal models [56]. Another study by Banihashemi *et al.* suggested that there is a correlation between changes in the QUS parameters including MBF and SS and the histological variations in size of cell nuclei due to apoptosis [67].

Different Studies on QUS parametric maps of 58 and 30 patients have shown that QUS parameters including the MBF, SS, SI, and ESD have the potential of predicting breast tumor histopathology

responses to chemotherapy within few weeks after the therapy initiation [68][69]. Also, several studies demonstrated that textural features of QUS parametric maps which quantify the spatial relationship between local acoustic properties within the tissue, could be used for breast tumor characterization and response prediction [70][71][72]. Sannachi *et al*. have demonstrated that QUS in conjunction with textural analysis and molecular features could be applied to predict breast tumor response to chemotherapy early after treatment initiation [73]. A recent study demonstrated that the features extracted from the tumor margin in addition to the tumor core in QUS parametric maps of 56 patients could be used for chemotherapy response prediction at pre-treatment [74]. Byra et al. have demonstrated that segmented quantitative ultrasound maps could be utilized for distinguishing malignant versus benign lesions of breast [75]. In the chapter 2 of this thesis, we have adapted, for the first time, advanced clustering methods to segment intra-tumor regions in QUS multi-parametric images to quantify heterogeneity within the tumor for therapy response prediction.

1.4. Conventional Machine Learning Techniques for Medical Image Analysis and Classification

1.4.1. Image Processing and Segmentation Methods for Feature Extraction

An initial step in processing imaging data to use conventional machine learning methods for image classification is extracting appropriate features. These hand-crafted features should be defined in specific ways that represent important properties of the images. In classifying QUS parametric images, the mean value and signal to noise ratio (SNR) of the parametric image within a region of interest (ROI) are among the features that have been used for different tissue characterization applications [75], [76]. The SNR is acquired by calculating the ratio of the average pixel value to the standard deviation of pixel values within the ROI, as a measure of spatial heterogeneity [77].

In some studies on QUS, the features were acquired using texture analysis on parametric images [70], [73]. In order to acquire textural features, spatial distribution of QUS parameters in parametric maps can be quantified using statistical approaches including those based on the gray-level co-occurrence matrix (GLCM) [78]. A GLCM represents the angular relationship between neighboring pixels as well as their distances in an image. From a GLCM, different texture features such as contrast, correlation, homogeneity, and energy can be derived to quantify spatial patterns of heterogeneity in an image.

Another possible approach to characterize spatial heterogeneity in an image, *e.g.* a QUS parametric map, is to identify its distinct regions using segmentation methods [75]. Two popular clustering-based segmentation methods that can be utilized in this task include the k-means [79], and the Gaussian mixture model (GMM). These methods have been used in different applications in medical image segmentation [80], [81]. Also, k-means is commonly used as an initialization step in more complicated algorithms such as the hidden Markov random field-expectation maximization (HMRF-EM) (described in section 1.4.2). Concisely, the k-means clustering algorithms is as follows:

1. Determine the number of clusters *k*.
2. Initialize centroids by first shuffling the dataset and then randomly selecting *k* data points for the centroids without replacement.
3. Keep iterating the following steps until a stopping criterion is reached:
    - Compute the sum of the squared distance between data points and all centroids.
    - Assign each data point to the closest cluster (centroid).
    - Update the centroids for the clusters by taking the average of the all data points that belong to each cluster.

1.4.2. Hidden Markov Random Field - Expectation Maximization (HMRF-EM)

The HMRF-EM is an unsupervised classification method originally proposed for segmentation of brain MR images [82]. This method has been used for segmentation in several medical imaging analysis applications [83][84][85].

In HMRF-EM algorithm, for segmenting an image $x = (x_1, \ldots, x_N)$ where each x_i is the intensity of a pixel, we intend to find a configuration of labels $y = (y_1, \ldots, y_N)$ where $y_i \in L$ and L is the set of all possible labels with maximum a posteriori probability (MAP) estimation. Based on the MAP criteria, the estimated labels Y* should satisfy:

$$Y^* = argmax_x \{P(X|Y,\theta)P(Y)\} \qquad (1.5)$$

Where the prior probability $P(Y)$ is a Gibbs distribution and θ is representative of multivariate Gaussian distribution parameters which is obtained by the EM algorithm. Using joint likelihood probability, $P(X|Y,\theta)$ can be computed as:

$$P(X|Y,\theta) = \prod_i P(x_i|Y,\theta) = \prod_i P(x_i|y_i,\theta_i) \qquad (1.6)$$

Where $P(x_i|y_i,\theta_i)$ is a multivariate Gaussian distribution with parameters $\theta_{x_i} = (\mu_i, \Sigma_i)$, such that μ_i is the mean and Σ_i is the precision matrix of the distribution.

In order to find the intended labels, the following algorithm is followed [83]. First, the initial parameters and labels were estimated by applying a k-means algorithm on the image. Then, the following steps are performed iteratively until a stopping criterion is reached:

1. Compute the likelihood distribution $P^t(x_i|y_i,\theta_i)$ in iteration *t* starting from $t = 1$.
2. Use the current parameter set θ^t to estimate the labels by the MAP estimation algorithm [83].

3. Calculate the posterior distribution $P^t(l|x_i)$ for all the $l \in L$ and all pixels x_i utilizing the Bayesian rule.
4. Compute the updated parameter set θ^{t+1} with calculated posterior distribution $P^t(l|x_i)$.

1.4.3. Conventional Machine Learning Methods for Image Classification

During the past decades, several conventional machine learning methods have been introduced for classification using handcrafted features including those derived from medical images [86]. Different classification methods including the random forest [87], support vector machine (SVM) [88], and decision tree with adaptive boosting (AdaBoost) [89] showed decent performance in different applications in medical imaging analysis [86], [90].

In SVM algorithm, the goal is to find the hyperplane which separates the data into classes in an optimal way. First, closest points to the classifier hyperplane from both the classes are identified. These points are called support vectors. Then, the distance between the hyperplane and the support vectors would be computed. This distance is called the margin, and objective of the algorithm is to maximize the margin. The hyperplane for which the margin is maximum is the optimal hyperplane. Also SVM algorithms use a set of mathematical functions that are defined as the kernel. The function of kernel is to take data as input and transform it into another dimension which the data is more separable [91].

Random forest is another conventional machine learning method used for classification. Random forest builds multiple decision trees and fuses their output to get a more accurate and stable prediction. In random forest instead of searching for the most important feature while splitting a node, it searches for the best feature among a random subset of features which help model to avoid overfitting [91].

Adaboost uses the idea that a single classifier may not be able to accurately predict the class of an object, but when multiple weak classifiers are grouped with each one learning from the others' wrongly classified objects, one strong model can be built. In Adaboost model a sequence of weak learners are fitted on different weighted training data. It starts by predicting over the initial dataset and giving equal weight to each observation. If prediction is incorrect using the first learner, then the weight to observation which has been predicted incorrectly will increase. Also, each classifier is assigned with a weight based on the accuracy of the classifier, which means classifier with higher accuracy has more weight. Being an iterative process, it continues to add learner(s) until a limit is reached in the maximum iteration level or accuracy [91].

Larkin et al. [92] adapted the SVM model to classify whether a T2-weighted MRI image represents a treated tumor. Another study showed application of SVM in differentiating between “pre-” and “post-treatment” texton-based features acquired from QUS parametric images of preclinical data [93]. In a recent study, Tadayyon *et al.* [94] used SVM and KNN as classifier for chemotherapy response prediction prior to start of treatment on QUS images. Another study by Sannachi *et al.* [95], explored conventional machine learning methods including SVM and KNN for therapy response prediction early after the start of treatment using textural features acquired from QUS images. Moghadas-Dastjerdi *et al.* [96] have recently investigated different machine learning methods including SVM, random forest and Adaboost with decision tree as a weak learner for chemotherapy response prediction using CT images.

1.5. Deep Learning in Medical Image Analysis

Conventional machine learning methods like SVM and random forest use handcrafted features that should be extracted from medical images and processed to be used for classification. These methods use algorithms to learn from the extracted features and make informed decisions based on what they have learned. Therefore, appropriately defining distinctive features for each specific application is crucial in achieving a good performance in image classification with such models. On the other hand, deep learning methods, and specifically deep convolutional neural networks (DCNN), use a different approach to address image classification problems. As it is depicted in Figure 1.1, in these models the input image is sent through different processing layers, and the network layers hierarchically determines the specific features of the image that are appropriate for classification. The feature sets are optimized iteratively through the network training process [97]. The main advantage of deep learning methods is that they do not necessarily need structured features to classify image data. The DCNN models require minimal human intervention, as multilevel layers in the network ultimately learn from their own mistakes. However, since features are emerged from the data, a considerably large dataset would be required to let the model learn important features from the samples.

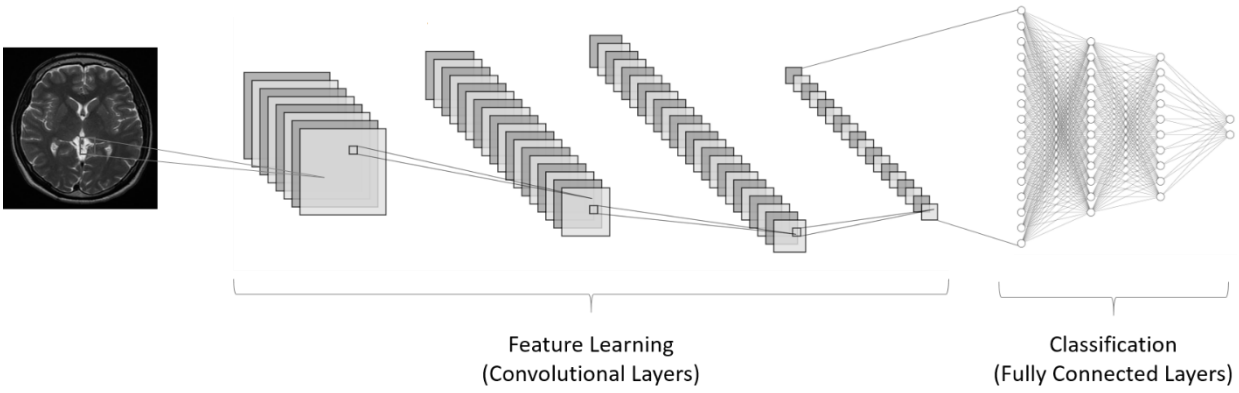

Figure 1.1. A convolutional neural network consists of convolutional layers and fully connected layers.

By introducing the AlexNet model in 2012, Krizhevsky *et al.* [98] showed that DCNNs can be highly effective in classifying high resolution images. DCNNs are able to successfully capture the spatial and temporal dependencies in an image through the application of relevant filters. The convolutional architecture showed significant performance on the image datasets with lower number of parameters involved and reusability of weights [99], [100].

During the last few years which DCNNs have shown promise in different tasks, several models including the residual networks (ResNet) [101], inception network [102], and the residual attention network (RAN) [103] have been introduced to improve the performance of deep learning models in image classification. The ResNet was introduced by He *et al.* [101] with a new concept to facilitate training the networks that are substantially deeper than those used previously. There has been some studies that argued adding more layer is crucial for improving the classification performance [99], [102]. But in practice, adding more layer to very deep neural networks can cause overfitting and reducing the performance of classification [104]. The core idea of ResNet is to introduce a so-called "identity shortcut connection" that skips one or more layers as is shown in Figure 1.2. The authors demonstrated that by using this architecture, stacking more layers will not degrade the network performance, because the network is able to skip the unnecessary layers, and the resulting architecture would perform better in classification tasks.

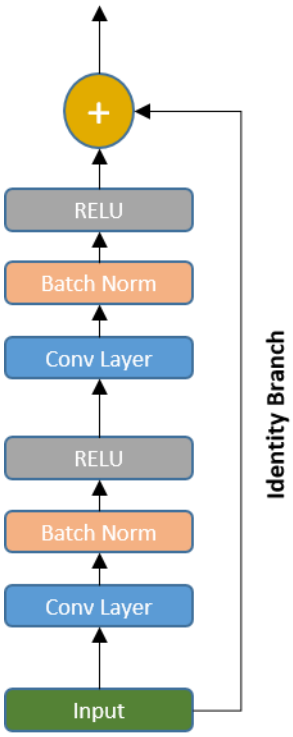

Figure 1.2. Residual unit.

The novelty incorporated in the RAN model was incorporating an attention module that is shown in Figure 1.3. The attention module in RAN consists of two branches - a “trunk” branch T(x) that is composed of two consecutive residual modules, and a mask branch M(x). The mask branch operates by down sampling an input patch using average pooling, passing through a residual module, down sampling again, computing another residual connection, and then finally upsampling to the original size using a bilinear interpolation and computing a sigmoid activation. The final output of this module can be written as:

$$F(x) = \big(1 + M(x)\big) * T(x) \qquad (1.7)$$

Adding one to the trunk operation allows for the trunk branch computation to pass through, where the mask branch works to suppress noise in the trunk branch, allowing for easier detection of important features. Therefore, only important features pass through the attention module.

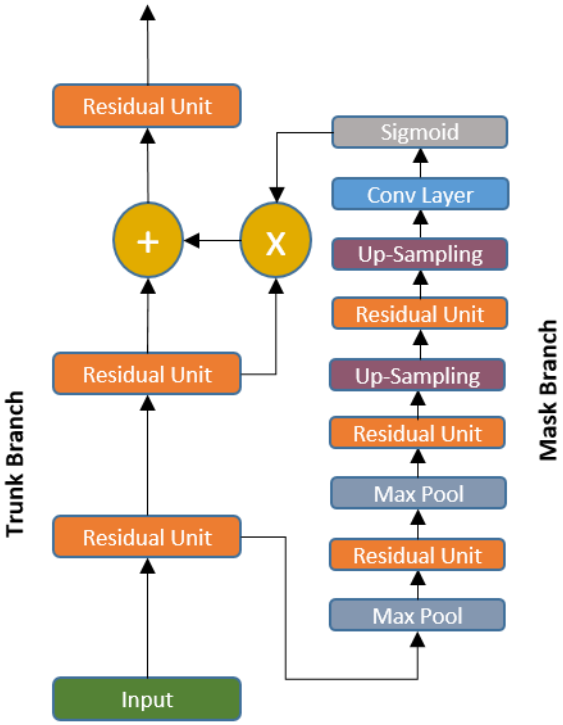

Figure 1.3. Attention unit.

The deep neural networks have recently been investigated in different applications of medical image analysis [105], [106]. A few studies have been conducted on adapting DCNNs for breast cancer therapy response prediction in breast cancer patients using MRI [107], [108]. Sloun *et al.* have recently reviewed different applications of deep learning on ultrasound imaging [109]. Byra *et al.* demonstrated the potential of convolutional neural networks for breast lesion classification using QUS Nakagami parametric images [110]. To the best of our knowledge no previous study has investigated the performance of applying DCNNs on QUS multi-parametric imaging for pre-treatment prediction of breast cancer response to NAC.

1.6. Contribution and Thesis Organization

In the recent years, few studies have been performed on analyzing QUS parametric images of breast tumors to predict therapy response prior to the start of treatment [74], [94]. These studies have focused on conventional machine learning methods with features derived from the parametric images of the entire tumor core and margin. In those studies, performance of QUS parameters for response prediction was assessed using a leave-one-patient-out cross-validation approach due to the relatively small cohorts applied and no independent test set were used for evaluation.

In this research, we have investigated different machine learning strategies to analyze QUS parametric images for prediction of LABC response to NAC at pre-treatment. Specifically, we investigated QUS parametric maps generated for more than 180 LABC patients using the ultrasound data acquired prior to their NAC. The obtained dataset were separated into separate training set and test set in order to have more robust and accurate evaluation. The proposed models were assessed using different criteria including accuracy, sensitivity, specificity, and area under the receiver operating characteristic (ROC) curve (AUC). Sensitivity (true positive rate) in this project refers to the ratio of the non-responses that was predicted as non-responder by the model. Similarly, specificity (true negative rate) refers to the ratio of the responders that was truly predicted by the model.

For response prediction, we explored two different approaches to analyze these parametric maps within the tumor core and its margin. In the first approach presented in Chapter 2 of this thesis, distinct intra-tumor regions were segmented within the parametric maps using a hidden Markov random field (HMRF) and its expectation-maximization (EM) algorithm. In the next step, quantitative features were extracted from the segmented intra-tumor regions. After feature

selection, AdaBoost was adapted and investigated in conjunction with the selected features for response prediction. We showed that AdaBoost has the best performance with an accuracy of 84.9% and an AUC of 0.89. For comparison, Adaboost predicted the treatment response with lower accuracy of 76.4% using features extracted from the unsegmented core and margin. Further, long-term survival analyses indicated that the patients predicted by the developed model as responders had a significantly better survival compared to the non-responders.

In the second approach presented in Chapter 3 of this thesis, we adapted and analyzed a number of different DCNN architectures for response prediction at pre-treatment using the QUS parametric maps. The main DCNN architectures investigated include the ResNet [101] and RAN [103] in conjunction with a fully connected neural network for response prediction. Potential of these architectures have been demonstrated in several applications in medical image classification [111], [112] that can possibly be extended to image-guided therapy response prediction [113]. Further, in a series of experiments we performed as a pilot study to find the best candidate models for response prediction, ResNet and RAN demonstrated superior performance in comparison to other well-known architectures including the Inception and Inception-ResNet [114], [115]. The results indicated the feature maps extracted from parametric maps of the core and margin using RAN architecture can predict the therapy response with accuracy of 87.5% and AUC of 0.86. Also, survival analysis indicated that there is a significant difference between survival curves of responders and non-responders identified based on both the model prediction at pre-treatment, and clinical criteria at post-treatment.

In Chapter 4 of the thesis, the acquired results are discussed and a number of future directions for extending this project are suggested.

References

[1] I. A. for R. on C. (IARC). WHO, "GLOBOCAN 2012: Estimated Cancer Incidence, Mortality and Prevalence Worldwide in 2012.," *Globocan*, pp. 1–6, 2012.

[2] C. DeSantis, J. Ma, L. Bryan, and A. Jemal, "Breast cancer statistics, 2013," *CA. Cancer J. Clin.*, vol. 64, no. 1, pp. 52–62, Jan. 2014, doi: 10.3322/caac.21203.

[3] H. Sung *et al.*, "Global cancer statistics 2020: GLOBOCAN estimates of incidence and mortality worldwide for 36 cancers in 185 countries," *CA. Cancer J. Clin.*, p. caac.21660, Feb. 2021, doi: 10.3322/caac.21660.

[4] H. Z. Montes, "TNM Classification of Malignant Tumors, 7th edition," *Int. J. Radiat. Oncol.*, vol. 78, no. 4, p. 1278, Nov. 2010, doi: 10.1016/j.ijrobp.2010.07.030.

[5] I. Damjanov, *Cancer Grading Manual*. Springer New York, 2007.

[6] L. K. Dunnwald, M. A. Rossing, and C. I. Li, "Hormone receptor status, tumor characteristics, and prognosis: A prospective cohort of breast cancer patients," *Breast Cancer Res.*, vol. 9, no. 1, pp. 1–10, Jan. 2007, doi: 10.1186/bcr1639.

[7] F. Rastelli and S. Crispino, "Factors predictive of response to hormone therapy in breast cancer," *Tumori*, vol. 94, no. 3, pp. 370–383, May 2008, doi: 10.1177/030089160809400314.

[8] Y. Yarden, "Biology of HER2 and Its Importance in Breast Cancer," *Oncology*, vol. 61, no. 2, pp. 1–13, 2001, doi: 10.1159/000055396.

[9] A. G. Waks and E. P. Winer, "Breast Cancer Treatment: A Review," *JAMA - Journal of the American Medical Association*, vol. 321, no. 3. American Medical Association, pp. 288–300, 22-Jan-2019, doi: 10.1001/jama.2018.19323.

[10] M. Perry, *The chemotherapy source book*. 2008.

[11] T. A. Moo, R. Sanford, C. Dang, and M. Morrow, "Overview of Breast Cancer Therapy," *PET Clinics*, vol. 13, no. 3. W.B. Saunders, pp. 339–354, 01-Jul-2018, doi: 10.1016/j.cpet.2018.02.006.

[12] T. A. Buchholz, "Radiation Therapy for Early-Stage Breast Cancer after Breast-Conserving Surgery," *N. Engl. J. Med.*, vol. 360, no. 1, pp. 63–70, Jan. 2009, doi: 10.1056/NEJMct0803525.

[13] A. Mohamed, K. Krajewski, B. Cakar, and C. X. Ma, "Targeted therapy for breast cancer," *American Journal of Pathology*, vol. 183, no. 4. Elsevier, pp. 1096–1112, 01-Oct-2013, doi: 10.1016/j.ajpath.2013.07.005.

[14] G. N. Hortobagyi, "Comprehensive management of locally advanced breast cancer.," *Cancer*, vol. 66, no. 6 Suppl, pp. 1387–91, Sep. 1990, doi: 10.1002/1097-0142(19900915)66:14+<1387::aid-cncr2820661414>3.0.co;2-i.

[15] S. H. Giordano, "Update on Locally Advanced Breast Cancer," *Oncologist*, vol. 8, no. 6, pp. 521–530, Dec. 2003, doi: 10.1634/theoncologist.8-6-521.

[16] M. R. Richard Hoppe, Theodore Phillips, "Leibel and Phillips Textbook of Radiation

Oncology," *Saunders*, 2010. .

[17] S. J. Cleator, A. Makris, S. E. Ashley, R. Lal, and T. J. Powles, "Good clinical response of breast cancers to neoadjuvant chemoendocrine therapy is associated with improved overall survival.," *Ann. Oncol. Off. J. Eur. Soc. Med. Oncol.*, vol. 16, no. 2, pp. 267–72, Feb. 2005, doi: 10.1093/annonc/mdi049.

[18] G. von Minckwitz *et al.*, "S3-2: Neoadjuvant Chemotherapy Adapted by Interim Response Improves Overall Survival of Primary Breast Cancer Patients – Results of the GeparTrio Trial.," in *Cancer Research*, 2011, vol. 71, no. 24 Supplement, pp. S3-2-S3-2, doi: 10.1158/0008-5472.sabcs11-s3-2.

[19] G. Von Minckwitz *et al.*, "Neoadjuvant vinorelbine-capecitabine versus docetaxel-doxorubicin- cyclophosphamide in early nonresponsive breast cancer: Phase III randomized gepartrio trial," *J. Natl. Cancer Inst.*, vol. 100, no. 8, pp. 542–551, Apr. 2008, doi: 10.1093/jnci/djn085.

[20] J. Chang, M. Ormerod, T. J. Powles, D. C. Allred, S. E. Ashley, and M. Dowsett, "Apoptosis and proliferation as predictors of chemotherapy response in patients with breast carcinoma.," *Cancer*, vol. 89, no. 11, pp. 2145–52, Dec. 2000.

[21] O. J. Stoetzer *et al.*, "Prediction of response to neoadjuvant chemotherapy in breast cancer patients by circulating apoptotic biomarkers nucleosomes, DNAse, cytokeratin-18 fragments and survivin," *Cancer Lett.*, vol. 336, no. 1, pp. 140–148, Aug. 2013, doi: 10.1016/j.canlet.2013.04.013.

[22] F. Andre *et al.*, "HER2 expression and efficacy of preoperative paclitaxel/FAC chemotherapy in breast cancer," *Breast Cancer Res. Treat.*, vol. 108, no. 2, pp. 183–190, Mar. 2008, doi: 10.1007/s10549-007-9594-8.

[23] H. Schwarzenbach and K. Pantel, "Circulating DNA as biomarker in breast cancer," *Breast Cancer Research*, vol. 17, no. 1. BioMed Central Ltd., p. 136, 09-Oct-2015, doi: 10.1186/s13058-015-0645-5.

[24] O. Falou *et al.*, "Diffuse optical spectroscopy evaluation of treatment response in women with locally advanced breast cancer receiving neoadjuvant chemotherapy," *Transl. Oncol.*, vol. 5, no. 4, pp. 238–246, 2012, doi: 10.1593/tlo.11346.

[25] J. R. Teruel *et al.*, "Dynamic contrast-enhanced MRI texture analysis for pretreatment prediction of clinical and pathological response to neoadjuvant chemotherapy in patients with locally advanced breast cancer," *NMR Biomed.*, vol. 27, no. 8, pp. 887–896, 2014, doi: 10.1002/nbm.3132.

[26] B. S. Pio *et al.*, "Usefulness of 3′-[F-18]fluoro-3′-deoxythymidine with positron emission tomography in predicting breast cancer response to therapy," *Mol. Imaging Biol.*, vol. 8, no. 1, pp. 36–42, Jan. 2006, doi: 10.1007/s11307-005-0029-9.

[27] R. M. Mann, C. K. Kuhl, and L. Moy, "Contrast-enhanced MRI for breast cancer screening," *Journal of Magnetic Resonance Imaging*, vol. 50, no. 2. John Wiley and Sons Inc., pp. 377–390, 01-Aug-2019, doi: 10.1002/jmri.26654.

[28] C. H. Lee *et al.*, "Breast Cancer Screening With Imaging: Recommendations From the Society of Breast Imaging and the ACR on the Use of Mammography, Breast MRI, Breast

Ultrasound, and Other Technologies for the Detection of Clinically Occult Breast Cancer," *Journal of the American College of Radiology*, vol. 7, no. 1. Elsevier, pp. 18–27, 01-Jan-2010, doi: 10.1016/j.jacr.2009.09.022.

[29] M. Morrow, J. Waters, and E. Morris, "MRI for breast cancer screening, diagnosis, and treatment," *The Lancet*, vol. 378, no. 9805. Lancet Publishing Group, pp. 1804–1811, 19-Nov-2011, doi: 10.1016/S0140-6736(11)61350-0.

[30] M. L. Marinovich *et al.*, "Early prediction of pathologic response to neoadjuvant therapy in breast cancer: Systematic review of the accuracy of MRI," *Breast*, vol. 21, no. 5, pp. 669–677, Oct. 2012, doi: 10.1016/j.breast.2012.07.006.

[31] M. Fan, G. Wu, H. Cheng, J. Zhang, G. Shao, and L. Li, "Radiomic analysis of DCE-MRI for prediction of response to neoadjuvant chemotherapy in breast cancer patients," *Eur. J. Radiol.*, vol. 94, pp. 140–147, Sep. 2017, doi: 10.1016/j.ejrad.2017.06.019.

[32] Y. Kim *et al.*, "Early prediction of response to neoadjuvant chemotherapy using dynamic contrast-enhanced mri and ultrasound in breast cancer," *Korean J. Radiol.*, vol. 19, no. 4, pp. 682–691, Jul. 2018, doi: 10.3348/kjr.2018.19.4.682.

[33] J. Wu, G. Gong, Y. Cui, and R. Li, "Intratumor partitioning and texture analysis of dynamic contrast-enhanced (DCE)-MRI identifies relevant tumor subregions to predict pathological response of breast cancer to neoadjuvant chemotherapy," *J. Magn. Reson. Imaging*, vol. 44, no. 5, pp. 1107–1115, Nov. 2016, doi: 10.1002/jmri.25279.

[34] G. Thibault *et al.*, "DCE-MRI Texture Features for Early Prediction of Breast Cancer Therapy Response," *Tomogr. (Ann Arbor, Mich.)*, vol. 3, no. 1, pp. 23–32, Mar. 2017, doi: 10.18383/j.tom.2016.00241.

[35] K. M. Hasebroock and N. J. Serkova, "Toxicity of MRI and CT contrast agents," *Expert Opin. Drug Metab. Toxicol.*, vol. 5, no. 4, pp. 403–416, Apr. 2009, doi: 10.1517/17425250902873796.

[36] P. C. Gøtzsche and K. J. Jørgensen, "Screening for breast cancer with mammography," *Cochrane Database of Systematic Reviews*, vol. 2013, no. 6. John Wiley and Sons Ltd, 04-Jun-2013, doi: 10.1002/14651858.CD001877.pub5.

[37] M. T. Mandelson, "Breast Density as a Predictor of Mammographic Detection: Comparison of Interval- and Screen-Detected Cancers," *J. Natl. Cancer Inst.*, vol. 92, no. 13, pp. 1081–1087, Jul. 2000, doi: 10.1093/jnci/92.13.1081.

[38] K. M. Kelly, J. Dean, W. S. Comulada, and S. J. Lee, "Breast cancer detection using automated whole breast ultrasound and mammography in radiographically dense breasts," *Eur. Radiol.*, vol. 20, no. 3, pp. 734–742, Mar. 2010, doi: 10.1007/s00330-009-1588-y.

[39] B. Zangheri, C. Messa, M. Picchio, L. Gianolli, C. Landoni, and F. Fazio, "PET/CT and breast cancer," *European Journal of Nuclear Medicine and Molecular Imaging*, vol. 31, no. SUPPL. 1. Springer Verlag, pp. S135–S142, 05-May-2004, doi: 10.1007/s00259-004-1536-7.

[40] H. Schöder and M. Gönen, "Screening for Cancer with PET and PET/CT: Potential and Limitations," *J. Nucl. Med.*, vol. 48, pp. 4–18, 2007.

[41] L. Fass, *Imaging and cancer: A review*, vol. 2, no. 2. Wiley-Blackwell, 2008, pp. 115–152.

[42] J. Czernin and M. E. Phelps, "Positron Emission Tomography Scanning: Current and Future Applications," *Annu. Rev. Med.*, vol. 53, no. 1, pp. 89–112, Feb. 2002, doi: 10.1146/annurev.med.53.082901.104028.

[43] C. M. Sehgal, P. H. Arger, S. E. Rowling, E. F. Conant, C. Reynolds, and J. A. Patton, "Quantitative vascularity of breast masses by Doppler imaging: Regional variations and diagnostic implications," *J. Ultrasound Med.*, vol. 19, no. 7, pp. 427–440, 2000, doi: 10.7863/jum.2000.19.7.427.

[44] J. L. Gennisson, T. Deffieux, M. Fink, and M. Tanter, "Ultrasound elastography: Principles and techniques," *Diagnostic and Interventional Imaging*, vol. 94, no. 5. Elsevier Masson SAS, pp. 487–495, 01-May-2013, doi: 10.1016/j.diii.2013.01.022.

[45] C. M. Sehgal, S. P. Weinstein, P. H. Arger, and E. F. Conant, "A review of breast ultrasound," *Journal of Mammary Gland Biology and Neoplasia*, vol. 11, no. 2. Springer, pp. 113–123, 04-Apr-2006, doi: 10.1007/s10911-006-9018-0.

[46] J. Mamou and M. L. Oelze, *Quantitative ultrasound in soft tissues*. Springer Netherlands, 2013.

[47] H. Tadayyon, A. Sadeghi-Naini, L. Wirtzfeld, F. C. Wright, and G. Czarnota, "Quantitative ultrasound characterization of locally advanced breast cancer by estimation of its scatterer properties," *Med. Phys.*, vol. 41, no. 1, p. 012903, Jan. 2014, doi: 10.1118/1.4852875.

[48] D. J. Coleman and F. L. Lizzi, "Computerized ultrasonic tissue characterization of ocular tumors," *Am. J. Ophthalmol.*, vol. 96, no. 2, pp. 165–175, Aug. 1983, doi: 10.1016/S0002-9394(14)77784-0.

[49] M. F. Insana and T. J. Hall, "Parametric Ultrasound Imaging from Backscatter Coefficient Measurements: Image Formation and Interpretation," *Ultrason. Imaging*, vol. 12, no. 4, pp. 245–267, 1990, doi: 10.1177/016173469001200402.

[50] Y. Saijo, "Recent applications of acoustic microscopy for quantitative measurement of acoustic properties of soft tissues," in *Quantitative Ultrasound in Soft Tissues*, Springer Netherlands, 2013, pp. 291–314.

[51] R. J. Lavarello and A. J. Hesford, "Methods for forward and inverse scattering in ultrasound tomography," in *Quantitative Ultrasound in Soft Tissues*, Springer Netherlands, 2013, pp. 345–394.

[52] F. Destrempes and G. Cloutier, "Review of envelope statistics models for quantitative ultrasound imaging and tissue characterization," in *Quantitative Ultrasound in Soft Tissues*, Springer Netherlands, 2013, pp. 219–274.

[53] E. J. E. Feleppa *et al.*, "Typing of prostate tissue by ultrasonic spectrum analysis," *IEEE Trans. Ultrason. Ferroelectr. Freq. Control*, vol. 43, no. 4, pp. 609–619, Jul. 1996, doi: 10.1109/58.503779.

[54] A. Sadeghi-Naini *et al.*, "Quantitative ultrasound spectroscopic imaging for characterization of disease extent in prostate cancer patients," *Transl. Oncol.*, vol. 8, no. 1, pp. 25–34, 2015, doi: 10.1016/j.tranon.2014.11.005.

[55] A. Guimond *et al.*, "Quantitative ultrasonic tissue characterization as a new tool for continuous monitoring of chronic liver remodelling in mice," *Liver Int.*, vol. 27, no. 6, pp.

854–864, Aug. 2007, doi: 10.1111/j.1478-3231.2007.01493.x.

[56] M. L. Oelze, W. D. O'Brien, J. P. Blue, and J. F. Zachary, "Differentiation and characterization of rat mammary fibroadenomas and 4T1 mouse carcinomas using quantitative ultrasound imaging," *IEEE Trans. Med. Imaging*, vol. 23, no. 6, pp. 764–771, Jun. 2004, doi: 10.1109/TMI.2004.826953.

[57] R. M. Vlad, S. Brand, A. Giles, M. C. Kolios, and G. J. Czarnota, "Quantitative ultrasound characterization of responses to radiotherapy in cancer mouse models," *Clin. Cancer Res.*, vol. 15, no. 6, pp. 2067–2075, Mar. 2009, doi: 10.1158/1078-0432.CCR-08-1970.

[58] A. Sadeghi-Naini *et al.*, "Low-frequency quantitative ultrasound imaging of cell death *in vivo*," *Med. Phys.*, vol. 40, no. 8, p. 082901, Jul. 2013, doi: 10.1118/1.4812683.

[59] H. C. Kim, A. Al-Mahrouki, A. Gorjizadeh, A. Sadeghi-Naini, R. Karshafian, and G. J. Czarnota, "Quantitative ultrasound characterization of tumor cell death: Ultrasound-stimulated microbubbles for radiation enhancement," *PLoS One*, vol. 9, no. 7, Jul. 2014, doi: 10.1371/journal.pone.0102343.

[60] Y. Labyed, T. A. Bigelow, and B. L. McFarlin, "Estimate of the attenuation coefficient using a clinical array transducer for the detection of cervical ripening in human pregnancy," *Ultrasonics*, vol. 51, no. 1, pp. 34–39, Jan. 2011, doi: 10.1016/j.ultras.2010.05.005.

[61] L. X. Yao, J. A. Zagzebski, and E. L. Madsen, "Backscatter coefficient measurements using a reference phantom to extract depth-dependent instrumentation factors," *Ultrason. Imaging*, vol. 12, no. 1, pp. 58–70, Jan. 1990, doi: 10.1016/0161-7346(90)90221-i.

[62] F. L. F. L. F. L. Lizzi *et al.*, "Comparison of theoretical scattering results and ultrasonic data from clinical liver examinations," *Ultrasound Med. Biol.*, vol. 14, no. 5, pp. 377–385, 1988, doi: 10.1016/0301-5629(88)90073-7.

[63] M. F. Insana *et al.*, "Describing small-scale structure in random media using pulse-echo ultrasound," *J. Acoust. Soc. Am.*, vol. 87, no. 1, pp. 179–192, Jan. 1990, doi: 10.1121/1.399283.

[64] M. Yang, T. M. Krueger, J. G. Miller, and M. R. Holland, "Characterization of anisotropic myocardial backscatter using spectral slope, intercept and midband fit parameters," *Ultrason. Imaging*, vol. 29, no. 2, pp. 122–134, Apr. 2007, doi: 10.1177/016173460702900204.

[65] J. Mamou *et al.*, "Three-dimensional high-frequency backscatter and envelope quantification of cancerous human lymph nodes," *Ultrasound Med. Biol.*, vol. 37, no. 3, pp. 345–357, Mar. 2011, doi: 10.1016/j.ultrasmedbio.2010.11.020.

[66] R. C. Waag, J. O. Nilsson, and J. P. Astheimer, "Characterization of volume scattering power spectra in isotropic media from power spectra of scattering by planes," *J. Acoust. Soc. Am.*, vol. 74, no. 5, pp. 1555–1571, Nov. 1983, doi: 10.1121/1.390063.

[67] B. Banihashemi, R. Vlad, B. Debeljevic, A. Giles, M. C. Kolios, and G. J. Czarnota, "Ultrasound imaging of apoptosis in tumor response: Novel preclinical monitoring of photodynamic therapy effects," *Cancer Res.*, vol. 68, no. 20, pp. 8590–8596, Oct. 2008, doi: 10.1158/0008-5472.CAN-08-0006.

[68] H. Tadayyon *et al.*, "Quantitative ultrasound assessment of breast tumor response to

chemotherapy using a multi-parameter approach," *Oncotarget*, vol. 7, no. 29, pp. 45094–45111, Jul. 2016, doi: 10.18632/oncotarget.8862.

[69] L. Sannachi *et al.*, "Non-invasive evaluation of breast cancer response to chemotherapy using quantitative ultrasonic backscatter parameters," *Med. Image Anal.*, vol. 20, no. 1, pp. 224–236, Feb. 2015, doi: 10.1016/j.media.2014.11.009.

[70] A. Sadeghi-Naini *et al.*, "Early prediction of therapy responses and outcomes in breast cancer patients using quantitative ultrasound spectral texture," *Oncotarget*, vol. 5, no. 11, pp. 3497–3511, 2014, doi: 10.18632/oncotarget.1950.

[71] H. Tadayyon, A. Sadeghi-Naini, and G. J. Czarnota, "Noninvasive characterization of locally advanced breast cancer using textural analysis of quantitative ultrasound parametric images," *Transl. Oncol.*, vol. 7, no. 6, pp. 759–767, 2014, doi: 10.1016/j.tranon.2014.10.007.

[72] A. Sadeghi-Naini *et al.*, "Breast-Lesion Characterization using Textural Features of Quantitative Ultrasound Parametric Maps," *Sci. Rep.*, vol. 7, no. 1, Dec. 2017, doi: 10.1038/s41598-017-13977-x.

[73] L. Sannachi *et al.*, "Response monitoring of breast cancer patients receiving neoadjuvant chemotherapy using quantitative ultrasound, texture, and molecular features," *PLoS One*, vol. 13, no. 1, p. e0189634, Jan. 2018, doi: 10.1371/journal.pone.0189634.

[74] H. Tadayyon *et al.*, "A priori Prediction of Neoadjuvant Chemotherapy Response and Survival in Breast Cancer Patients using Quantitative Ultrasound," *Sci. Rep.*, vol. 7, Apr. 2017, doi: 10.1038/srep45733.

[75] M. Byra, A. Nowicki, H. Wróblewska-Piotrzkowska, and K. Dobruch-Sobczak, "Classification of breast lesions using segmented quantitative ultrasound maps of homodyned K distribution parameters," *Med. Phys.*, vol. 43, no. 10, pp. 5561–5569, Oct. 2016, doi: 10.1118/1.4962928.

[76] A. Sadeghi-Naini *et al.*, "Chemotherapy-Response Monitoring of Breast Cancer Patients Using Quantitative Ultrasound-Based Intra-Tumour Heterogeneities," *Sci. Rep.*, vol. 7, no. 1, Dec. 2017, doi: 10.1038/s41598-017-09678-0.

[77] R. F. Wagner, S. W. Smith, J. M. Sandrik, and H. Lopez, "Statistics of Speckle in Ultrasound B-Scans," *IEEE Trans. Sonics Ultrason.*, vol. 30, no. 3, pp. 156–163, 1983, doi: 10.1109/T-SU.1983.31404.

[78] R. M. Haralick, I. Dinstein, and K. Shanmugam, "Textural Features for Image Classification," *IEEE Trans. Syst. Man Cybern.*, vol. SMC-3, no. 6, pp. 610–621, 1973, doi: 10.1109/TSMC.1973.4309314.

[79] J. MacQueen, "Some methods for classification and analysis of multivariate observations." The Regents of the University of California, 1967.

[80] H. P. Ng, S. H. Ong, K. W. C. Foong, P. S. Goh, and W. L. Nowinski, "Medical image segmentation using k-means clustering and improved watershed algorithm," in *Proceedings of the IEEE Southwest Symposium on Image Analysis and Interpretation*, 2006, vol. 2006, pp. 61–65, doi: 10.1109/ssiai.2006.1633722.

[81] H. Greenspan and A. T. Pinhas, "Medical image categorization and retrieval for PACS using

the GMM-KL framework," *IEEE Trans. Inf. Technol. Biomed.*, vol. 11, no. 2, pp. 190–202, Mar. 2007, doi: 10.1109/TITB.2006.874191.

[82] Li S.Z. (1994) Markov random field models in computer vision. In: Eklundh JO. (eds) Computer Vision — ECCV '94. ECCV 1994. Lecture Notes in Computer Science, vol 801. Springer, Berlin, Heidelberg. https://doi.org/10.1007/BFb0028368

[83] Q. Wang, "GMM-Based Hidden Markov Random Field for Color Image and 3D Volume Segmentation," Dec. 2012.

[84] Y. Zhang, M. Brady, and S. Smith, "Segmentation of brain MR images through a hidden Markov random field model and the expectation-maximization algorithm," *IEEE Trans. Med. Imaging*, vol. 20, no. 1, pp. 45–57, Jan. 2001, doi: 10.1109/42.906424.

[85] T. Ben Saïd, F. Chaieb, S. M'Hiri, F. Ghorbel, and O. Azaiz, "Segmentation of liver tumor using HMRF-EM algorithm with Bootstrap resampling," in *2010 5th International Symposium on I/V Communications and Mobile Networks, ISIVC 2010*, 2010, doi: 10.1109/ISVC.2010.5656429.

[86] B. J. Erickson, P. Korfiatis, Z. Akkus, and T. L. Kline, "Machine learning for medical imaging," *Radiographics*, vol. 37, no. 2, pp. 505–515, Mar. 2017, doi: 10.1148/rg.2017160130.

[87] L. Breiman, "Random forests," *Mach. Learn.*, vol. 45, no. 1, pp. 5–32, Oct. 2001, doi: 10.1023/A:1010933404324.

[88] C. Cortes, "Support-Vector Networks," *Mach Learn*, vol. 20, pp. 273–297, 1995.

[89] Y. Freund, "Boosting a weak learning algorithm by majority," *Inf. Comput.*, vol. 121, no. 2, pp. 256–285, 1995, doi: 10.1006/inco.1995.1136.

[90] D. Shen, G. Wu, D. Zhang, and K. Suzuki, "Machine learning in medical imaging," *Springer*, 2015.

[91] S. Shalev-Shwartz and S. Ben-David, *Understanding machine learning: From theory to algorithms*. Cambridge University Press, 2013.

[92] T. J. Larkin *et al.*, "Analysis of image heterogeneity using 2D Minkowski functionals detects tumor responses to treatment," *Magn. Reson. Med.*, vol. 71, no. 1, pp. 402–410, Jan. 2014, doi: 10.1002/mrm.24644.

[93] M. J. Gangeh, A. Sadeghi-Naini, M. S. Kamel, and G. J. Czarnota, "Assessment of cancer therapy effects using texton-based characterization of quantitative ultrasound parametric images," in *Proceedings - International Symposium on Biomedical Imaging*, 2013, pp. 1372–1375, doi: 10.1109/ISBI.2013.6556788.

[94] H. Tadayyon *et al.*, "A priori prediction of breast tumour response to chemotherapy using quantitative ultrasound imaging and artificial neural networks," *Oncotarget*, vol. 10, no. 39, pp. 3910–3923, 2019.

[95] D. Sethi, R. Sen, J. Sen, S. Parshad, S. Khetarpal, and M. Garg, "Histopathologic changes following neoadjuvant chemotherapy in various malignancies," *Int. J. Appl. Basic Med. Res.*, vol. 2, no. 2, p. 111, 2012, doi: 10.4103/2229-516x.106353.

[96] H. Moghadas-Dastjerdi, H. R. Sha-E-Tallat, L. Sannachi, A. Sadeghi-Naini, and G. J.

Czarnota, “A priori prediction of tumour response to neoadjuvant chemotherapy in breast cancer patients using quantitative CT and machine learning,” *Sci. Rep.*, vol. 10, no. 1, p. 10936, Dec. 2020, doi: 10.1038/s41598-020-67823-8.

[97] I. Goodfellow, Y. Bengio, A. Courville, and Y. Bengio, “Deep learning,” 2016, doi: 10.4258/hir.2016.22.4.351.

[98] Krizhevsky, Alex & Sutskever, Ilya & Hinton, Geoffrey, "ImageNet Classification with Deep Convolutional Neural Networks" *Neural Information Processing Systems 2012*. 25. 10.1145/3065386.

[99] K. Simonyan and A. Zisserman, “Very deep convolutional networks for large-scale image recognition,” *3rd Int. Conf. Learn. Represent. ICLR 2015 - Conf. Track Proc.*, Sep. 2015.

[100] R. Yang and Y. Yu, “Artificial Convolutional Neural Network in Object Detection and Semantic Segmentation for Medical Imaging Analysis,” *Front. Oncol.*, vol. 11, p. 638182, Mar. 2021, doi: 10.3389/fonc.2021.638182.

[101] K. He, X. Zhang, S. Ren, and J. Sun, “Deep residual learning for image recognition,” in *Proceedings of the IEEE Computer Society Conference on Computer Vision and Pattern Recognition*, 2016, vol. 2016-December, pp. 770–778, doi: 10.1109/CVPR.2016.90.

[102] C. Szegedy *et al.*, “Going deeper with convolutions,” in *Proceedings of the IEEE Computer Society Conference on Computer Vision and Pattern Recognition*, 2015, vol. 07-12-June, pp. 1–9, doi: 10.1109/CVPR.2015.7298594.

[103] F. Wang *et al.*, “Residual Attention Network for Image Classification,” *Proc. - 30th IEEE Conf. Comput. Vis. Pattern Recognition, CVPR 2017*, vol. 2017-January, pp. 6450–6458, Apr. 2017.

[104] K. He and J. Sun, “Convolutional Neural Networks at Constrained Time Cost,” *Proc. IEEE Comput. Soc. Conf. Comput. Vis. Pattern Recognit.*, vol. 07-12-June-2015, pp. 5353–5360, Dec. 2014.

[105] D. Shen, G. Wu, and H.-I. Suk, *Deep Learning in Medical Image Analysis*. Elsevier, 2017.

[106] G. Litjens *et al.*, “A survey on deep learning in medical image analysis,” *Medical Image Analysis*, vol. 42. Elsevier B.V., pp. 60–88, 01-Dec-2017, doi: 10.1016/j.media.2017.07.005.

[107] K. Ravichandran, N. Braman, A. Janowczyk, and A. Madabhushi, “A deep learning classifier for prediction of pathological complete response to neoadjuvant chemotherapy from baseline breast DCE-MRI,” in *Medical Imaging 2018: Computer-Aided Diagnosis*, 2018, vol. 10575, p. 11, doi: 10.1117/12.2294056.

[108] Y. Qu, H. Zhu, K. Cao, X. Li, M. Ye, and Y. Sun, “Prediction of pathological complete response to neoadjuvant chemotherapy in breast cancer using a deep learning (DL) method,” *Thorac. Cancer*, vol. 11, no. 3, pp. 651–658, Mar. 2020, doi: 10.1111/1759-7714.13309.

[109] R. J. G. Van Sloun, R. Cohen, and Y. C. Eldar, “Deep Learning in Ultrasound Imaging,” *Proc. IEEE*, vol. 108, no. 1, pp. 11–29, Jan. 2020, doi: 10.1109/JPROC.2019.2932116.

[110] M. Byra, H. Piotrzkowska-Wroblewska, K. Dobruch-Sobczak, and A. Nowicki, “Combining Nakagami imaging and convolutional neural network for breast lesion

classification," in *IEEE International Ultrasonics Symposium, IUS*, 2017, pp. 1–4, doi: 10.1109/ULTSYM.2017.8092154.

[111] V. Sharma and C. Dyreson, "COVID-19 Screening Using Residual Attention Network an Artificial Intelligence Approach," in *Proceedings - 19th IEEE International Conference on Machine Learning and Applications, ICMLA 2020*, 2020, pp. 1354–1361, doi: 10.1109/ICMLA51294.2020.00211.

[112] Z. Gandomkar, P. C. Brennan, and C. Mello-Thoms, "MuDeRN: Multi-category classification of breast histopathological image using deep residual networks," *Artif. Intell. Med.*, vol. 88, pp. 14–24, Jun. 2018, doi: 10.1016/j.artmed.2018.04.005.

[113] Y. Xu *et al.*, "Deep learning predicts lung cancer treatment response from serial medical imaging," *Clin. Cancer Res.*, vol. 25, no. 11, pp. 3266–3275, Jun. 2019, doi: 10.1158/1078-0432.CCR-18-2495.

[114] C. Szegedy *et al.*, "Going deeper with convolutions," in *Proceedings of the IEEE Computer Society Conference on Computer Vision and Pattern Recognition*, 2015, vol. 07-12-June-2015, pp. 1–9, doi: 10.1109/CVPR.2015.7298594.

[115] C. Szegedy, S. Ioffe, V. Vanhoucke, and A. A. Alemi, "Inception-v4, inception-ResNet and the impact of residual connections on learning," in *31st AAAI Conference on Artificial Intelligence, AAAI 2017*, 2017, pp. 4278–4284.

Chapter 2

Characterizing Intra-Tumor Regions on Quantitative Ultrasound Parametric Images to Predict Chemotherapy Response at Pre-Treatment*

2.1. Introduction

Breast Cancer is the most frequent malignancy and the leading cause of cancer-related death among women [1], [2]. In 2018 more than 2 million new breast cancer cases were diagnosed, and more than 0.6 million people died from it [3]. Up to 20% of breast cancer patients are diagnosed with locally advanced breast cancer (LABC) that often presents as tumors greater than 5 cm in size, possibly with regional lymph node, skin and/or chest wall involvement [4], [5]. LABC patients have a high risk of relapse and metastasis, with a 5-year survival rate of around 55% [5]. The standard treatments for LABC patients include a combination of neoadjuvant chemotherapy (NAC), followed by surgery, and if required, adjuvant radiation and/or hormonal therapies [4], [6]. Response to NAC has demonstrated a high correlation to the patient survival [6]–[8]. However up to 40% of LABC patients do not respond to NAC, and complete pathological response is limited to only 10-30% of the patients [4], [5], [9]–[12]. Current methods for evaluating response to NAC are based on changes in tumor size in routine physical examination or anatomical imaging. However, changes in tumor size may require many weeks to months of therapy to be detectable, and in some cases, it is not evident despite a pathological response to NAC [13]. Post-surgical histopathology is the standard approach to determine tumor pathological response to NAC [7], [8], [14], [15]. However, at that point the window to adjust the NAC or switch to a salvage treatment

* The material presented in this chapter has been published in *Scientific Reports* (2021).

is already closed. Prediction of LABC response to NAC before or early after the start of treatment can facilitate changing ineffective treatments to more effective ones. A personalized treatment strategy for LABC patients is expected to improve the rate of response to neoadjuvant therapies, and the overall survival and quality of life of the patients.

Genetic approaches have recently been investigated for prediction of cancer response to treatment [16]. Specifically, analysis of circulating tumor DNA has shown promise in evaluation of breast cancer response to therapy [17], [18]. Whereas such methods provide crucial scientific insights, they are invasive, relatively expensive, and require time-consuming analyses for quantification of circulating tumor DNA and gene sequencing. For monitoring and evaluating breast cancer response to NAC, functional imaging techniques including positron emission tomography (PET) and magnetic resonance imaging (MRI) have been investigated and shown promise within weeks after the treatment initiation [19]–[21]. However, these modalities are often expensive with long scan times and need injection of contrast agents to detect functional changes in tumor in response to treatment. Adapting an imaging modality with higher availability, lower cost, and an intrinsic source of image contrast to predict tumor response would facilitate adoption of the developed methodologies in routine clinical practice.

Ultrasound is a relatively inexpensive and portable imaging modality with a high spatial resolution and short imaging time that does not require injection of exogenous contrast agents. Quantitative ultrasound (QUS) techniques examine the frequency dependence of the radiofrequency (RF) signal backscattered from the underlying tissue to extract parameters that quantify tissue physical properties, and can be used to characterize tissue micro-structure [22]. Specifically, efficacy of the QUS parameters derived from the analysis of normalized power spectrum of RF signal, including mid-band fit (MBF), spectral slope (SS), spectral 0-MHz intercept (SI), effective scatterer diameter

(ESD) and effective acoustic concentration (EAC) have been demonstrated in detecting and characterizing different abnormalities including prostate and breast cancer, intraocular tumors and cardiovascular disease [23]–[28].

A number of previous studies have demonstrated that changes in QUS spectral parameters after the start of treatment could be used to detect tumor cell death [29], and monitor breast cancer responses to chemotherapy [30]–[32]. Also, it has been demonstrated that compared to the QUS mean-value parameters, alterations in the textural characteristics of QUS spectral parametric maps have higher correlations to histological tumor cell death in response to chemotherapy [33], and could be used to predict LABC tumor response to NAC as early as one week after starting the treatment [34], [35]. Textural measures of the QUS parametric maps quantify the spatial relationship between local acoustic properties within the tumor and their early alterations after treatment initiation could characterize changes in response-related intra-tumor heterogeneity [35]. Sannachi *et al.* showed that a combination of QUS spectral and, textural parameters and molecular features of tumor could predict the LABC tumor response with high sensitivity and specificity [36]. In a recent study, Tadayyon *et al.* have demonstrated that a combination of QUS parameters derived from the tumor core and margin could be applied to characterize the responsiveness of LABC tumors to NAC before starting the treatment [37]. In particular, their study highlighted the importance of spatial heterogeneity within tumor core and margin in characterizing tumor aggressiveness and predicting its likelihood of response to standard chemotherapy at pre-treatment.

Imaging-based characterization of distinct intra-tumor regions has been shown efficacious for characterizing malignancies and predicting their therapy outcome [38]–[40]. Previous studies have investigated the potential of imaging tumor habitats in characterizing the lung cancer [41], head

and neck cancer [42], and the breast cancer [43] and demonstrated that the characteristics of such habitats can be associated with the treatment response and patient survival. Intra-tumor regions evident on imaging can be linked to differential tumor biology and micro-structure, including clusters of heterogenous cancer cells, activated molecular pathways, calcification foci, hypoxic or necrotic/apoptotic areas, and regions with different perfusion and metabolic activities [27], [35], [44]–[46]. A study by Byra *et al.* has demonstrated that features of intra-tumor regions identified using QUS maps of homodyned K distribution parameters could be used to differentiate benign and malignant breast lesions [40]. Another study by Wu *et al.* has showed the potential of characterizing intra-tumor regions on MRI in predicting pathological response of breast tumors to chemotherapy [47]. Despite its demonstrated potential for tissue characterization in various diagnostic and prognostic applications, to our knowledge, no previous work has applied QUS parametric imaging to quantify distinct intra-tumor regions for therapy response prediction.

This study investigated the efficacy of QUS spectral multi-parametric imaging in characterizing LABC intra-tumor regions to predict tumor response to NAC before the start of treatment. QUS spectral parametric images were generated using the ultrasound data acquired from 181 LABC patients at pre-treatment. The dataset was randomly partitioned into a training set (70%) and an independent test set (30%). A hidden Markov random field (HMRF) expectation maximization (EM) algorithm was applied to identify distinct intra-tumor regions on QUS multi-parametric images [48]. Several features were extracted from the segmented regions on different parametric maps within the tumor core and margin to characterize each tumor. The features were analyzed using a multi-step feature ranking and selection process to construct an optimal QUS biomarker consisting of four features for response prediction. For comparison, the features extracted from the unsegmented tumor core and margin were also analyzed and applied for predicting the therapy

response. A decision tree model with adaptive boosting (AdaBoost) was adapted for classifying patients into responders and non-responders at pre-treatment. The patient responses to NAC identified after their surgery using standard clinical and pathological criteria were used as the ground truth to evaluate the performance of prediction models. Results indicated that the model with the developed biomarker could predict the NAC response of patients of the independent test set with a sensitivity and specificity of 87% and 85%, respectively. However, the models using barely features extracted from the unsegmented tumor core and the tumor margin predicted the NAC response with lower performance and an accuracy of up to 76.4%. Kaplan-Meier survival analyses showed that the patients predicted as responders using the optimal QUS biomarker demonstrated a statistically significantly better survival compared to those predicted as non-responders.

2.2. Materials and Methods

2.2.1. Study Protocol

This study was conducted under the guidelines and regulations in accordance with institutional research ethics board approval from Sunnybrook Health Sciences Centre (SHSC), Toronto Canada. The study was open to all women who were diagnosed with LABC aged 18–85 and planned for NAC followed by surgery. In accord with this, 181 eligible patients were recruited for the study after obtaining written informed consent. A core needle biopsy was performed for all patients to confirm cancer diagnosis, and determine the tumor grade and histological subtype. Also, for each patient pre-treatment magnetic resonance (MR) images of the breast were acquired to determine the initial tumor size. Ultrasound data were acquired from the patients immediately

before the start of NAC. Ultrasound scans were performed with patients lying supine with their arms above their heads. Patients were followed up to 10 years after their treatment and their clinical data were recorded for recurrence-free survival analysis. For this study, about 30% of patients (n = 53) were randomly selected and separated to form an unseen independent test set, and the remaining patients (n = 128) were considered as the training set.

2.2.2. Clinical and Pathological Response Evaluation

All patients had breast surgery after completing their neoadjuvant chemotherapy. For assessing residual tumor size, an MRI scan of the breast was obtained right before the surgery. The surgical specimens were stained with hematoxylin and eosin (H&E) and prepared when possible on whole-mount 5″ × 7″ pathology slides which were digitized using a confocal scanner (TISSUEscope, Huron Technologies, Waterloo, ON). All pathology samples were examined by a board-certified pathologist who remained blinded to the study results. Patients were categorized into two groups of responders and non-responders using a modified response (MR) grading system which was based on response evaluation criteria in solid tumors (RECIST) [49] and histopathological criteria [37][50]. The MR score was defined as follows: MR 1: no reduction in tumor size; MR 2: up to 30% reduction in tumor size; MR 3: 30% to 90% reduction in tumor size or a very low residual tumor cellularity determined histopathologically; MR 4: more than 90% reduction in tumor; MR 5: no evident tumor and no malignant cells identifiable in sections from the site of the tumor; only vascular fibroelastotic stroma remaining, often containing macrophages; nevertheless, ductal carcinoma in situ may be present. The patients with a MR score of 1-2 (less than 30% reduction in tumor size) and 3-5 (more than 30% reduction in tumor size or with very low residual tumor cellularity) were determined as non-responders and responders, respectively. In accordance with this, 138 and 43 patients were determined as responders and non-responders, respectively.

2.2.3. Ultrasound Data Acquisition

Ultrasound data were obtained using an RF-enabled Sonix RP, (Ultrasonix, Vancouver, Canada) system utilizing an L14-5/60 transducer, operating at the center frequency of ~6 MHz, and with a -6 dB bandwidth range of 3–8 MHz. For each breast tumor, ultrasound RF data and B-mode images were acquired at four to seven image planes across the breast with approximately 1 cm intervals. An oncologist selected the breast region for ultrasound scanning and determined acquisition scan planes via a physical examination of the patient. The image size along the lateral and axial directions was 6 cm and 4–6 cm, respectively. The focal depth was set at the center of the tumor depending on the individual patient circumstances. The RF data were acquired with a sampling frequency of 40 MHz and digitized with 16-bit resolution.

2.2.4. Parametric Map Generation

For generating the QUS parametric images, the tumor core was manually outlined by experts on each scan plane using the associated B-mode image. In addition, the tumor margin contour was automatically generated with a thickness of 5 mm around the core. The parametric maps were generated for all imaging planes of the tumor using a sliding window analysis throughout the entire region of interest (tumor core and margin) with windows of size 2 mm × 2 mm and 95% overlap in both lateral and axial direction.

The QUS spectral analyses were performed to derive MBF, SS, SI, ESD, EAC parameters [26], [27]. The power spectrum was calculated using the Fourier transform of the Hanning-gated RF data for every scan line within the analysis window and then averaged. A reference phantom technique was used to normalize the average power spectrum to remove the effects of the system transfer function and transducer beam-forming [46], [47]. The reference phantom was composed of 5 to 30 μm diameter glass beads embedded in a homogeneous background of microscopic oil

drop- lets in gelatin (Medical Physics Department, University of Wisconsin, USA). The attenuation coefficient and speed of sound parameters of the reference phantom were 0.576 dB/MHz.cm and 1488 m/s, respectively. The attenuation coefficient estimate (ACE) of tumor was calculated using a spectral difference method [46], and used for attenuation correction of the normalized power spectrum using the point attenuation compensation method. A two-layer (intervening tissue and tumor) attenuation correction was performed using total attenuation estimation [46]. An attenuation coefficient of 1 dB/MHz.cm was assumed for intervening breast tissue based on ultrasound tomography measurements of the breast [48]. The MBF, SS and SI parameters were estimated using a linear regression analysis within the -6 dB bandwidth of the transducer [26], [49], [50]. The ESD and EAC parameters were derived by fitting a spherical Gaussian form factor model to the estimated backscatter coefficient [51], [52].

2.2.5. Segmentation of Intra-Tumor Regions

Figure 2.1 demonstrates the overall diagram of the proposed framework for segmentation of intra-tumor regions on QUS multi-parametric images that were applied in the therapy response prediction model. The intra-tumor regions were identified at pixel level on QUS parametric images using a HMRF-EM algorithm and the tumor core parametric maps of ESD, EAC, MBF and SI as different data channels (described further below). The optimum number of distinct regions within tumors was determined using the elbow method over the samples of the training set [58]. Specifically, the intra-tumor segmentation was performed for different number of regions, and the Baysian information criterion (BIC) was estimated as the clustering quality metric. Subsequently,

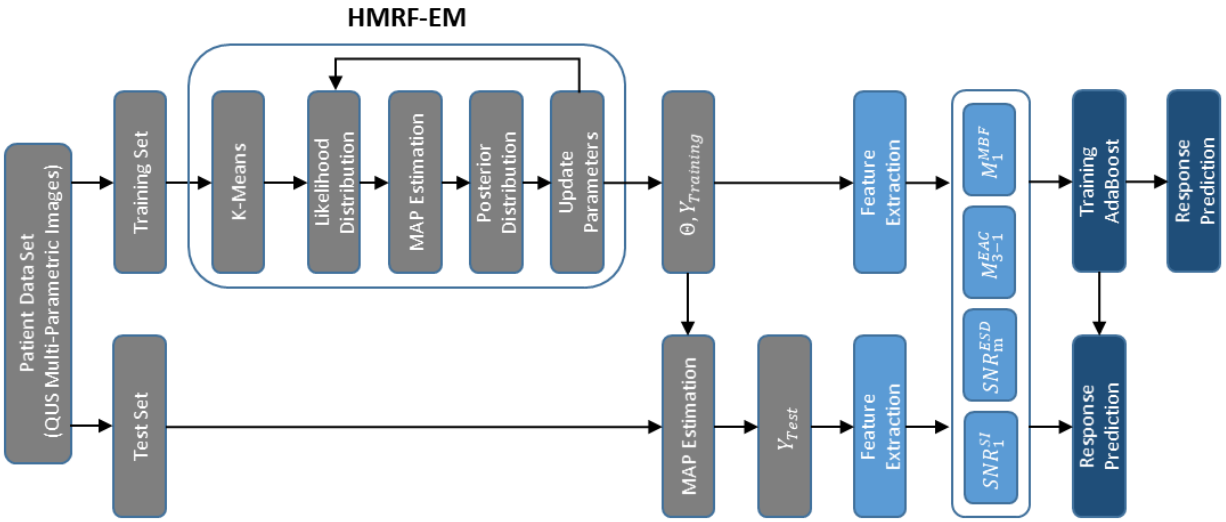

Figure 2.1. Overall diagram of the proposed framework for identification of intra-tumor regions on QUS multi-parametric images and therapy response prediction.

the least number of regions associated with a low BIC (the elbow point in the plot of BIC versus different number of regions) was identified. Using this method, the optimum number of distinct intra-tumor regions on the QUS parametric maps was determined as three regions.

A modified HMRF model was trained using an EM algorithm for segmentation of intra-tumor regions [48]. The HMRF-EM is an unsupervised classification method originally proposed for computer vision applications [59]. This method can be adapted for segmentation of multi-channel color images [48], and medical imaging data [48], [60]. In this work, we applied different QUS parametric maps as different channels of data (features) to segment intra-tumor distinct regions. For each pixel *i* (*i=1, ..., N*), the feature set can be defined as $x_i = (I_i^{ESD}, I_i^{EAC}, I_i^{MBF}, I_i^{SI})$. The goal is to infer the labels $Y = (y_1, y_2, \dots, y_N)$ where $y_i = \{1,2,3\}$, for all tumor core pixels within a set of parametric maps $X = (x_1, x_2, \dots, x_N)$ with maximum a posteriori probability (MAP) estimation. In other words, the estimated labels Y* should satisfy:

$$Y^* = argmax_y \{P(X|Y,\theta)P(Y)\} \qquad (2.1)$$

Where the prior probability $P(Y)$ is a Gibbs distribution and θ is representative of multivariate Gaussian distribution parameters. For the joint likelihood probability, we have:

$$P(X|Y,\theta) = \prod_i P(x_i|Y,\theta) = \prod_i P(x_i|y_i,\theta_i) \qquad (2.2)$$

Where $P(x_i|y_i,\theta_i)$ is a multivariate Gaussian distribution with parameters $\theta_{x_i} = (\mu_i, \Sigma_i)$, such that μ_i is the mean and Σ_i is the precision matrix of the distribution. The modified HMRF-EM algorithm was used to solve Equation (2.1). To estimate initial parameters and labels, a K-means algorithm was applied on the parametric maps. Then, the following steps were performed iteratively:

1. Compute the likelihood distribution $P^t(x_i|y_i,\theta_i)$ in step *t*.
2. Use the current parameter set θ^t to estimate the labels by the MAP estimation algorithm [48].
3. Calculate the posterior distribution $P^t(l|x_i)$ for all the $l \in \{1,2,3\}$ and all pixels x_i utilizing the Bayesian rule.
4. Compute the updated parameter set θ^{t+1} with calculated posterior distribution.

In this study, we performed the iteration on the whole training set for 15 times or until convergence. Also, we repeated the inner loop in the MAP estimation algorithm for 10 times or until convergence. Subsequently, the estimated Gaussian distribution parameters (θ) were used to determine the labels of the pixels in the parametric maps of the test set. The segmented regions were numbered based on the mean-value in the MBF parametric maps of the training set from the highest (first region) to the lowest (third region) values. The in-group proportion (IGP) criterion was computed at patient level using the HMRF model developed over the entire training set to evaluate the reproducibility of the clustering results and validate the consistency of the identified intra-tumor regions in both the training and independent test sets [61].

2.2.6. Feature Extraction and Biomarker Discovery

A total of 56 features were extracted from the segmented intra-tumor regions and the tumor margin in the QUS parametric maps of ESD, EAC, MBF and SI. The extracted features included mean-value and signal to noise ratio (SNR) of each parametric map within the tumor core (4 × 2 features), mean-value and SNR of each parametric map within the tumor margin (4 × 2 features), mean-value and SNR of each parametric map within each segmented region (4 × 3 × 2 features), the difference between the mean-value of each two segmented regions in each parametric map (4 × 3 features), the proportion area of each segmented region within the tumor core (3 features), and the relative area of the tumor margin to the core. The SNR of each region was acquired by calculating the ratio of the average pixel value to the standard deviation of pixel values of the region, as a measure of spatial heterogeneity [62]. The features were calculated for all 2D imaging planes associated with each tumor and subsequently averaged over the entire tumor volume.

A multi-step feature reduction/selection process was applied to eliminate the redundant and irrelevant features that do not contribute to the predictive model and obtain an optimal QUS feature set for robust response prediction. In the first step, the features were ranked and reduced to 21 features using the minimal-redundancy-maximal-relevance (mRMR) method [55]. In the next step, the final features were selected from the reduced feature set using a sequential forward selection (SFS) method. A 5-fold cross-validated accuracy on the training set was used as the criterion in the SFS method with an AdaBoost decision tree model as the classifier [59]. The SFS method selected four features as the optimal QUS feature set (biomarker) that was applied for training the response prediction model.

Four other experiments were conducted for comparison. In the first two experiments, the features extracted from the entire tumor core without considering any intra-tumor regions, and the tumor

margin were used for response prediction. Specifically, eight features including the mean-value and SNR of each parametric map within the tumor core (4 × 2 features), and 16 features consisting of the mean-value and SNR of each parametric map within the tumor core (4 × 2 features) and the tumor margin (4 × 2 features) were applied in these experiments, respectively. In both cases, the best feature set was selected using a similar SFS method as described above. The best feature sets included four features in both experiments, and were separately applied for response prediction as described below. In the third experiment, a similar feature reduction/selection procedure was applied on a merged set of standard clinical features and the 56 QUS features derived from the intra-tumor regions and tumor margin to obtain an optimal feature set for response prediction. The clinical features included the initial tumor size, estrogen/progesterone receptor (ER/PR) status, human epidermal growth factor receptor 2 (HER2) status and the age of patient. In the fourth experiment, only the clinical features were used to develop a response predictive model as described below.

2.2.7. Response Prediction and Risk Assessment

To address the imbalance issue of the dataset, the minority class in the training set was oversampled to the size of the majority class using the synthetic minority oversampling technique (SMOTE) [63]. An AdaBoost decision tree model was adapted for response prediction in each experiment. After training each model on the oversampled training set, its performance was evaluated on the independent test set using the accuracy, sensitivity, specificity, and the area under the receiver operating characteristic (ROC) curve (AUC).

Survival analysis was performed to assess the efficacy of the developed QUS biomarker at pre-treatment in differentiating the LABC patient cohorts with different recurrence-free survival determined many years later. The Kaplan-Meier survival curves were generated for the responders

and non-responders identified based on the model's prediction at pre-treatment, and at post-treatment based on the clinical and histopathological criteria. A log-rank test was used to assess for statistically significant differences between the survival curves of the two patient cohorts (responders versus non-responders).

2.3. Results

The clinical and histopathological characteristics of the participating patients are provided in table 2.1. The average age of the patients was 50.6 years. The patients had an average initial tumor size of 5.2 cm, and at the end of their treatment, the average residual tumor size was 2.5 cm. In terms of histology, 90.3% of the tumors were diagnosed with invasive ductal carcinoma, 3.4% with invasive lobular carcinoma, and 6.3% with invasive metaplastic carcinoma. Further, 10.6% of the patients were diagnosed with grade 1 tumors, 38.8% with grade 2 tumors, and 50.6% with grade 3 tumors. At the end of the treatment, 76.2% of the patients were identified as responders, and 23.8% as non-responder, according to the clinical and histopathological criteria.

Figure 2.2 demonstrates QUS parametric maps of ESD, EAC, MBF and SI overlaid on ultrasound B-mode images acquired from representative responding and non-responding patients, respectively. Distinct intra-tumor regions identified using the HMRF-EM algorithm are presented in Figure 2.2-E. The QUS parametric maps obtained from the responding and non-responding patients were different in terms of mean and spatial distribution of pixel values. A considerable difference was observed in size, and the mean, distribution and difference of the pixel values of the intra-tumor segmented regions on the QUS parametric maps acquired from the responders and non-responders. An average and median IGP of 0.99 was obtained at patient level in both the

training and test sets, implying a high-level of consistency in the intra-tumor regions identified using the HMRF-EM model.

Table 2.1. Patient characteristics.

Characteristic	**Mean ± SD / Percentage**
Age	50.6 ± 11.5 years
Initial Tumor Size	5.2 ± 2.7cm
Residual Tumor size	2.5 ± 3.4cm
Histology	
Invasive Ductal Carcinoma	90.3%
Invasive Lobular Carcinoma	3.4%
Invasive Metaplastic Carcinoma	6.3%
Tumor Grade	
Grade I	10.6%
Grade II	38.8%
Grade III	50.6%
Molecular Features	
ER+	63.4%
PR+	54.7%
HER2+	34.3%
Triple Negative	24.4%
ER+ / PR+ / HER2+	18.6%
ER+ / PR+ / HER2-	33.7%
ER- / PR- / HER2+	10.5%
Response	
Responders	76.2%
Non-Responders	23.8%

Figure 2.3 shows H&E stained histopathology images of the surgical specimens obtained from representative responding and non-responding patients. Whereas the histology images show a large residual tumor in the mastectomy specimen of the non-responding patient, the images acquired from the responding patient demonstrate the tumor bed area with chemotherapy effects and no residual tumor. The images also show considerable heterogeneity within the tumor (bed) area.

The multi-step feature selection process resulted in a QUS biomarker for NAC response prediction with four features out of 56 features including SNR of the SI parametric map within the first region (SNR_1^{SI}), SNR of the ESD parametric map within the tumor margin (SNR_m^{ESD}), difference between the mean-values of the EAC parametric map within the first and third regions (M_{3-1}^{EAC}), and mean-value of the MBF parametric map within the first segmented region (M_1^{MBF}). The first and third regions are associated with the highest and lowest mean-values in the MBF parametric maps, respectively. Figure 2.4 demonstrates the box plots of the selected features for responders and non-responders in the training set. Whereas various levels of difference can be observed in the selected features between the responders and non-responders, a combination of these features is expected to differentiate better between the response groups at pre-treatment. The impurity-based importance of these features in the trained AdaBoost decision tree model for response prediction was computed as 0.28, 0.26, 0.24, 0.22 for SNR_1^{SI}, SNR_m^{ESD}, M_{3-1}^{EAC}, and M_1^{MBF}, respectively.

Applying a similar feature selection method on the eight features derived from the unsegmented tumor core resulted in four features including mean-value of the MBF and SI parametric maps (M_C^{MBF} and M_C^{SI}), and SNR of the EAC and SI parametric map (SNR_C^{EAC} and SNR_C^{SI}) within the tumor core. In case of the 16 features derived from the unsegmented tumor core and the tumor margin the best feature set consisted of mean-value of the MBF and SI parametric maps within the tumor core (M_C^{MBF} and M_C^{SI}), SNR of the SI parametric map within the tumor margin (SNR_m^{SI}), and SNR of the EAC parametric map within the tumor core (SNR_C^{EAC}). Further, applying a similar feature reduction/selection procedure on the merged set of standard clinical features with the 56 QUS features derived from the intra-tumor regions and tumor margin resulted in the same QUS features selected previously (SNR_1^{SI}, SNR_m^{ESD}, M_{3-1}^{EAC}, and M_1^{MBF}) with no clinical feature included in the optimal feature set.

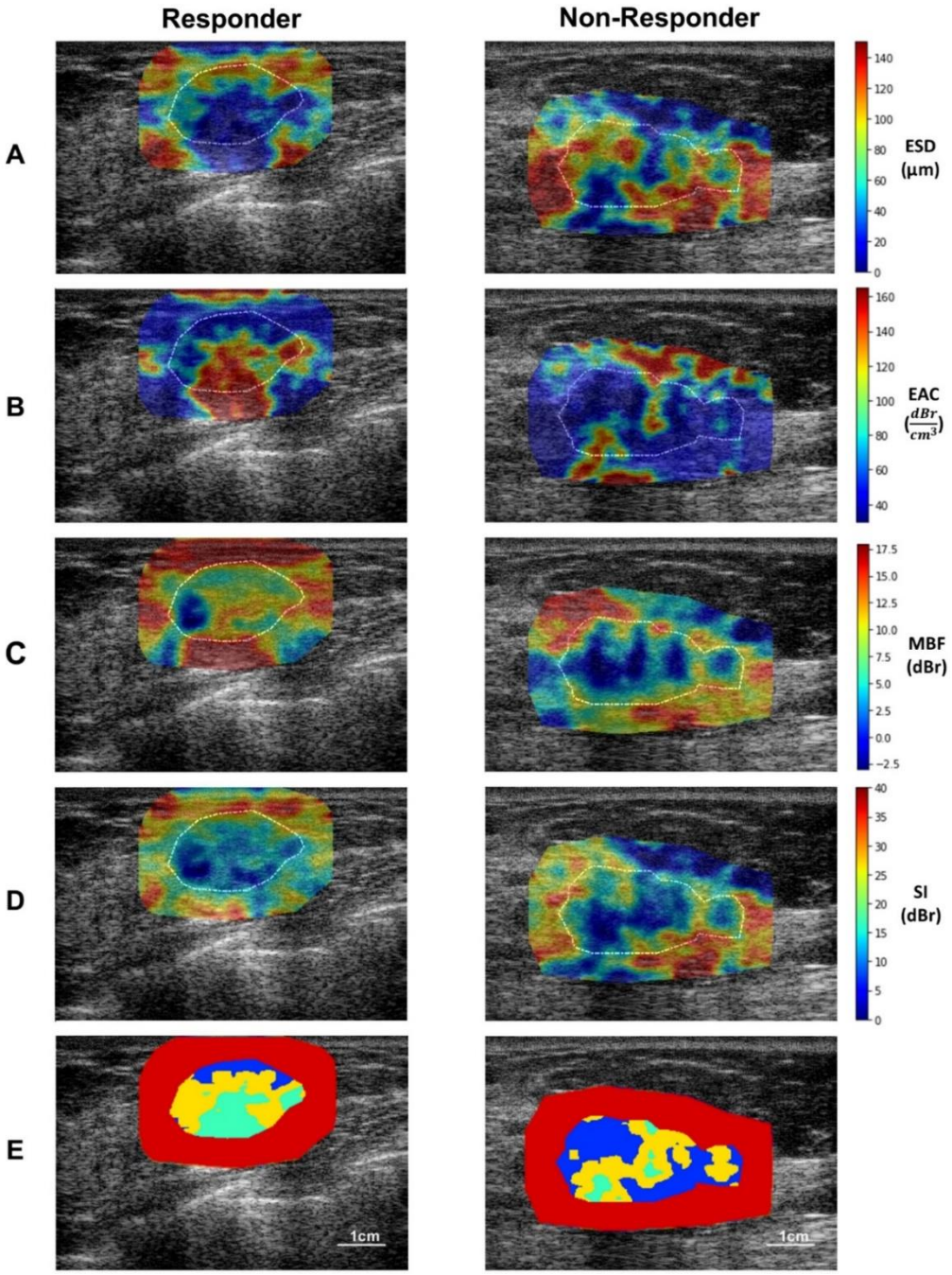

Figure 2.2. A-D: Ultrasound B-mode images with parametric overlays of ESD (A), EAC (B), MBF (C), and SI (D) acquired from a representative responder and non-responder to NAC. The tumor core has been outlined with white dashed line. E: distinct intra-tumor regions (region 1: green, region 2: yellow, region 3: blue) segmented using the HMRF-EM algorithm, surrounded by the tumor margin area (red).

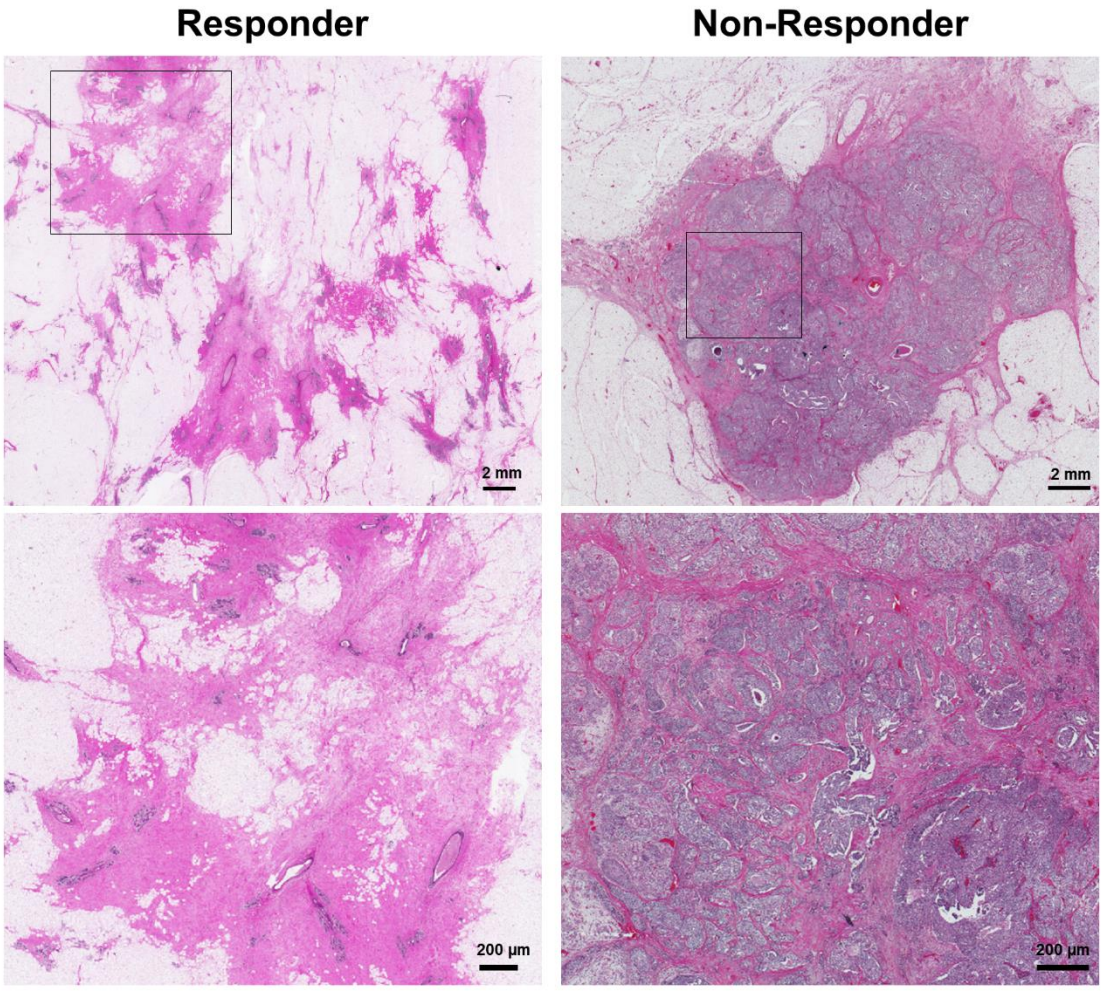

Figure 2.3. Whole mount histopathology images of mastectomy specimens acquired from representative responding and non-responding patients, at low (top) and high (bottom) magnifications. The scale bars represent 2 mm and 200 µm in low and high-magnification images.

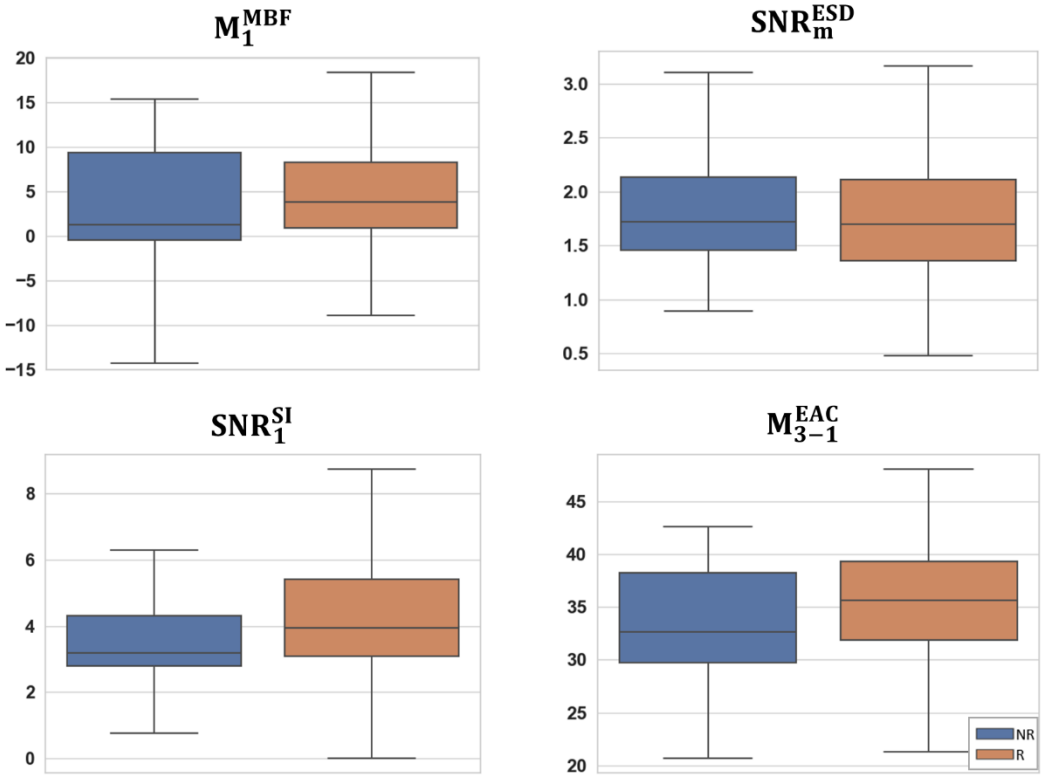

Figure 2.4. Box plots of the selected features including M_1^{MBF}, SNR_m^{ESD}, SNR_1^{SI} and M_{3-1}^{EAC} for the responders and non-responders in the training set.

Table 2.2 presents the result of response prediction on the training and independent test sets using the clinical features and the best feature sets obtained in different experiments. The predictive model with the clinical features could predict the therapy response of patients with a sensitivity, specificity, accuracy and AUC of 40%, 80%, 69.1%, and 0.6, respectively, on the independent test set. Applying the selected QUS features among those extracted from the unsegmented tumor core in response prediction resulted in an accuracy of 74.5%, a sensitivity of 66.6%, and a specificity of 77.5% on the independent test set. Incorporating the QUS features derived from the tumor margin increased the specificity to 80% and the accuracy to 76.4%. Applying the QUS biomarker consisting of the features derived from the segmented intra-tumor regions and the tumor margin resulted in the best performance of the response prediction model on both the training and test sets, with an accuracy, sensitivity, specificity, and AUC of 85.4%, 86.6%, 85.0%, and 0.89,

respectively, on the independent test set. Figure 2.5 demonstrates the ROC curves of the predictive models with different feature sets on the test set.

Table 2.2. Results of response prediction on the training and independent test sets using different clinical and QUS feature sets. Acc: Accuracy; Sen: Sensitivity; Spec: Specificity.

Feature Set	**Training Set**				**Test Set**			
	Acc	**Sen**	**Spec**	**AUC**	**Acc**	**Sen**	**Spec**	**AUC**
Clinical Features: Tumor Size, ER/PR, HER2, Age	77.0%	51.9%	83.8%	0.678	69.1%	40.0%	80.0%	0.6
Unsegmented Core: $M_C^{MBF}, SNR_C^{EAC}, SNR_C^{SI}, M_C^{SI}$	81.0%	81.5%	80.8%	0.853	74.5%	66.6%	77.5%	0.79
Unsegmented Core and Margin: $M_C^{MBF}, SNR_m^{SI}, SNR_C^{EAC}, M_C^{SI}$	81.0%	77.8%	81.8%	0.86	76.4%	66.6%	80.0%	0.76
Intra-Tumor Regions and Margin: $SNR_1^{SI}, SNR_m^{ESD}, M_{3-1}^{EAC}, M_1^{MBF}$	90.5%	88.9%	91.0%	0.974	85.4%	86.6%	85.0%	0.89

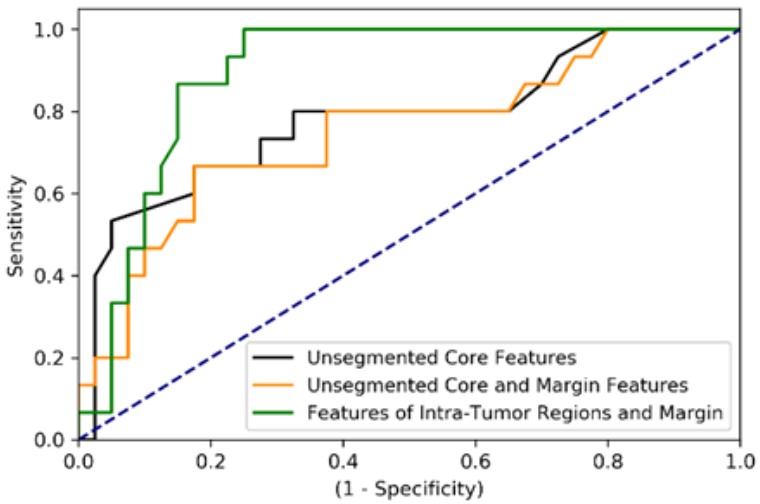

Figure 2.5. The ROC curves of the therapy response prediction models with different QUS feature sets on the independent test set.

Figure 2.6 demonstrates the ten-year recurrence-free survival curves for the responding and non-responding patients identified based on prediction at pre-treatment using the optimal QUS biomarker, and at post-treatment using the clinical and pathological criteria. Statistically significant differences (p-value < 0.05) were observed between the survival curves of the histopathological response cohorts in both the training and test sets, and responders demonstrated a significantly higher survival rate compared to non-responders. Similar trends were observed in the survival curves of the response cohorts predicted at pre-treatment, with statistically significant differences between the long-term survival of the two cohorts in both the training and test sets.

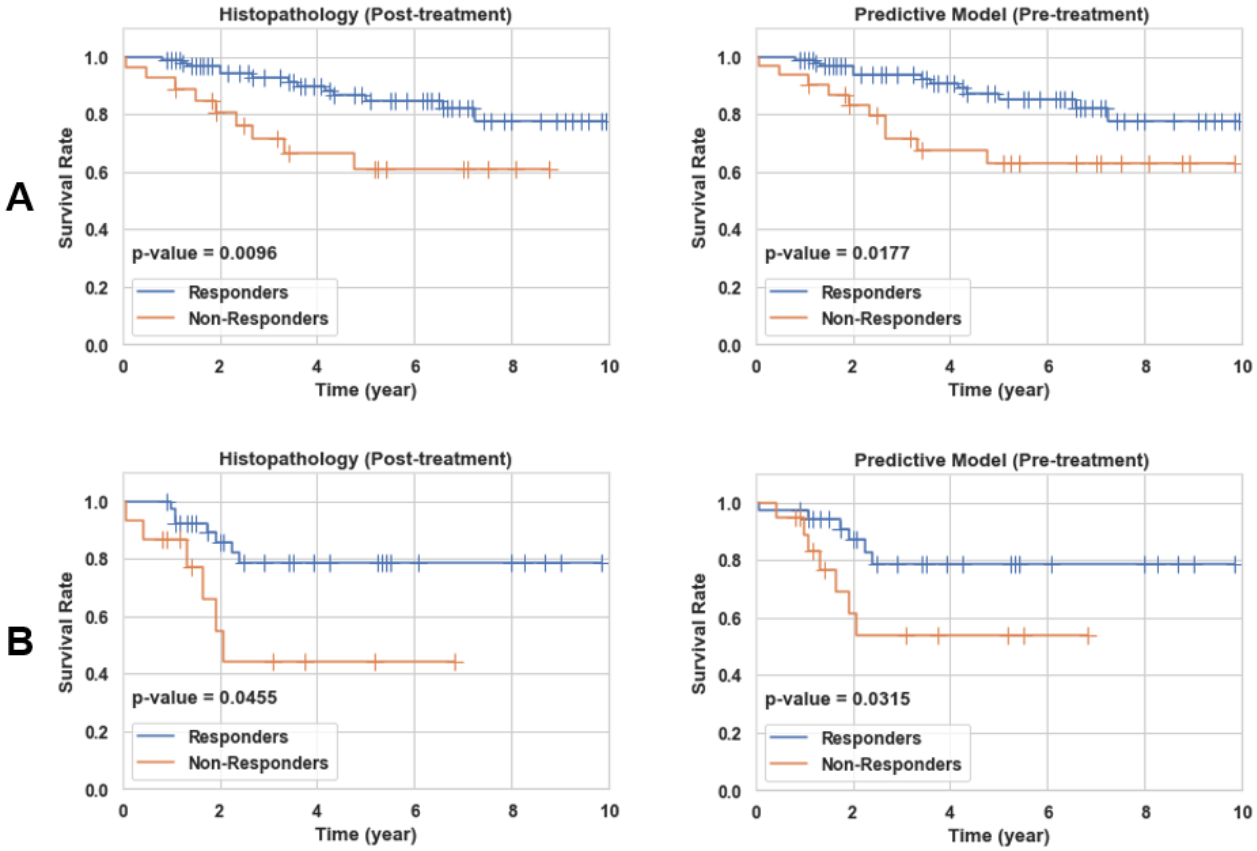

Figure 2.6. Ten-year recurrence-free survival curves for responding and non-responding patients in the training (A) and independent test set (B) identified at post treatment based on the clinical and histopathological criteria, and at pre-treatment using the developed predictive model with the optimal QUS biomarker.

2.4. Discussion

In this study, a novel method was investigated to predict breast cancer response to NAC using the characteristics of distinct intra-tumor regions on QUS multi-parametric images acquired at pre-treatment. A modified HMRF-EM algorithm was applied to segment the intra-tumor regions on QUS parametric images acquired from LABC patients. Several features were derived from the segmented QUS multi-parametric images to characterize the identified intra-tumor regions and tumor margin. A hybrid QUS biomarker consisting of four features were constructed through a multi-step feature selection process for NAC response prediction. Results indicated that the developed QUS biomarker in conjunction with an AdaBoost decision tree model could predict the response of LABC patient to NAC before starting the treatment with an accuracy of 85.4% and an AUC of 0.89. In comparison, applying the best features extracted from the whole tumor core and the tumor margin on the QUS parametric images resulted in an accuracy of 76.4% and an AUC of 0.76. Obtained results support the idea that using characteristics of distinct intra-tumor regions identified on the QUS multi-parametric images can improve the accuracy of therapy response prediction in breast cancer. Further, the results indicate a very good potential of these QUS features in comparison with standard clinical factors for therapy response prediction at pre-treatment. Recurrence-free survival analyses were performed to evaluate the performance of the developed predictive model in differentiating patients in terms of long-term treatment outcomes. The ten-year recurrence-free survival curves obtained for the responders and non-responders identified based on prediction at pre-treatment were very similar to their counterparts generated for the two response groups identified at post-treatment using the clinical and histopathological criteria. Statistically significant differences were observed between the survival of the responders and non-responders identified based on the both methods.

A number of recent studies has demonstrated the potential of QUS spectral and textural parameters to predict and monitor response of breast cancer to chemotherapy [34]–[37]. Those studies evaluated the efficacy of QUS parameters for therapy response evaluation using a leave-one-patient-out cross-validation approach due to the relatively small size of their dataset. Whereas cross-validation approaches are commonly used in evaluating classification models when limited data are available, they may overestimate a model's performance due to overfitting. The study here introduced a new method for analyzing the QUS multi-parametric images for response prediction by quantifying the properties of intra-tumor regions. The developed QUS biomarker was evaluated on an independent test set that was kept unseen during the biomarker discovery and predictive model training. The results obtained in this study extend the findings of previous studies on efficacy of QUS parameters for therapy response evaluation to new robust features that were assessed rigorously on independent data.

The results of this study indicated that characteristics of intra-tumor regions and tumor margin identified on QUS parametric maps of ESD, EAC, MBF and SI could be used for predicting the LABC response to chemotherapy prior to start of treatment. These parametric maps provide complementary information regarding the tumor microstructure by quantifying the properties of underlying acoustic scatterers including their size, density, distribution and impedance mismatch [22], [23], [26]. Recent studies have demonstrated the potential of the QUS parametric maps in characterizing the tumor aggressiveness and its responsiveness to systemic therapies [34], [64]. Segmenting the distinct regions on these multi-parametric maps potentially facilitates effective characterization of intra-tumor heterogeneity. Among the three intra-tumor regions identified in this study, region one is associated with the highest MBF and EAC mean-values, and the lowest ESD and SI mean-values in parametric maps of the entire training set, whereas region three has

the highest ESD and SI mean-values, and the lowest MBF and EAC mean-values. An accurate interpretation of these regions in terms of tumor biology requires pre-treatment histology or molecular imaging. However, based on the biophysical characteristics of these regions from the QUS multi-parametric images, region one and three can potentially be linked to the necrotic/apoptotic and active tumor areas, respectively. Region two may be associated with edema and highly perfused regions within the active tumor. Spatial heterogeneity within tumor has demonstrated a crucial role in its responsiveness/resistance to anti-cancer therapies and clinical outcome [39]. The findings of this study are in agreement with observations of previous studies that show quantification of tumor heterogeneity and intra-tumor regions (habitats) on imaging is effective for tumor characterization and therapy outcome prediction [27], [40], [47], [65], [66], and encourage investigation of such methodology when co-registered multi-parametric and/or multi-modal imaging data are available for solid tumors.

The optimal QUS biomarker developed through a multi-step feature selection process consists of four features including SNR_1^{SI}, SNR_m^{ESD}, M_{3-1}^{EAC}, and M_1^{MBF}. The SNR features in the biomarker can be linked to spatial heterogeneity in tissue microstructure within the associated region. M_{3-1}^{EAC} quantifies the difference in density and impedance mismatch of acoustic scatterer in the first and third segmented regions that can potentially be associated with the necrotic/apoptotic and active tumor areas, respectively. M_1^{MBF} is associated with the echogenicity of the first intra-tumor region and is related to the size, density and distribution of acoustic scatterers in tissue micro-structure [67]. The selected features imply that the four QUS parametric maps provide complementary information about the responsiveness of breast tumors to chemotherapy, as all the four parametric images have contributed to the developed biomarker with a relatively similar importance in the final predictive model. Further, the features derived from the distinct intra-tumor regions may

better characterize a tumor in terms of therapy response as the feature selection algorithm prioritizes those over the features derived from the entire tumor core. The second feature in the biomarker (SNR_m^{ESD}) is a measure of signal quality (homogeneity) in effective scatterer dimeters within the tumor margin. This is in agreement with the findings of previous studies that reported the importance of tumor margin characteristics in diagnostic and prognostic applications [37], [66], [68], [69]. Whereas the intra-tumor segmentation strategy is potentially expected to improve the feature robustness with respect to variations in the tumor contour, such robustness should be evaluated rigorously in future studies using multi-observer and/or automatically segmented tumor contours. Future studies may also adapt other methods proposed for clustering tumor habitats [43] to identify intra-tumor regions on QUS multi-parametric images and investigate their performance in comparison with the HMRF-EM algorithm for tumor characterization and therapy outcome prediction.

In conclusion, this study demonstrated that intra-tumor regions in LABC could effectively be segmented on QUS multi-parametric maps for chemotherapy response prediction. The QUS biomarker developed using this methodology could predict the breast tumor response to NAC with high sensitivity and specificity and classify patients into two cohorts with significantly different long-term outcomes. Predicting cancer response to chemotherapy at pre-treatment with demonstrated correlations to long-term survival can facilitate adoption of precision medicine for cancer patients. The results obtained in this study are encouraging. However, studies on larger patient populations are required to assess further the efficacy and robustness of the proposed methodology in clinic. Availability of data from larger patient cohorts will also permit stratified analyses across breast cancer sub-types to explore the performance of the developed models for different molecular and histological sub-types.

References

[1] I. A. for R. on C. (IARC). WHO, "GLOBOCAN 2012: Estimated Cancer Incidence, Mortality and Prevalence Worldwide in 2012.," *Globocan*, pp. 1–6, 2012.

[2] C. J. L. Murray and A. D. Lopez, "Mortality by cause for eight regions of the world: Global Burden of Disease Study," *Lancet*, vol. 349, no. 9061, pp. 1269–1276, May 1997.

[3] F. Bray, J. Ferlay, I. Soerjomataram, R. L. Siegel, L. A. Torre, and A. Jemal, "Global cancer statistics 2018: GLOBOCAN estimates of incidence and mortality worldwide for 36 cancers in 185 countries.," *CA. Cancer J. Clin.*, vol. 68, no. 6, pp. 394–424, Nov. 2018.

[4] G. N. Hortobagyi, "Comprehensive management of locally advanced breast cancer," *Cancer*, vol. 66, no. 6 Suppl, pp. 1387–91, Sep. 1990.

[5] S. H. Giordano, "Update on Locally Advanced Breast Cancer," *Oncologist*, vol. 8, no. 6, pp. 521–530, 2003.

[6] B. Fisher *et al.*, "Effect of preoperative chemotherapy on the outcome of women with operable breast cancer," *J. Clin. Oncol.*, vol. 16, no. 8, pp. 2672–2685, 1998.

[7] S. J. Cleator, a Makris, S. E. Ashley, R. Lal, and T. J. Powles, "Good clinical response of breast cancers to neoadjuvant chemoendocrine therapy is associated with improved overall survival.," *Ann. Oncol.*, vol. 16, no. 2, pp. 267–72, Feb. 2005.

[8] V. Guarneri *et al.*, "Prognostic value of pathologic complete response after primary chemotherapy in relation to hormone receptor status and other factors," *J. Clin. Oncol.*, vol. 24, no. 7, pp. 1037–44, Mar. 2006.

[9] D. Sethi, R. Sen, S. Parshad, S. Khetarpal, M. Garg, and J. Sen, "Histopathologic changes following neoadjuvant chemotherapy in locally advanced breast cancer," *Indian J. Cancer*, vol. 50, no. 1, pp. 58–64, 2013.

[10] S. Chuthapisith, J. M. Eremin, M. El-Sheemy, and O. Eremin, "Neoadjuvant chemotherapy in women with large and locally advanced breast cancer: Chemoresistance and prediction of response to drug therapy," *Surgeon*, vol. 4, no. 4., pp. 211–219, Aug-2006.

[11] W. Haque, V. Verma, S. Hatch, V. Suzanne Klimberg, E. Brian Butler, and B. S. Teh, "Response rates and pathologic complete response by breast cancer molecular subtype following neoadjuvant chemotherapy," *Breast Cancer Res. Treat.*, vol. 170, no. 3, pp. 559–567, Aug. 2018.

[12] T. Byrski *et al.*, "Pathologic complete response rates in young women with BRCA1-positive breast cancers after neoadjuvant chemotherapy," *J. Clin. Oncol.*, vol. 28, no. 3, pp. 375–379, Jan. 2010.

[13] K. Brindle, "New approaches for imaging tumour responses to treatment," *Nat. Rev. Cancer*, vol. 8, no. 2, pp. 94–107, Feb. 2008.

[14] B. T. Hennessy *et al.*, "Outcome after pathologic complete eradication of cytologically proven breast cancer axillary node metastases following primary chemotherapy," *J. Clin. Oncol.*, vol. 23, no. 36, pp. 9304–11, Dec. 2005.

[15] J. B. Nikas, W. C. Low, and P. A. Burgio, "Prognosis of treatment response (pathological complete response) in breast cancer," *Biomark. Insights*, vol. 7, pp. 59–70, Jan. 2012.

[16] O. J. Stoetzer *et al.*, "Prediction of response to neoadjuvant chemotherapy in breast cancer patients by circulating apoptotic biomarkers nucleosomes, DNAse, cytokeratin-18 fragments and survivin," *Cancer Lett.*, vol. 336, no. 1, pp. 140–148, Aug. 2013.

[17] H. Schwarzenbach and K. Pantel, "Circulating DNA as biomarker in breast cancer," *Breast Cancer Research*, vol. 17, no. 1., p. 136, Oct-2015.

[18] S.-J. Dawson *et al.*, "Analysis of circulating tumor DNA to monitor metastatic breast cancer," *N. Engl. J. Med.*, vol. 368, no. 13, pp. 1199–209, Mar. 2013.

[19] J. Czernin and M. E. Phelps, "Positron emission tomography scanning: current and future applications," *Annu. Rev. Med.*, vol. 53, pp. 89–112, Jan. 2002.

[20] B. S. Pio *et al.*, "Usefulness of 3'-[F-18]fluoro-3'-deoxythymidine with positron emission tomography in predicting breast cancer response to therapy," *Mol. imaging Biol.*, vol. 8, no. 1, pp. 36–42, 2006.

[21] C.-P. Chou *et al.*, "Monitoring breast cancer response to neoadjuvant systemic chemotherapy using parametric contrast-enhanced MRI: a pilot study," *Acad. Radiol.*, vol. 14, no. 5, pp. 561–73, May 2007.

[22] J. Mamou and M. L. Oelze, Eds., *Quantitative Ultrasound in Soft Tissues*. Dordrecht: Springer Netherlands, 2013.

[23] E. J. Feleppa *et al.*, "Typing of prostate tissue by ultrasonic spectrum analysis," *IEEE Trans. Ultrason. Ferroelectr. Freq. Control*, vol. 43, no. 4, pp. 609–619, Jul. 1996.

[24] M. Yang, T. M. Krueger, J. G. Miller, and M. R. Holland, "Characterization of anisotropic myocardial backscatter using spectral slope, intercept and midband fit parameters," *Ultrason. Imaging*, vol. 29, no. 2, pp. 122–34, Apr. 2007.

[25] D. J. Coleman, F. L. Lizzi, R. H. Silverman, L. Helson, J. H. Torpey, and M. J. Rondeau, "A model for acoustic characterization of intraocular tumors.," *Invest. Ophthalmol. Vis. Sci.*, vol. 26, no. 4, pp. 545–50, Apr. 1985.

[26] H. Tadayyon, A. Sadeghi-Naini, L. Wirtzfeld, F. C. Wright, and G. J. Czarnota, "Quantitative ultrasound characterization of locally advanced breast cancer by estimation of its scatterer properties," *Med. Phys.*, vol. 41, no. 1, p. 012903, Jan. 2014.

[27] H. Tadayyon, A. Sadeghi-Naini, and G. J. Czarnota, "Noninvasive characterization of locally advanced breast cancer using textural analysis of quantitative ultrasound parametric images," *Transl. Oncol.*, vol. 7, no. 6, pp. 759–767, Dec. 2014.

[28] A. Sadeghi-Naini *et al.*, "Quantitative ultrasound spectroscopic imaging for characterization of disease extent in prostate cancer patients," *Transl. Oncol.*, vol. 8, no. 1, pp. 25–34, Feb. 2015.

[29] A. Sadeghi-Naini *et al.*, "Low-frequency quantitative ultrasound imaging of cell death in vivo," *Med. Phys.*, vol. 40, no. 8, p. 082901, Jul. 2013.

[30] H. Tadayyon *et al.*, "Quantitative ultrasound assessment of breast tumor response to chemotherapy using a multi-parameter approach," *Oncotarget*, vol. 7, no. 29, pp. 45094–

45111, 2016.

[31] L. Sannachi *et al.*, "Non-invasive evaluation of breast cancer response to chemotherapy using quantitative ultrasonic backscatter parameters," *Med. Image Anal.*, vol. 20, no. 1, pp. 224–236, Nov. 2014.

[32] A. Sadeghi-Naini *et al.*, "Quantitative ultrasound evaluation of tumor cell death response in locally advanced breast cancer patients receiving chemotherapy," *Clin. Cancer Res.*, vol. 19, no. 8, pp. 2163–74, Apr. 2013.

[33] A. Sadeghi-Naini *et al.*, "Conventional frequency ultrasonic biomarkers of cancer treatment response in vivo," *Transl. Oncol.*, vol. 6, no. 3, pp. 234–243, Jun. 2013.

[34] A. Sadeghi-Naini *et al.*, "Chemotherapy-Response Monitoring of Breast Cancer Patients Using Quantitative Ultrasound-Based Intra-Tumour Heterogeneities," *Sci. Rep.*, vol. 7, p. 10352, 2017.

[35] A. Sadeghi-Naini *et al.*, "Early prediction of therapy responses and outcomes in breast cancer patients using quantitative ultrasound spectral texture," *Oncotarget*, vol. 5, no. 11, pp. 3497–3511, 2014.

[36] L. Sannachi *et al.*, "Response monitoring of breast cancer patients receiving neoadjuvant chemotherapy using quantitative ultrasound, texture, and molecular features," *PLoS One*, vol. 13, no. 1, p. e0189634, Jan. 2018.

[37] H. Tadayyon *et al.*, "A priori prediction of neoadjuvant chemotherapy response and survival in breast cancer patients using quantitative ultrasound," *Sci. Rep.*, vol. 7, p. 45733, 2017.

[38] J. Wu, A. T. Mayer, and R. Li, "Integrated imaging and molecular analysis to decipher tumor microenvironment in the era of immunotherapy," *Semin. Cancer Biol.*, doi: 10.1016/j.semcancer.2020.12.005, 2020.

[39] J. P. B. O'Connor, C. J. Rose, J. C. Waterton, R. A. D. Carano, G. J. M. Parker, and A. Jackson, "Imaging intratumor heterogeneity: Role in therapy response, resistance, and clinical outcome," *Clin. Cancer Res.*, vol. 21, no. 2, pp. 249–257, 2015.

[40] M. Byra, A. Nowicki, H. Wróblewska-Piotrzkowska, and K. Dobruch-Sobczak, "Classification of breast lesions using segmented quantitative ultrasound maps of homodyned K distribution parameters," *Med. Phys.*, vol. 43, no. 10, pp. 5561–5569, 2016.

[41] J. Wu *et al.*, "Robust Intratumor Partitioning to Identify High-Risk Subregions in Lung Cancer: A Pilot Study," *Int. J. Radiat. Oncol. Biol. Phys.*, vol. 95, no. 5, pp. 1504–1512, Aug. 2016.

[42] J. Wu *et al.*, "Tumor Subregion Evolution-Based Imaging Features to Assess Early Response and Predict Prognosis in Oropharyngeal Cancer," *J. Nucl. Med.*, vol. 61, no. 3, pp. 327–336, Mar. 2020.

[43] J. Wu *et al.*, "Intratumoral spatial heterogeneity at perfusion MR imaging predicts recurrence-free survival in locally advanced breast cancer treated with neoadjuvant chemotherapy," *Radiology*, vol. 288, no. 1, pp. 26–35, Jul. 2018.

[44] L. G. Martelotto, C. K. Y. Ng, S. Piscuoglio, B. Weigelt, and J. S. Reis-Filho, "Breast cancer intra-tumor heterogeneity," *Breast Cancer Research*, vol. 16, no. 3., p. 210, May-2014.

[45] A. Evans, I. Ellis, S. Pinder, and R. Wilson, *Breast calcification : a diagnostic manual*. Greenwich Medical Media, 2002.

[46] J. Wu *et al.*, "Heterogeneous enhancement patterns of tumor-adjacent parenchyma at MR imaging are associated with dysregulated signaling pathways and poor survival in breast cancer," *Radiology*, vol. 285, no. 2, pp. 401–413, Nov. 2017.

[47] J. Wu, G. Gong, Y. Cui, and R. Li, "Intratumor partitioning and texture analysis of dynamic contrast-enhanced (DCE)-MRI identifies relevant tumor subregions to predict pathological response of breast cancer to neoadjuvant chemotherapy," *J. Magn. Reson. Imaging*, vol. 44, no. 5, pp. 1107–1115, Nov. 2016.

[48] Q. Wang, "GMM-Based Hidden Markov Random Field for Color Image and 3D Volume Segmentation," *arXiv*, pp. 1212.4527 (1–7), 2012.

[49] E. A. A. Eisenhauer *et al.*, "New response evaluation criteria in solid tumours: Revised RECIST guideline (version 1.1)," *Eur. J. Cancer* vol. 45, no. 2, pp. 228–247, 2009.

[50] K. N. Ogston *et al.*, "A new histological grading system to assess response of breast cancers to primary chemotherapy: Prognostic significance and survival," *Breast*, vol. 12, no. 5, pp. 320–327, 2003.

[51] Y. Labyed, T. A. Bigelow, and B. L. McFarlin, "Estimate of the attenuation coefficient using a clinical array transducer for the detection of cervical ripening in human pregnancy," *Ultrasonics*, vol. 51, no. 1, pp. 34–9, Jan. 2011.

[52] L. X. Yao, J. A. Zagzebski, and E. L. Madsen, "Backscatter coefficient measurements using a reference phantom to extract depth-dependent instrumentation factors," *Ultrason. Imaging*, vol. 12, no. 1, pp. 58–70, Jan. 1990.

[53] N. Duric *et al.*, "Development of ultrasound tomography for breast imaging: Technical assessment," *Med. Phys.*, vol. 32, no. 5, p. 1375, 2005.

[54] F. L. Lizzi *et al.*, "Comparison of theoretical scattering results and ultrasonic data from clinical liver examinations," *Ultrasound Med. Biol.*, vol. 14, no. 5, pp. 377–385, 1988.

[55] M. F. Insana, R. F. Wagner, D. G. Brown, and T. J. Hall, "Describing small-scale structure in random media using pulse-echo ultrasound," *J. Acoust. Soc. Am.*, vol. 87, no. 1, pp. 179–92, Jan. 1990.

[56] M. L. Oelze, W. D. O'Brien, J. P. Blue, and J. F. Zachary, "Differentiation and characterization of rat mammary fibroadenomas and 4T1 mouse carcinomas using quantitative ultrasound imaging," *IEEE Trans. Med. Imaging*, vol. 23, no. 6, pp. 764–71, Jun. 2004.

[57] M. F. Insana and T. J. Hall, "Parametric ultrasound imaging from backscatter coefficient measurements: image formation and interpretation.," *Ultrason. Imaging*, vol. 12, no. 4, pp. 245–67, Oct. 1990.

[58] M. A. Syakur, B. K. Khotimah, E. M. S. Rochman, and B. D. Satoto, "Integration K-Means Clustering Method and Elbow Method for Identification of the Best Customer Profile Cluster," in *IOP Conference Series: Materials Science and Engineering*, 2018, vol. 336, no. 1, pp. 012017 (1–6).

[59] S. Z. Li, “Markov random field modeling in computer vision,” Springer Japan, ISBN: 978-4-431-66933-3, 1995.

[60] Y. Zhang, M. Brady, and S. Smith, “Segmentation of brain MR images through a hidden Markov random field model and the expectation-maximization algorithm,” *IEEE Trans. Med. Imaging*, vol. 20, no. 1, pp. 45–57, Jan. 2001.

[61] A. V. Kapp and R. Tibshirani, “Are clusters found in one dataset present in another dataset?,” *Biostatistics*, vol. 8, no. 1, pp. 9–31, Jan. 2007.

[62] R. F. Wagner, S. W. Smith, J. M. Sandrik, and H. Lopez, “Statistics of Speckle in Ultrasound B-Scans,” *IEEE Trans. Sonics Ultrason.*, vol. 30, no. 3, pp. 156–163, 1983.

[63] N. V. Chawla, K. W. Bowyer, L. O. Hall, and W. P. Kegelmeyer, “SMOTE: Synthetic Minority Over-sampling Technique,” *J. Artif. Intell. Res.*, vol. 16, pp. 321–357, Jun. 2002.

[64] H. Tadayyon *et al.*, “*A priori* prediction of breast tumour response to chemotherapy using quantitative ultrasound imaging and artificial neural networks,” *Oncotarget*, vol. 10, no. 39, p. 3910, Jun. 2019.

[65] A. Sadeghi-Naini *et al.*, “Early detection of chemotherapy-refractory patients by monitoring textural alterations in diffuse optical spectroscopic images,” *Med. Phys.*, vol. 42, no. 11, pp. 6130–6146, Nov. 2015.

[66] E. Karami *et al.*, “Quantitative MRI Biomarkers of Stereotactic Radiotherapy Outcome in Brain Metastasis.,” *Sci. Rep.*, vol. 9, p. 19830, Dec. 2019.

[67] R. M. Vlad, S. Brand, A. Giles, M. C. Kolios, and G. J. Czarnota, “Quantitative ultrasound characterization of responses to radiotherapy in cancer mouse models,” *Clin. Cancer Res.*, vol. 15, no. 6, pp. 2067–2075, 2009.

[68] P. M. Lamb, N. M. Perry, S. J. Vinnicombe, and C. A. Wells, “Correlation between ultrasound characteristics, mammographic findings and histological grade in patients with invasive ductal carcinoma of the breast,” *Clin. Radiol.*, vol. 55, no. 1, pp. 40–44, 2000.

[69] A. M. Fowler, D. A. Mankoff, and B. N. Joe, “Imaging Neoadjuvant Therapy Response in Breast Cancer,” *Radiology*, vol. 285, no. 2, pp. 358–375, Nov. 2017.

Chapter 3

Deep Learning of Quantitative Ultrasound Multi-Parametric Images for Chemotherapy Response Prediction at Pre-Treatment

3.1. Introduction

Breast cancer is the most common cancer type and the foremost cause of cancer-related death among women [1], [2]. In 2020, around 2.3 million new cases of breast cancer were diagnosed worldwide and it caused around 0.7 million deaths among females [1]. Locally advanced breast cancer (LABC) is an aggressive subtype of breast cancer that includes up to 20% of new cases each year [3]. LABC is often identified with tumors greater than 5 cm in size and possibly with skin and/or chest wall involvement. Moreover, LABC includes patients diagnosed with inflammatory breast cancer or multiple positive axillary lymph nodes [3][4].

Patients diagnosed with LABC suffer from high risk of relapse and metastasis. With availability of different systemic and targeted regimens, neoadjuvant chemotherapy (NAC) followed by surgery is currently considered as the standard treatment for LABC patients [5]–[8]. In some cases, the surgery is followed by adjuvant radiation and/or hormonal therapies to reduce the risk of cancer recurrence [4][6]. Although response to NAC has demonstrated a high correlation to the patient survival, complete pathological response is limited to less than 30% of the patients, with about 30% of the patient do not even partially respond to NAC [3]–[5], [9]–[14]. To determine the tumor pathological response to NAC, post-surgical histopathology is considered as the standard approach [5]–[8]. However, post-surgical evaluations cannot be used for adjusting the NAC or switching to salvage treatment.

Currently, monitoring tumor response to NAC mostly relies on physical examination or standard anatomical imaging to assess the changes in tumor size. The main limitation of these methods is that detectable changes in tumor dimensions usually become apparent after several months of therapy, and in some cases a measurable change may not become evident on imaging despite a pathological response to NAC [15]. Early prediction of tumor response to NAC can permit therapy adjustments, switching to more effective treatments or even salvage therapies before it is potentially too late for individual patients [16], [17]. A personalized strategy for LABC treatment is anticipated to improve tumor response to neoadjuvant therapies, spare patients from unnecessary side effects of ineffective treatment, and improve their overall survival and quality of life.

Ultrasound is a portable, rapid and cost-efficient imaging modality that can be applied to characterize tissue physical properties without injection of any exogenous contrast agents. In particular, quantitative ultrasound (QUS) techniques have been introduced to derive quantitative measures of tissue biophysical properties that are independent of instrument settings, with a lower level of dependence to the operator [18]. Quantitative ultrasound spectral analysis techniques examine the frequency dependence of the ultrasound radiofrequency (RF) signal backscattered from the underlying tissue which can be used for tissue micro-structure characterization [18]. The QUS parameters derived from the analysis of normalized power spectrum of RF signal including the mid-band fit (MBF), spectral slope (SS), spectral 0-MHz intercept (SI), effective scatterer diameter (ESD) and effective acoustic concentration (EAC) have shown promises in detecting and characterizing malignancies, examination of liver tissues and detecting cardiovascular disease [19]–[25].

It has been shown that QUS spectral parameters can detect tumor cell death induced by various anti-cancer-therapies [26]–[29]. Also, several studies have demonstrated that the hand-crafted

features derived from the QUS parametric maps can be used to predict and monitor breast cancer response to neoadjuvant chemotherapy before or within weeks after the start of treatment, with a high correlations to clinical and pathological response identified at the end of treatment [30]–[33]. For example, it has been demonstrated that textural features of QUS spectral parametric maps have higher correlations to histological tumor cell death in response to chemotherapy in comparison with QUS mean-value parameters [34]. Further, A few studies have revealed the potential of the textural features of QUS parametric images in predicting LABC tumor response to NAC as early as one week after starting the treatment [35]–[37]. In a recent study, Tadayyon *et al.* have demonstrated that using the QUS hand-crafted features derived from both the tumor core and its margin could improve the performance of tumor response prediction before starting the treatment [38].

The deep learning approaches have recently been investigated in different applications of medical image analysis [39], [40]. Such methodologies can potentially remove the process of extracting carefully designed hand-crafted features from images required for conventional machine learning techniques. Instead, the deep learning frameworks optimize their data-driven feature maps during the iterative training procedure [41]. In this context, a few studies have been conducted on adapting deep convolutional neural networks (DCNN) for NAC therapy response prediction in breast cancer patients using magnetic resonance imaging (MRI) [42]–[44]. Moreover, few studies have explored the potential of DCNNs in analyzing ultrasound images of breast tumors for cancer classification. For example, Byra *et al.* have demonstrated the potential of convolutional neural networks for breast lesion classification using Nakagami parametric images [45]. To our knowledge, no previous study has explored the efficacy of deep learning techniques with QUS multi-parametric images for therapy response prediction.

In this study, the effectiveness of DCNN methodologies on QUS spectral multi-parametric images has been investigated to predict LABC response to NAC before the start of treatment. The QUS spectral parametric images were generated using the ultrasound data acquired from 181 LABC patients at pre-treatment. The patient responses to NAC were identified after their surgery using the standard clinical and pathological criteria, and used as the ground truth to evaluate the performance of the prediction models. The dataset was randomly partitioned into a training set and an independent test set. Different DCNN architectures including RAN [46], and ResNet [47] were investigated for feature extraction in the developed framework. In a set of experiments, the feature maps were extracted from the tumor core and the core and its margin. After averaging the features on different tumor cross-sections, a fully connected network was utilized for response prediction. Results demonstrated that the developed model with the RAN architecture for extracting feature maps from the expanded parametric images of the tumor core with margin had superior performance with an AUC of 0.86 on the independent test set. The Kaplan-Meier survival analyses showed that the patients predicted as the responders using this model demonstrated a significantly better survival rate in comparison with those predicted as non-responders.

3.2. Materials and Methods

3.2.1. Study Protocol

This study was conducted in accordance with institutional research ethics board approval from Sunnybrook Health Sciences Centre (SHSC), Toronto Canada. The study was open to all women aged 18–85, diagnosed with LABC and planned for NAC followed by surgery. After obtaining written informed consent, 181 eligible patients were recruited for the study. A core needle biopsy was done for each patient to confirm the cancer diagnosis and grade the tumor. The initial tumor

size was determined for each patient using the magnetic resonance (MR) images of the affected breast. Ultrasound B-mode images and radiofrequency (RF) data were acquired from the patients (in supine position with arms above the head) before the start of NAC. Patients were followed up to 10 years after their treatment and their clinical data were recorded for survival analysis. Out of the 181 patients, about 30% (n = 50) were randomly selected and kept unseen as an independent test set, and the remaining patients (n = 131) were considered as the training set and used to develop and optimize the predictive models.

3.2.2. Clinical and Pathological Response Evaluation

In keeping with the institutional guidelines, all patients had breast surgery after completing their neoadjuvant chemotherapy. Before surgery, the residual tumor size was determined using MRI. Standard histopathology was performed on the surgical specimens to assess the pathological response of tumor to NAC. The specimens were stained with hematoxylin and eosin (H&E) and prepared when possible on whole-mount 5″ × 7″ pathology slides. The mounted slides were digitized using a confocal scanner (TISSUEscope, Huron Technologies, Waterloo, ON). A board-certified pathologist who remained blinded to the study results examined all pathology samples. A modified response (MR) grading system based on response evaluation criteria in solid tumors (RECIST) [48] and histopathological criteria [38][49] was used to categorize the patients into two groups of responders and non-responders. In the MR grading system, the MR score is defined as follows: MR 1: no reduction in tumor size; MR 2: less than 30% reduction in tumor size; MR 3: between 30% and 90% reduction in tumor size or a very low residual tumor cellularity determined histopathologically; MR 4: more than 90% reduction in tumor; MR 5: no evident tumor and no malignant cells identifiable in sections from the site of the tumor (ductal carcinoma in situ may be present). In this study, patients with a MR score of 1-2 (less than 30% reduction in tumor size)

were considered as non-responders, and patients with a MR score 3-5 (more than 30% reduction in tumor or very low residual tumor cellularity) were determined as responders. In keeping with this, 138 and 43 patients were identified as responders and non-responders, respectively.

3.2.3. Ultrasound Data Acquisition

Ultrasound RF data were acquired utilizing an RF-enabled Sonix RP system (Ultrasonix, Vancouver, Canada) and an L14-5/60 transducer. The transducer operated at the center frequency of ~6 MHz with a -6 dB bandwidth of 3–8 MHz. The RF data were acquired with a sampling frequency of 40 MHz and digitized with a 16-bit resolution. For each tumor, the ultrasound data were acquired at four to seven image planes across the breast with approximately 1 cm intervals. The focal depth was set at the center of the tumor depending on the individual patient circumstances. The breast region for ultrasound scanning was specified by an oncologist who determined the acquisition scan planes via a physical examination of the patient. The image size along the lateral and axial directions was 6 cm and 4–6 cm, respectively.

3.2.4. QUS Parametric Map Generation

For generating the parametric images, QUS spectral analyses were performed in conjunction with a sliding window analysis (described below) to derive MBF, SI, ESD, and EAC parameters [22], [23]. The mean power spectrum was obtained by averaging over the Fourier transform of the Hanning-gated RF data calculated for every scan line of the analyzed window. The average power spectrum was normalized using a reference phantom method to remove the effects of the system transfer function and transducer beam-forming [50], [51]. The reference phantom was composed of 5 to 30 μm diameter glass beads embedded in a homogeneous background of microscopic oil droplets in gelatin (Medical Physics Department, University of Wisconsin, USA). The reference phantom had an attenuation coefficient of 0.576 dB/MHz.cm and a speed of sound parameter of

1488 m/s. The MBF and SI parameters were estimated using a linear regression analysis within the -6 dB bandwidth of the transducer [22], [52], [53]. The ESD and EAC parameters were derived by fitting a spherical Gaussian form factor model to the estimated backscatter coefficient [54], [55].

To generate the QUS parametric maps for each tumor, the tumor core was manually outlined by experts on each scan plane using the associated B-mode image. The tumor margin contour was automatically generated with a thickness of 5 mm around the core. The parametric maps were generated for all imaging planes of the tumor using a sliding window analysis throughout the entire region of interest (tumor core and margin) with windows of size 2 mm × 2 mm and 95% overlap in both lateral and axial direction.

3.2.5. Deep Learning Model

The deep learning framework developed in this study for response prediction consisted of two cascaded networks. The first network was a DCNN, with several convolutional layers as its backbone, adapted to extract the optimal feature maps from the QUS parametric images and is called the feature network in this chapter. The second network was a fully-connected network utilizing the features extracted by the feature network for response prediction. Two main architectures including a modified residual network version 101 (ResNet) [47] and a modified residual attention network version 56 (RAN) [46], were investigated as the backbone of the feature network. The second network consisted of two fully-connected layers with an input layer with the same size as the flatten feature vector (256), a middle layer with 100 neurons, and a softmax layer at the end with an output size of two to predict the probability of the response categories (responder versus non-responder) for each sample. Drop-out layers were added after the first and second layer of this network to avoid overfitting and enhance its generalization performance. The scheme of the

developed deep learning framework is shown in Figure 3.1. This figure demonstrates the adapted ResNet and RAN architectures with their residual and attention modules. The figure also depicts the fully connected layers applied after the feature network for optimizing the feature maps. As shown in the figure, the averaged optimized feature maps were subsequently used in another fully connected network (predictive network) adapted for response prediction (described further below). In the residual module applied in the ResNet architecture, the convolutional layer could be skipped through the identity branch. This strategy permits the very deep networks such as ResNet to avoid overfitting and achieve an improved performance on unseen samples. In the attention module applied in the RAN architecture, the trunk branch determines the information that can be passed through the network, whereas the mask branch determines the amount of information from the trunk branch that should be passed. Therefore, the module is able to pass the important information with higher weights and reduce the effect of less-important information in the network's output.

Before training the model, the parametric images were preprocessed and adjusted for the convolutional model. About 25% (31 patients) of the training set was randomly selected as a validation set to optimize the network hyperparameters. The parametric images were resampled to the size of 512×512 pixel. Then the pixel values in the parametric images of the training set were normalized to (0 1) to facilitate the training convergence. The training set normalization parameters were used for normalizing the validation and test sets. In order to improve the network training and alleviate the problem of having a relatively small training dataset, data augmentation was applied on the training set. For augmenting the training data, flipping horizontally and shifting both horizontally and vertically (maximum shift: 30% of image size) were stochastically applied.

For training the feature network, parametric images of the training set were fed into the feature network while different imaging planes of each tumor were considered as independent inputs with

the tumor response as their output. The optimal feature maps for each imaging plane were acquired by feeding its corresponding parametric images into the trained feature network. The optimal feature maps were calculated for all 2D imaging planes associated with each tumor, flatten to a 1D vector, and subsequently averaged over the entire tumor volume to obtain an averaged feature vector with size of 256×1 that was used in the predictive network. The predictive network was trained using the averaged feature vectors associated with the patients in the training set, and evaluated over the independent test set for response prediction. For training the networks, the cross entropy was used as the loss function, with a cost weight ratio of 5:1 for non-responders to responders to account for the unbalance in the dataset. The Adam optimizer was used for training the networks [56]. The network hyperparameters including the learning rate, cost weight, number of epochs, and the width of hidden layers in the fully connected network were optimized using the validation set. Early stopping was used to avoid overfitting by monitoring the network's performance on the validation set during the training process.

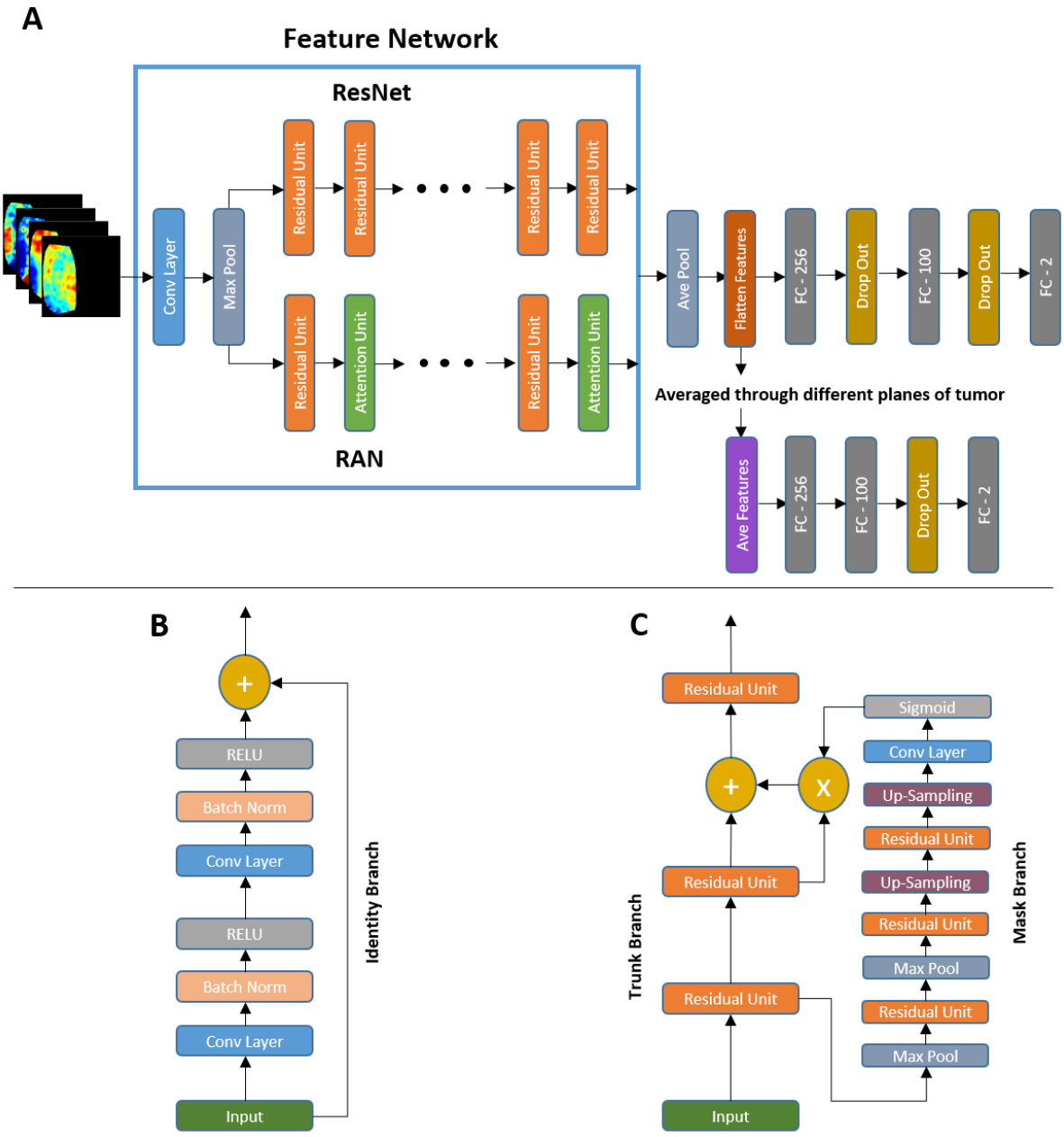

Figure 3.1. Scheme of the developed deep learning framework for response prediction, demonstrating the feature and predictive networks (A), The residual module (B), and the attention module (C).

3.2.6. Response Prediction and Risk Assessment

In different experiments, the QUS multi-parametric images (MBF, SI, ESD, and EAC) of the tumor core, as well as the core and its margin were investigated, as the inputs to the DCNN

framework and their performance were compared in response prediction. The deep learning models with different feature networks were trained and optimized using the training set. The performance of the optimized models was evaluated on the independent test set using the accuracy, sensitivity, specificity, and the ROC analysis. A prediction difference analysis (PDA) was performed to visualize the importance of different regions of the input QUS parametric images to the network's decision [57]. In each iteration of the modified PDA procedure applied in this study, a small patch (8 × 8 pixel with 50% overlap between adjacent patches) of one of the input parametric images was occluded (pixel values were set to zero). The absolute change in the model's prediction (output probability) was then calculated compared to the case of inputting the original parametric images, and considered as the impact of the occluded patch on the network's decision. The PDA maps were generated for each input parametric image by sliding the occluding patch over the image and assigning the estimated impact to its center.

The efficacy of the developed predictive models in differentiating the LABC patients with different recurrence-free survival was assessed through Kaplan-Meier survival analysis. The survival curves were generated for the responders and non-responders identified based on each model's prediction at pre-treatment, and at post-treatment based on the clinical and histopathological criteria. A long-rank test was applied to assess for statistically significant differences between the survival curves of the two response cohorts obtained in each experiment.

3.3. Results

Table 3.1 presents the clinical and histopathological characteristics of the participating patients. The average age of the patients was 50.6 years. The patients had an average initial tumor size of 5.2 cm, and the average residual tumor size at the end of their treatment was 2.5 cm. Histologically, 90.3% of the tumors were diagnosed with invasive ductal carcinoma, 3.4% with invasive lobular carcinoma, and 6.3% with invasive metaplastic carcinoma. Further, 10.6% of the patients were diagnosed with grade 1 tumors, 38.8% with grade 2 tumors, and 50.6% with grade 3 tumors. Using the MR grading system, 76.2% of the patients were identified as responders, and 23.8% as non-responder at the end of the treatment.

Figure 3.2 demonstrates QUS parametric maps of MBF, SI, ESD, and EAC overlaid on the ultrasound B-mode images acquired from representative responding and non-responding patients, respectively. As observed in these representative images, the QUS parametric maps associated with the responding and non-responding patients demonstrated different mean and spatial pattern of pixel values within the tumor core and margin. The figure also shows the PDA maps associated with these parametric images, visualizing the relative impact of different regions in each image to the network's decision for response prediction. Figure 3.3 demonstrates H&E stained histopathology images of the surgical specimens obtained from representative responding and non-responding patients. In responding patients, minimal tumor cellularity remained within the tumor bed after chemotherapy, as evident in the histopathology slides. In contrast, histopathology images of the non-responding patients typically indicated large areas of residual disease with minimal chemotherapy effects.

Table 3.2 presents the results of response prediction in different experiments on the validation and independent test sets. The ROC curves associated with the validation and test sets for different predictive models are demonstrated in figure 3.4. Using the ResNet architecture as the model's backbone to extract feature maps from the parametric images of the tumor core resulted in a sensitivity, specificity, and accuracy of 82.5%, 70% and 80%, respectively on the independent test set. Extending the input parametric images to include both the tumor core and its margin improved the AUC of this model from 0.77 to 0. 83.

Table 3.1. Patient characteristics

Characteristic	**Mean ± SD / Percentage**
Age	50.6 ± 11.5 years
Histology	
Invasive Ductal Carcinoma	90.3%
Invasive Lobular Carcinoma	3.4%
Invasive Metaplastic Carcinoma	6.3%
Tumor Grade	
Grade I	10.6%
Grade II	38.8%
Grade III	50.6%
Molecular Features	
ER+	63.4%
PR+	54.7%
HER2+	34.3%
ER+ / PR+ / HER2+	18.6%
ER+ / PR+ / HER2-	33.7%
ER- / PR- / HER2+	10.5%
ER- / PR- / HER2-	24.4%
Tumor Size	
Initial Tumor Size	5.2 ± 2.7cm
Residual Tumor size	2.5 ± 3.4cm
Response	
Responders	76.2%
Non-Responders	23.8%

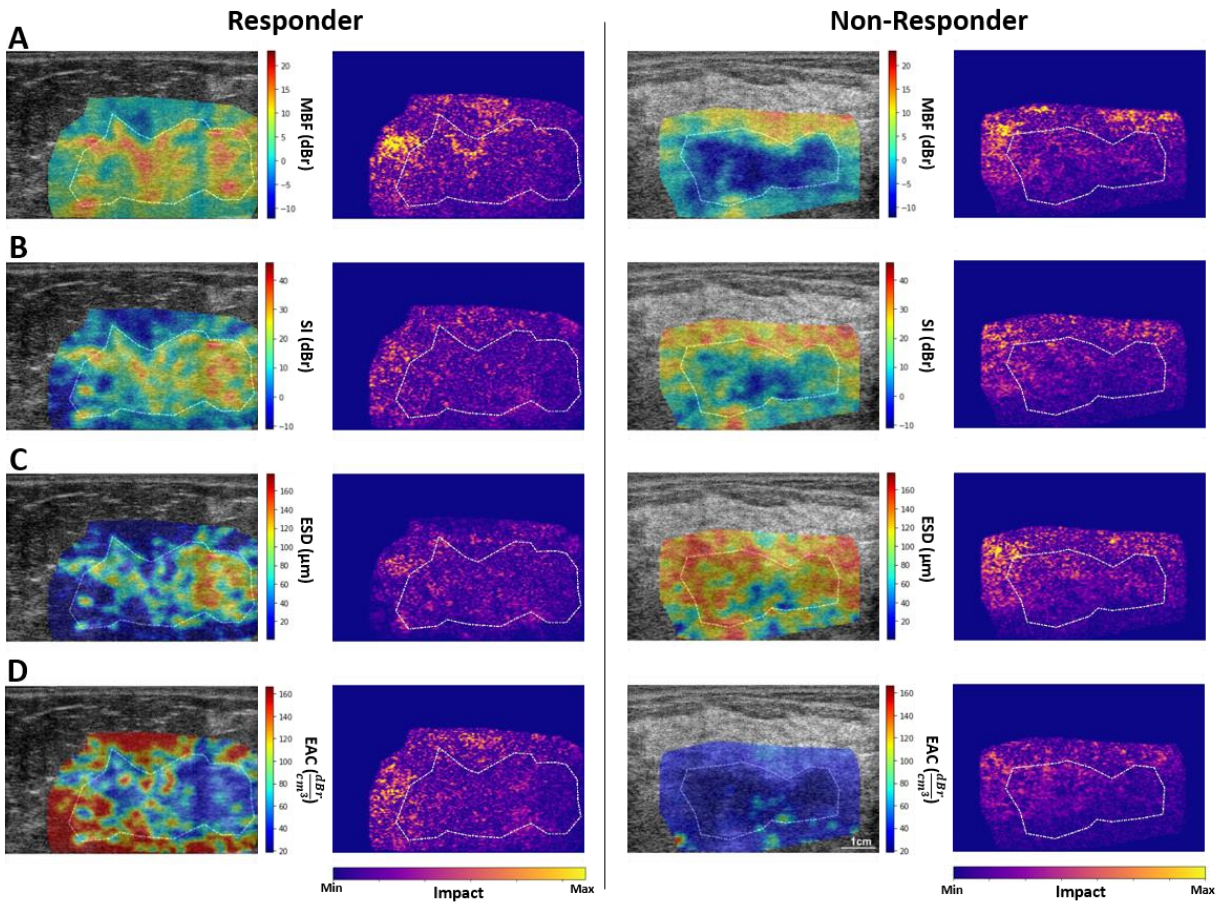

Figure 3.2. Ultrasound B-mode images with parametric overlays and of MBF (A), SI (B), ESD (C), and EAC (D) acquired at pre-treatment from a representative responder and non-responder to NAC, and the associated PDA maps visualizing the level of impact of different regions in each parametric image on the network's decision (model 4 in Table 3.2). The tumor core has been outlined with white dashed line.

Applying the extracted features from the parametric images of the tumor core using the RAN architecture resulted in an accuracy of 80%, and an AUC of 0.82 on the independent test set. Similar to the model with the ResNet architecture as the feature extractor, the performance of this model improved by extending the input parametric images to include the tumor margin. In particular, this model resulted in the best prediction performance with a sensitivity, specificity, accuracy and AUC of 92.5%, 70%, 88%, and 0.86, respectively on the independent test set. All models demonstrated a relatively similar performance on the validation and test sets, implying a good generalizability of the trained models on never seen samples.

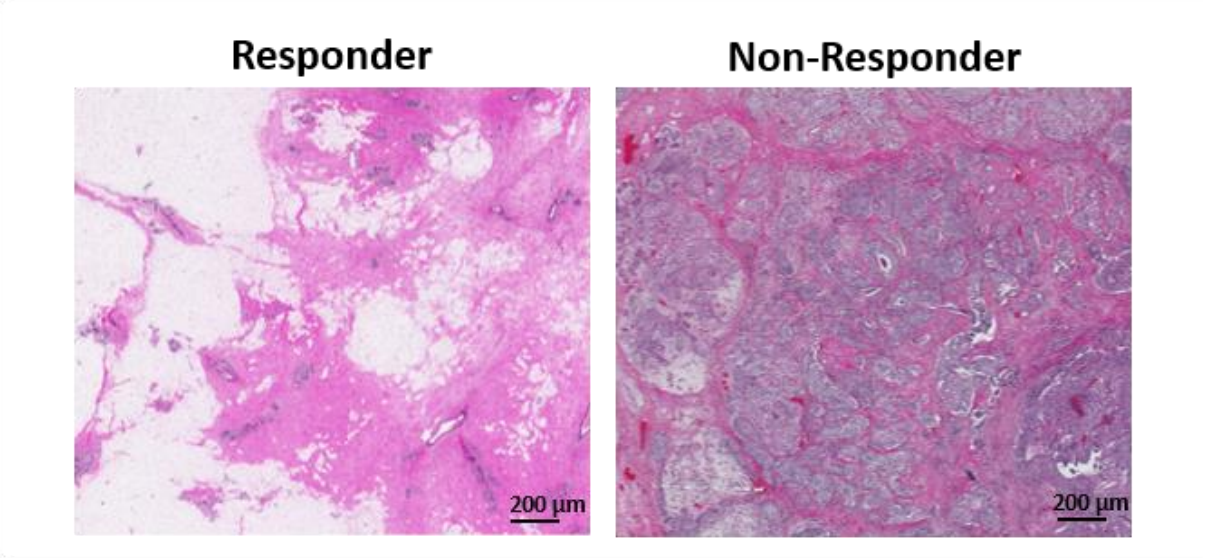

Figure 3.3. Histopathology images of mastectomy specimens acquired from representative responding and non-responding patients.

Figure 3.5 presents the ten-year recurrence-free survival curves for the responders and non-responders identified based on the clinical and histological criteria at post treatment, and at pre-treatment using the four predictive models presented in Tables 3.2. The survival analysis demonstrated a statistically significant difference (p-value = 0.030) between the survival curves of the responders and non-responders identified at post-treatment. Among the response cohorts predicted at pretreatment, the ones identified using the predictive models with the RAN as their feature network demonstrated a statistically significant difference or approached significance. Specifically, whereas the model that input the parametric images of the tumor core approached a significant difference (p-value = 0.058), the one with the input parametric images extended to the tumor margin demonstrated a statistically significant difference between the survival of the two predicted cohorts (p-value = 0.040). The response cohorts identified by the other two models at pre-treatment did not show a significant difference in survival.

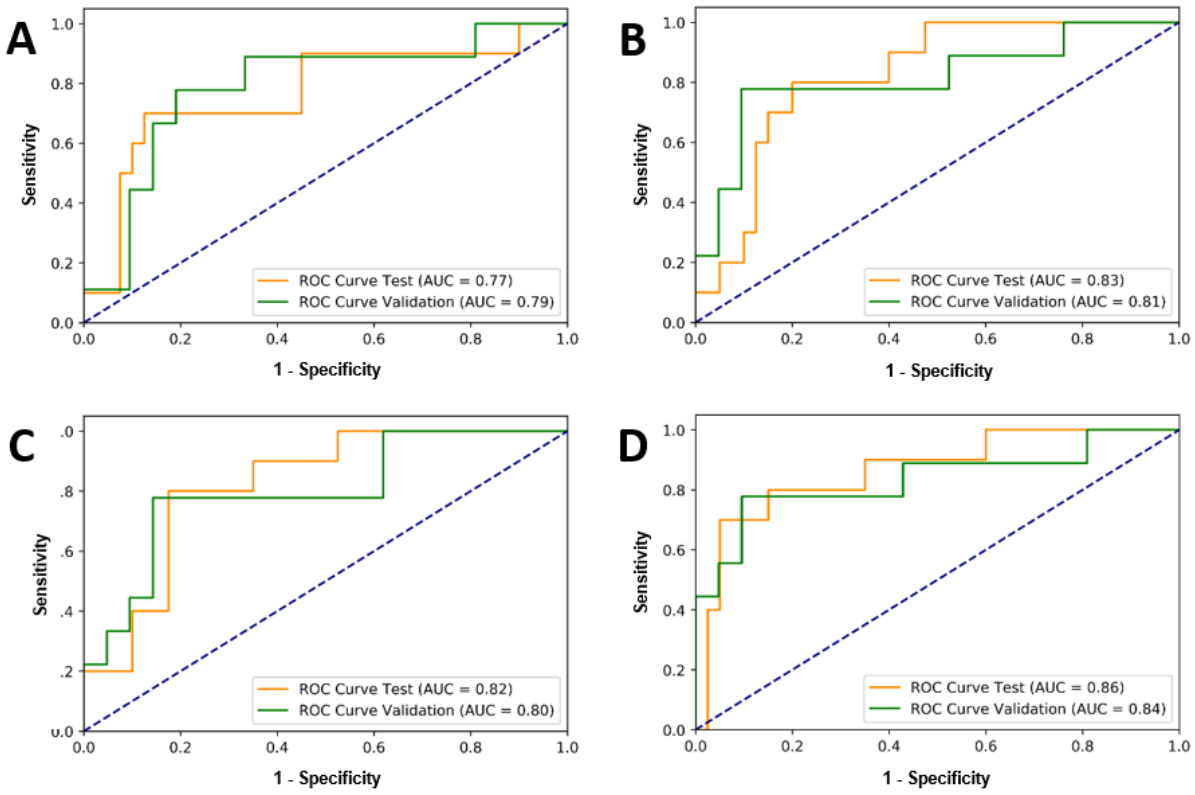

Figure 3.4. ROC curves generated for responding and non-responding patients in the validation set and independent test set identified at pre-treatment using the predictive models 1-4 in Table 3.2 (A-D).

Table 3.2. Results of response prediction on the validation and independent tests with different predictive models. Acc: Accuracy; Sen: Sensitivity; Spec: Specificity, Loss: Mean absolute error.

Model	Feature Network	Input Parametric Maps	Validation Set				Test Set			
			Acc	Spec	Sen	Loss	Acc	Spec	Sen	AUC
1	ResNet	Core	77%	76%	78%	0.27	80%	82.5%	70%	0.77
2	ResNet	Core + Margin	86%	90%	78%	0.17	82%	85%	70%	0.83
3	RAN	Core	83%	86 %	78%	0.22	80%	80%	80%	0.82
4	RAN	Core + Margin	86%	90%	78%	0.16	88%	92.5%	70%	0.86

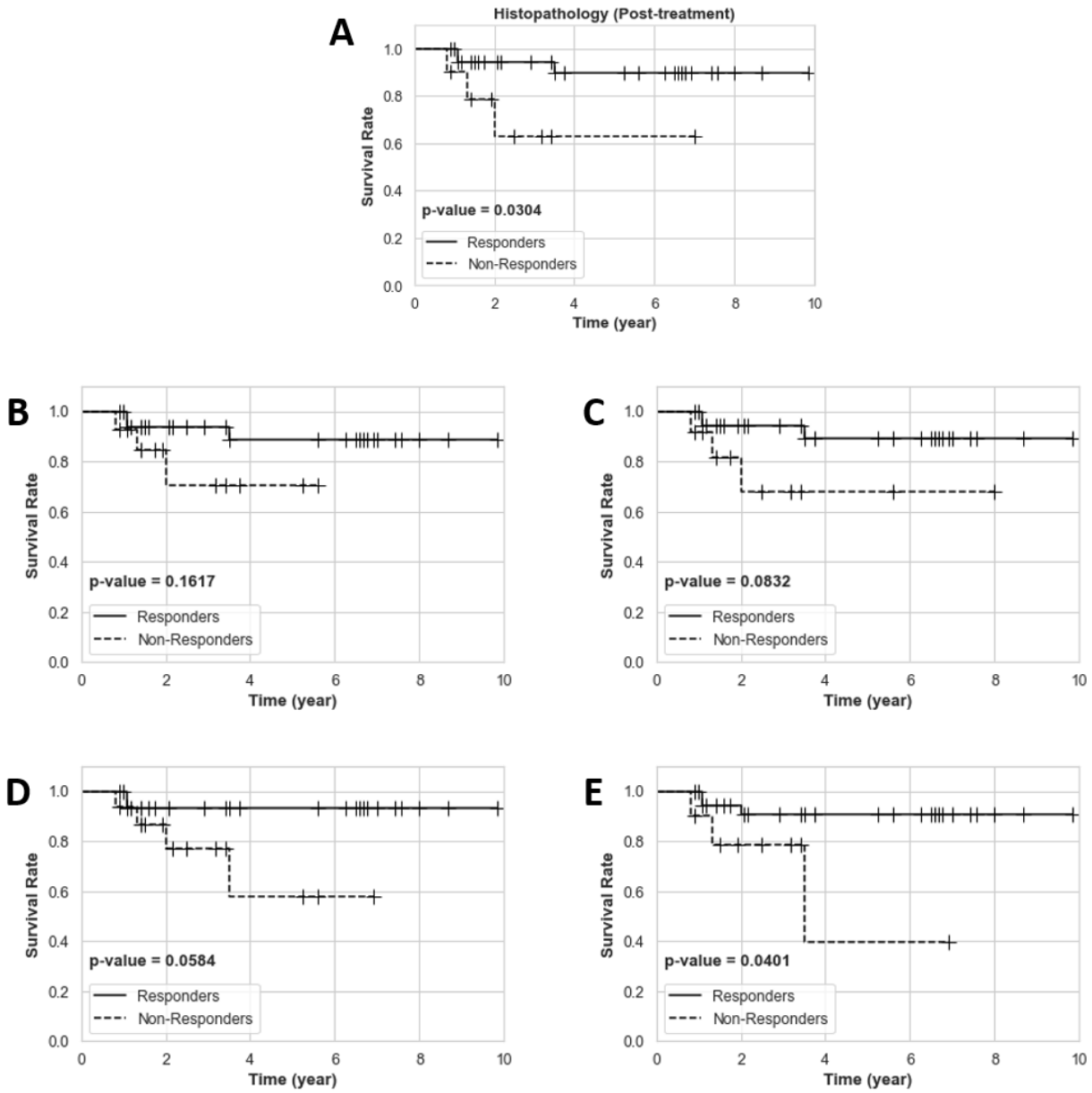

Figure 3.5. Ten-year recurrence-free survival curves for responding and non-responding patients in the independent test set identified at post treatment based on the clinical and histopathological criteria (A), and at pre-treatment using the predictive models 1-4 in table 3.2 (B-E).

3.4. Discussion and Conclusion

In this study, a deep learning methodology was proposed and investigated for predicting breast tumor response to NAC using the QUS parametric images acquired at pre-treatment. In the

proposed framework, a DCNN architecture was adapted to extract optimal feature maps from QUS multi-parametric images. The flatten feature vectors associated with different cross-sections of a tumor were averaged over the entire tumor volume. A fully-connected network was subsequently applied for response prediction, using the average feature vectors. The performance of the framework was investigated in a set of experiments using two different DCNN architectures including the ResNet and RAN as the backbone feature extractor, and the QUS parametric images of the tumor core, and the tumor core with margin as the input. The best performance in response prediction was achieved with the RAN architecture and the extended parametric images of the tumor core and margin, with an accuracy of 88%, a sensitivity of 92%, a specificity of 70%, and an AUC of 0.86 on the unseen test set. Long-term survival analyses demonstrated statistically significant differences between the survival of the responders and non-responders identified at pre-treatment based on this model's prediction, and at post-treatment based on the standard clinical and pathological criteria.

A number of previous studies have investigated the potential of QUS multi-parametric imaging in predicting and monitoring response of breast cancer tumors to NAC [38], [58]. In those studies, handcrafted features such as the statistical and textural features of the QUS parametric maps were analyzed and applied for response prediction using traditional machine learning methods. With predefined hand-crafted features, the feature extraction process is easier to understand and analyze. But these features only carry limited information based on their definition. Further, carefully determining and defining optimal discriminatory features for each specific application is crucial in this approach but is not always feasible. In this study, we investigated the potential of DCNN architectures for extracting optimal features from QUS multi-parametric images automatically through multiple convolutional layers. The advantage of using deep learning model for feature

extraction is that the model learns during the training process to extract the important information while considering the whole image. As the PDA maps generated for the QUS parametric images implied, different regions of these parametric maps contribute substantially to the model's prediction, albeit with varying levels.

It has been shown that intratumor heterogeneity is an important factor in responsiveness of tumors to cancer therapy, with several studies demonstrated the value of imaging-based quantitative features of tumor heterogeneity for response prediction [23], [59]–[62]. The results obtained in the study here using the DCNN feature extractors are in agreement with the observations of those studies. Specifically, the features maps extracted from the QUS multi-parametric images are computed using multiple layers of convolutional filters throughout a DCNN architecture and can quantify the spatial heterogeneity within multi-channels of the QUS images simultaneously. The results of different experiments performed in this study demonstrated that extending the input QUS parametric images to include the tumor margin in addition to the core enhances the performance of the model in response prediction. Further, whereas the PDA maps demonstrated considerable contribution of various regions of the QUS parametric images to the network's decision, the impact of the margin areas on the model's prediction was highlighted particularly in the MBF and EAC parametric images. These results are in agreement with observations of the previous studies in which the imaging-based characteristics of tumor margin were shown important in different diagnostic and prognostic applications [38], [62]–[64].

The RAN architecture demonstrated a better performance compared to the ResNet in deriving optimal feature maps from QUS parametric images for response prediction. Both architectures use residual modules to overcome the overfitting throughout their very deep layers. The RAN architecture also utilizes attention modules that potentially facilitate feature optimization.

Specifically, the attention module enables the network to focus on significant and influential regions of images while extracting the feature maps. The observations of this study imply that the attention modules in the RAN architecture have been successful in identifying the important regions of the QUS parametric maps for response prediction.

In conclusion, this study demonstrated that DCNN models can be adapted in the context of quantitative imaging for therapy response prediction. The results indicated a better performance of the attention-guided convolutional networks in deriving optimal quantitative features form QUS multi-parametric images. The deep learning models developed in this study could predict the survival-linked response of LABC patients to NAC before starting the treatment with a high sensitivity and specificity. Predicting the outcome of NAC at pre-treatment would help the clinicians to adjust ineffective treatment regimens for individual patients. The results obtained in this study are promising and encourage further investigations using other DCNN architectures with the data acquired from larger (multi-institutional) cohorts of patients to evaluate the robustness of the methodologies in clinic.

References

[1] H. Sung *et al.*, "Global cancer statistics 2020: GLOBOCAN estimates of incidence and mortality worldwide for 36 cancers in 185 countries," *CA. Cancer J. Clin.*, p. caac.21660, Feb. 2021, doi: 10.3322/caac.21660.

[2] F. Bray, J. Ferlay, I. Soerjomataram, R. L. Siegel, L. A. Torre, and A. Jemal, "Global cancer statistics 2018: GLOBOCAN estimates of incidence and mortality worldwide for 36 cancers in 185 countries," *CA. Cancer J. Clin.*, vol. 68, no. 6, pp. 394–424, Nov. 2018, doi: 10.3322/caac.21492.

[3] S. H. Giordano, "Update on Locally Advanced Breast Cancer," *Oncologist*, vol. 8, no. 6, pp. 521–530, Dec. 2003, doi: 10.1634/theoncologist.8-6-521.

[4] G. N. Hortobagyi, "Comprehensive management of locally advanced breast cancer.," *Cancer*, vol. 66, no. 6 Suppl, pp. 1387–91, Sep. 1990, doi: 10.1002/1097-0142(19900915)66:14+<1387::aid-cncr2820661414>3.0.co;2-i.

[5] S. J. Cleator, A. Makris, S. E. Ashley, R. Lal, and T. J. Powles, "Good clinical response of breast cancers to neoadjuvant chemoendocrine therapy is associated with improved overall survival.," *Ann. Oncol. Off. J. Eur. Soc. Med. Oncol.*, vol. 16, no. 2, pp. 267–72, Feb. 2005, doi: 10.1093/annonc/mdi049.

[6] V. Guarneri *et al.*, "Prognostic value of pathologic complete response after primary chemotherapy in relation to hormone receptor status and other factors," *J. Clin. Oncol.*, vol. 24, no. 7, pp. 1037–1044, Mar. 2006, doi: 10.1200/JCO.2005.02.6914.

[7] B. T. Hennessy *et al.*, "Outcome after pathologic complete eradication of cytologically proven breast cancer axillary node metastases following primary chemotherapy," *J. Clin. Oncol.*, vol. 23, no. 36, pp. 9304–9311, 2005, doi: 10.1200/JCO.2005.02.5023.

[8] J. B. Nikas, W. C. Low, and P. A. Burgio, "Prognosis of treatment response (pathological complete response) in breast cancer," *Biomark. Insights*, vol. 7, pp. 59–70, May 2012, doi: 10.4137/BMI.S9387.

[9] B. Fisher *et al.*, "Effect of preoperative chemotherapy on the outcome of women with operable breast cancer," *J. Clin. Oncol.*, vol. 16, no. 8, pp. 2672–2685, 1998, doi: 10.1200/JCO.1998.16.8.2672.

[10] "Update on locally advanced breast cancer. - PubMed - NCBI." [Online]. Available: https://www.ncbi.nlm.nih.gov/pubmed/14657530. [Accessed: 12-May-2020].

[11] D. Sethi, R. Sen, J. Sen, S. Parshad, S. Khetarpal, and M. Garg, "Histopathologic changes following neoadjuvant chemotherapy in various malignancies," *Int. J. Appl. Basic Med. Res.*, vol. 2, no. 2, p. 111, 2012, doi: 10.4103/2229-516x.106353.

[12] S. Chuthapisith, J. M. Eremin, M. El-Sheemy, and O. Eremin, "Neoadjuvant chemotherapy in women with large and locally advanced breast cancer: Chemoresistance and prediction of response to drug therapy," *Surgeon*, vol. 4, no. 4. Edinburgh University Press, pp. 211–219, 01-Aug-2006, doi: 10.1016/S1479-666X(06)80062-4.

[13] W. Haque, V. Verma, S. Hatch, V. Suzanne Klimberg, E. Brian Butler, and B. S. Teh,

"Response rates and pathologic complete response by breast cancer molecular subtype following neoadjuvant chemotherapy," *Breast Cancer Res. Treat.*, vol. 170, no. 3, pp. 559–567, Aug. 2018, doi: 10.1007/s10549-018-4801-3.

[14] T. Byrski *et al.*, "Pathologic complete response rates in young women with BRCA1-positive breast cancers after neoadjuvant chemotherapy," *J. Clin. Oncol.*, vol. 28, no. 3, pp. 375–379, Jan. 2010, doi: 10.1200/JCO.2008.20.7019.

[15] K. Brindle, "New approaches for imaging tumour responses to treatment," *Nature Reviews Cancer*, vol. 8, no. 2. pp. 94–107, Feb-2008, doi: 10.1038/nrc2289.

[16] G. von Minckwitz *et al.*, "S3-2: Neoadjuvant Chemotherapy Adapted by Interim Response Improves Overall Survival of Primary Breast Cancer Patients – Results of the GeparTrio Trial.," in *Cancer Research*, 2011, vol. 71, no. 24 Supplement, pp. S3-2-S3-2, doi: 10.1158/0008-5472.sabcs11-s3-2.

[17] G. Von Minckwitz *et al.*, "Neoadjuvant vinorelbine-capecitabine versus docetaxel-doxorubicin- cyclophosphamide in early nonresponsive breast cancer: Phase III randomized gepartrio trial," *J. Natl. Cancer Inst.*, vol. 100, no. 8, pp. 542–551, Apr. 2008, doi: 10.1093/jnci/djn085.

[18] J. Mamou and M. L. Oelze, *Quantitative ultrasound in soft tissues*. Springer Netherlands, 2013.

[19] E. J. Feleppa *et al.*, "Typing of prostate tissue by ultrasonic spectrum analysis," *IEEE Trans. Ultrason. Ferroelectr. Freq. Control*, vol. 43, no. 4, pp. 609–619, Jul. 1996, doi: 10.1109/58.503779.

[20] M. Yang, T. M. Krueger, J. G. Miller, and M. R. Holland, "Characterization of anisotropic myocardial backscatter using spectral slope, intercept and midband fit parameters," *Ultrason. Imaging*, vol. 29, no. 2, pp. 122–134, Apr. 2007, doi: 10.1177/016173460702900204.

[21] D. J. Coleman, F. L. Lizzi, R. H. Silverman, L. Helson, J. H. Torpey, and M. J. Rondeau, "A model for acoustic characterization of intraocular tumors.," *Invest. Ophthalmol. Vis. Sci.*, vol. 26, no. 4, pp. 545–50, Apr. 1985.

[22] H. Tadayyon, A. Sadeghi-Naini, L. Wirtzfeld, F. C. Wright, and G. Czarnota, "Quantitative ultrasound characterization of locally advanced breast cancer by estimation of its scatterer properties," *Med. Phys.*, vol. 41, no. 1, p. 012903, Jan. 2014, doi: 10.1118/1.4852875.

[23] H. Tadayyon, A. Sadeghi-Naini, and G. J. Czarnota, "Noninvasive characterization of locally advanced breast cancer using textural analysis of quantitative ultrasound parametric images," *Transl. Oncol.*, vol. 7, no. 6, pp. 759–767, 2014, doi: 10.1016/j.tranon.2014.10.007.

[24] A. Sadeghi-Naini *et al.*, "Quantitative ultrasound spectroscopic imaging for characterization of disease extent in prostate cancer patients," *Transl. Oncol.*, vol. 8, no. 1, pp. 25–34, Feb. 2015, doi: 10.1016/j.tranon.2014.11.005.

[25] A. Guimond *et al.*, "Quantitative ultrasonic tissue characterization as a new tool for continuous monitoring of chronic liver remodelling in mice," *Liver Int.*, vol. 27, no. 6, pp. 854–864, Aug. 2007, doi: 10.1111/j.1478-3231.2007.01493.x.

[26] B. Banihashemi, R. Vlad, B. Debeljevic, A. Giles, M. C. Kolios, and G. J. Czarnota, "Ultrasound imaging of apoptosis in tumor response: Novel preclinical monitoring of

photodynamic therapy effects," *Cancer Res.*, vol. 68, no. 20, pp. 8590–8596, Oct. 2008, doi: 10.1158/0008-5472.CAN-08-0006.

[27] R. M. Vlad, S. Brand, A. Giles, M. C. Kolios, and G. J. Czarnota, "Quantitative ultrasound characterization of responses to radiotherapy in cancer mouse models," *Clin. Cancer Res.*, vol. 15, no. 6, pp. 2067–2075, Mar. 2009, doi: 10.1158/1078-0432.CCR-08-1970.

[28] G. J. Czarnota *et al.*, "Tumor radiation response enhancement by acoustical stimulation of the vasculature," *Proc. Natl. Acad. Sci. U. S. A.*, vol. 109, no. 30, pp. E2033–E2041, Jul. 2012, doi: 10.1073/pnas.1200053109.

[29] A. Sadeghi-Naini *et al.*, "Low-frequency quantitative ultrasound imaging of cell death *in vivo*," *Med. Phys.*, vol. 40, no. 8, p. 082901, Jul. 2013, doi: 10.1118/1.4812683.

[30] H. Tadayyon *et al.*, "Quantitative ultrasound assessment of breast tumor response to chemotherapy using a multi-parameter approach," *Oncotarget*, vol. 7, no. 29, pp. 45094–45111, Jul. 2016, doi: 10.18632/oncotarget.8862.

[31] L. Sannachi *et al.*, "Non-invasive evaluation of breast cancer response to chemotherapy using quantitative ultrasonic backscatter parameters," *Med. Image Anal.*, vol. 20, no. 1, pp. 224–236, Feb. 2015, doi: 10.1016/j.media.2014.11.009.

[32] A. Sadeghi-Naini *et al.*, "Quantitative ultrasound evaluation of tumor cell death response in locally advanced breast cancer patients receiving chemotherapy," *Clin. Cancer Res.*, vol. 19, no. 8, pp. 2163–2173, Apr. 2013, doi: 10.1158/1078-0432.CCR-12-2965.

[33] D. DiCenzo *et al.*, "Quantitative ultrasound radiomics in predicting response to neoadjuvant chemotherapy in patients with locally advanced breast cancer: Results from multi-institutional study," *Cancer Med.*, vol. 9, no. 16, pp. 5798–5806, Aug. 2020, doi: 10.1002/cam4.3255.

[34] A. Sadeghi-Naini *et al.*, "Conventional frequency ultrasonic biomarkers of cancer treatment response in vivo," *Transl. Oncol.*, vol. 6, no. 3, pp. 234–243, 2013, doi: 10.1593/tlo.12385.

[35] A. Sadeghi-Naini *et al.*, "Chemotherapy-Response Monitoring of Breast Cancer Patients Using Quantitative Ultrasound-Based Intra-Tumour Heterogeneities," *Sci. Rep.*, vol. 7, no. 1, Dec. 2017, doi: 10.1038/s41598-017-09678-0.

[36] A. Sadeghi-Naini *et al.*, "Early prediction of therapy responses and outcomes in breast cancer patients using quantitative ultrasound spectral texture," *Oncotarget*, vol. 5, no. 11, pp. 3497–3511, 2014, doi: 10.18632/oncotarget.1950.

[37] A. Dasgupta *et al.*, "Quantitative ultrasound radiomics using texture derivatives in prediction of treatment response to neo-adjuvant chemotherapy for locally advanced breast cancer," *Oncotarget*, vol. 11, no. 42, pp. 3782–3792, Oct. 2020, doi: 10.18632/oncotarget.27742.

[38] H. Tadayyon *et al.*, "A priori Prediction of Neoadjuvant Chemotherapy Response and Survival in Breast Cancer Patients using Quantitative Ultrasound," *Sci. Rep.*, vol. 7, Apr. 2017, doi: 10.1038/srep45733.

[39] D. Shen, G. Wu, and H.-I. Suk, *Deep Learning in Medical Image Analysis*. Elsevier, 2017.

[40] G. Litjens *et al.*, "A survey on deep learning in medical image analysis," *Medical Image Analysis*, vol. 42. Elsevier B.V., pp. 60–88, 01-Dec-2017, doi: 10.1016/j.media.2017.07.005.

[41] I. Goodfellow, Y. Bengio, A. Courville, and Y. Bengio, “Deep learning,” 2016, doi: 10.4258/hir.2016.22.4.351.

[42] K. Ravichandran, N. Braman, A. Janowczyk, and A. Madabhushi, “A deep learning classifier for prediction of pathological complete response to neoadjuvant chemotherapy from baseline breast DCE-MRI,” in *Medical Imaging 2018: Computer-Aided Diagnosis*, 2018, vol. 10575, p. 11, doi: 10.1117/12.2294056.

[43] Y. Qu, H. Zhu, K. Cao, X. Li, M. Ye, and Y. Sun, “Prediction of pathological complete response to neoadjuvant chemotherapy in breast cancer using a deep learning (DL) method,” *Thorac. Cancer*, vol. 11, no. 3, pp. 651–658, Mar. 2020, doi: 10.1111/1759-7714.13309.

[44] R. Ha *et al.*, “Prior to Initiation of Chemotherapy, Can We Predict Breast Tumor Response? Deep Learning Convolutional Neural Networks Approach Using a Breast MRI Tumor Dataset,” *J. Digit. Imaging*, vol. 32, no. 5, pp. 693–701, Oct. 2019, doi: 10.1007/s10278-018-0144-1.

[45] M. Byra, H. Piotrzkowska-Wroblewska, K. Dobruch-Sobczak, and A. Nowicki, “Combining Nakagami imaging and convolutional neural network for breast lesion classification,” in *IEEE International Ultrasonics Symposium, IUS*, 2017, pp. 1–4, doi: 10.1109/ULTSYM.2017.8092154.

[46] F. Wang *et al.*, “Residual Attention Network for Image Classification,” *Proc. - 30th IEEE Conf. Comput. Vis. Pattern Recognition, CVPR 2017*, vol. 2017-January, pp. 6450–6458, Apr. 2017.

[47] K. He, X. Zhang, S. Ren, and J. Sun, “Deep residual learning for image recognition,” in *Proceedings of the IEEE Computer Society Conference on Computer Vision and Pattern Recognition*, 2016, vol. 2016-December, pp. 770–778, doi: 10.1109/CVPR.2016.90.

[48] E. A. A. Eisenhauer *et al.*, “New response evaluation criteria in solid tumours: Revised RECIST guideline (version 1.1),” no. 2, pp. 228–247, Jan. 2009, doi: 10.1016/j.ejca.2008.10.026.

[49] K. N. Ogston *et al.*, “A new histological grading system to assess response of breast cancers to primary chemotherapy: prognostic significance and survival,” *The Breast*, vol. 12, no. 5, pp. 320–327, Oct. 2003, doi: 10.1016/S0960-9776(03)00106-1.

[50] Y. Labyed, T. A. Bigelow, and B. L. McFarlin, “Estimate of the attenuation coefficient using a clinical array transducer for the detection of cervical ripening in human pregnancy,” *Ultrasonics*, vol. 51, no. 1, pp. 34–39, Jan. 2011, doi: 10.1016/j.ultras.2010.05.005.

[51] L. X. Yao, J. A. Zagzebski, and E. L. Madsen, “Backscatter coefficient measurements using a reference phantom to extract depth-dependent instrumentation factors,” *Ultrason. Imaging*, vol. 12, no. 1, pp. 58–70, Jan. 1990, doi: 10.1016/0161-7346(90)90221-i.

[52] F. L. Lizzi *et al.*, “Comparison of theoretical scattering results and ultrasonic data from clinical liver examinations,” *Ultrasound Med. Biol.*, vol. 14, no. 5, pp. 377–385, 1988.

[53] M. F. Insana, R. F. Wagner, D. G. Brown, and T. J. Hall, “Describing small-scale structure in random media using pulse-echo ultrasound,” *J. Acoust. Soc. Am.*, vol. 87, no. 1, pp. 179–92, Jan. 1990.

[54] M. L. Oelze, W. D. O’Brien, J. P. Blue, and J. F. Zachary, “Differentiation and

characterization of rat mammary fibroadenomas and 4T1 mouse carcinomas using quantitative ultrasound imaging," *IEEE Trans. Med. Imaging*, vol. 23, no. 6, pp. 764–771, Jun. 2004, doi: 10.1109/TMI.2004.826953.

[55] M. F. Insana and T. J. Hall, "Parametric ultrasound imaging from backscatter coefficient measurements: image formation and interpretation.," *Ultrason. Imaging*, vol. 12, no. 4, pp. 245–67, Oct. 1990.

[56] D. P. Kingma and J. L. Ba, "Adam: A method for stochastic optimization," in *3rd International Conference on Learning Representations, ICLR 2015 - Conference Track Proceedings*, 2015.

[57] L. M. Zintgraf, T. S. Cohen, T. Adel, and M. Welling, "Visualizing Deep Neural Network Decisions: Prediction Difference Analysis," *5th Int. Conf. Learn. Represent. ICLR 2017 - Conf. Track Proc.*, Feb. 2017.

[58] L. Sannachi *et al.*, "Response monitoring of breast cancer patients receiving neoadjuvant chemotherapy using quantitative ultrasound, texture, and molecular features," *PLoS One*, vol. 13, no. 1, p. e0189634, Jan. 2018, doi: 10.1371/journal.pone.0189634.

[59] M. Byra, A. Nowicki, H. Wróblewska-Piotrzkowska, and K. Dobruch-Sobczak, "Classification of breast lesions using segmented quantitative ultrasound maps of homodyned K distribution parameters," *Med. Phys.*, vol. 43, no. 10, pp. 5561–5569, Oct. 2016, doi: 10.1118/1.4962928.

[60] J. Wu, G. Gong, Y. Cui, and R. Li, "Intratumor partitioning and texture analysis of dynamic contrast-enhanced (DCE)-MRI identifies relevant tumor subregions to predict pathological response of breast cancer to neoadjuvant chemotherapy," *J. Magn. Reson. Imaging*, vol. 44, no. 5, pp. 1107–1115, Nov. 2016, doi: 10.1002/jmri.25279.

[61] A. Sadeghi-Naini *et al.*, "Early detection of chemotherapy-refractory patients by monitoring textural alterations in diffuse optical spectroscopic images," *Med. Phys.*, vol. 42, no. 11, pp. 6130–6146, Nov. 2015, doi: 10.1118/1.4931603.

[62] E. Karami *et al.*, "Quantitative MRI Biomarkers of Stereotactic Radiotherapy Outcome in Brain Metastasis," *Sci. Rep.*, vol. 9, no. 1, p. 19830, Dec. 2019, doi: 10.1038/s41598-019-56185-5.

[63] P. M. Lamb, N. M. Perry, S. J. Vinnicombe, and C. A. Wells, "Correlation between ultrasound characteristics, mammographic findings and histological grade in patients with invasive ductal carcinoma of the breast," *Clin. Radiol.*, vol. 55, no. 1, pp. 40–44, 2000, doi: 10.1053/crad.1999.0333.

[64] A. M. Fowler, D. A. Mankoff, and B. N. Joe, "Imaging Neoadjuvant Therapy Response in Breast Cancer," *Radiology*, vol. 285, no. 2, pp. 358–375, Nov. 2017, doi: 10.1148/radiol.2017170180.

Chapter 4

Conclusion and Future Works

4.1. Discussion and Conclusion

In this thesis project, two novel approaches were investigated to predict breast cancer response to NAC prior to start of treatment using multi-parametric QUS imaging. The required data for analytical development, optimization, and evaluation of the methodologies in this project were acquired from 181 patients diagnosed with locally advanced breast cancer and planned for NAC followed by surgery. The QUS multi-parametric images were generated for these patients using the ultrasound radiofrequency (RF) data acquired before the start of treatment.

In the first approach, QUS multi-parametric images of the breast tumors were segmented into 3 regions using a modified version of HMRF-EM algorithm. Several features including SNR, mean-value, mean-value difference, and proportion area were extracted from the multi-parametric maps within the identified intra-tumor regions and tumor margin. After calculating the features for each tumor by averaging over the entire tumor volume, the derived 56 features were pruned into four features through a multi-step feature selection process to construct an optimal biomarker for response prediction. The developed biomarkers were used for response prediction using conventional machine learning method. The results indicated that applying AdaBoost decision tree model on developed features could predict the tumor response with an accuracy of 85.4% and an AUC of 0.89. The results demonstrated that considering characteristics of intra-tumor regions identified on the QUS multi-parametric images can improve the accuracy of pretreatment response prediction model compared to considering only characteristics of whole tumor. In addition, survival analysis indicated that there were statistically significant differences between the survival

rate of the responders and non-responders identified based on both the standard clinical criteria and the model predictions.

In the second approach, the capability of deep convolutional neural networks were investigated in predicting breast tumor response to NAC. The developed deep learning framework comprised a deep convolutional network as the backbone feature extractor followed by a fully-connected network for response prediction. For feature extraction, different network architectures including the ResNet and RAN were explored. 256 features were extracted from the multi-parametric images at each imaging plane using the deep convolutional models. Each tumor's features were obtained by averaging the feature vectors associated with its all imaging cross-sections. The average feature vectors were fed into the fully-connected network for response prediction. Evaluation results on the independent test indicated that the developed model inputting the extended parametric images of the tumor core and margin with the RAN as its feature extractor was able to predict the treatment response with an accuracy of 88%, a sensitivity of 92%, a specificity of 70%, and an AUC of 0.86. Also, the survival analysis showed that this model could differentiate the high-risk patients with relatively poor survival rate, as a statistically significant difference was observed between the survival curves of the patients predicted to be responder versus non-responder.

Response to NAC has demonstrated a high correlation to the patient survival [1][2]. However, up to 40% of LABC patients do not respond to NAC, and complete pathological response is limited to only 10-30% of the patients [3]–[6]. Therefore, it is crucial to identify the patients that do not even show a partial response to NAC as soon as possible. Other patient stratifications to differentiate partial versus complete pathological response to NAC is also very important and can be performed in parallel with non-responder detection or as a subsequent step. Early response prediction facilitates treatment adjustments for individual patients and even a switch to more

effective and salvage treatments before it is potentially late. Some available options of therapy adjustments/alteration for patients with minimal response to a standard treatment may include modifying the regimen, dose and/or sequence of treatment options. A personalized strategy in cancer treatment can potentially lead to higher treatment responsiveness, improved disease-free survival rates, better quality of life, and avoiding ineffective expensive treatment for patients. The results obtained in this study demonstrated the promising potential of QUS multi-parametric imaging in breast tumor response prediction when coupled with conventional machine learning methods and deep convolutional neural networks, and provided some ideas that can be pursued in future studies.

4.2. Future Works

In future, this study can be extended in several paths. Increasing the size of patient cohorts and including multi-institutional data can help to evaluate further the efficacy and robustness of the proposed methodologies. Also, providing more training data to the developed models can improve the generalizability and performance of the models. Especially deep learning models that have millions of parameters to be optimized requires large training datasets to achieve sufficient performance in real-world scenarios [7]. Therefore, incorporating larger datasets is expected to enhance the performance of the deep learning models developed in this project, and enable researchers to explore larger, more complex and potentially more powerful architectures in this application [8].

Another path of research that can be followed in future is investigating higher-order features including textural features of intra-tumor regions for response prediction [9], [10]. It has been

shown in several studies that textural features of QUS parametric images have high correlation with pathological outcome at the end of treatment [9], [11], [12]. Also, capability of combining textural features with mean-value and SNR parameters in parametric images of intra-tumor regions can be assessed in future studies. Also, exploring other methods for tumor segmentation and response classification can be considered in upcoming research [13], [14].

Nowadays, the field of deep learning is growing fast, and new state-of-art architectures in field of image processing are being introduced frequently [15], [16]. Concepts such as transformers and attention are getting more popular and they are transforming this field [17]. Also, stronger hardware and access to more powerful GPUs will enable exploiting larger and more complicated models. Therefore, in future these models can be explored and applied on QUS images for different tissue characterization applications [13]. Also, customizing the existing models for such applications through modifying and optimizing the network layers can be explored in future studies.

References

[1] L. M. Spring *et al.*, "Pathologic Complete Response after Neoadjuvant Chemotherapy and Impact on Breast Cancer Recurrence and Survival: A Comprehensive Meta-analysis," *Clin. Cancer Res.*, vol. 26, no. 12, pp. 2838–2848, Jun. 2020, doi: 10.1158/1078-0432.CCR-19-3492.

[2] A. Romero *et al.*, "Correlation between response to neoadjuvant chemotherapy and survival in locally advanced breast cancer patients," *Ann. Oncol.*, vol. 24, no. 3, pp. 655–661, 2013, doi: 10.1093/annonc/mds493.

[3] D. Sethi, R. Sen, S. Parshad, J. Sen, S. Khetarpal, and M. Garg, "Histopathologic changes following neoadjuvant chemotherapy in locally advanced breast cancer," *Indian J. Cancer*, vol. 50, no. 1, p. 58, 2013, doi: 10.4103/0019-509X.112301.

[4] S. Chuthapisith, J. M. Eremin, M. El-Sheemy, and O. Eremin, "Neoadjuvant chemotherapy in women with large and locally advanced breast cancer: Chemoresistance and prediction of response to drug therapy," *Surgeon*, vol. 4, no. 4. Edinburgh University Press, pp. 211–219, 01-Aug-2006, doi: 10.1016/S1479-666X(06)80062-4.

[5] G. N. Hortobagyi, "Comprehensive management of locally advanced breast cancer.," *Cancer*, vol. 66, no. 6 Suppl, pp. 1387–91, Sep. 1990, doi: 10.1002/1097-0142(19900915)66:14.

[6] S. H. Giordano, "Update on Locally Advanced Breast Cancer," *Oncologist*, vol. 8, no. 6, pp. 521–530, Dec. 2003, doi: 10.1634/theoncologist.8-6-521.

[7] J. Yim, D. Joo, J. Bae, and J. Kim, "A gift from knowledge distillation: Fast optimization, network minimization and transfer learning," in *Proceedings - 30th IEEE Conference on Computer Vision and Pattern Recognition, CVPR 2017*, 2017, vol. 2017-January, pp. 7130–7138, doi: 10.1109/CVPR.2017.754.

[8] C. Sun, A. Shrivastava, S. Singh, and A. Gupta, "Revisiting Unreasonable Effectiveness of Data in Deep Learning Era," *Proc. IEEE Int. Conf. Comput. Vis.*, vol. 2017-October, pp. 843–852, Jul. 2017.

[9] A. Sadeghi-Naini *et al.*, "Early prediction of therapy responses and outcomes in breast cancer patients using quantitative ultrasound spectral texture," *Oncotarget*, vol. 5, no. 11, pp. 3497–3511, 2014, doi: 10.18632/oncotarget.1950.

[10] L. Sannachi *et al.*, "Response monitoring of breast cancer patients receiving neoadjuvant chemotherapy using quantitative ultrasound, texture, and molecular features," *PLoS One*, vol. 13, no. 1, p. e0189634, Jan. 2018, doi: 10.1371/journal.pone.0189634.

[11] A. Sadeghi-Naini *et al.*, "Conventional frequency ultrasonic biomarkers of cancer treatment response in vivo," *Transl. Oncol.*, vol. 6, no. 3, pp. 234–243, 2013, doi: 10.1593/tlo.12385.

[12] A. Sadeghi-Naini *et al.*, "Chemotherapy-Response Monitoring of Breast Cancer Patients Using Quantitative Ultrasound-Based Intra-Tumour Heterogeneities," *Sci. Rep.*, vol. 7, no. 1, Dec. 2017, doi: 10.1038/s41598-017-09678-0.

[13] R. Yang and Y. Yu, "Artificial Convolutional Neural Network in Object Detection and

Semantic Segmentation for Medical Imaging Analysis," *Front. Oncol.*, vol. 11, p. 638182, Mar. 2021, doi: 10.3389/fonc.2021.638182.

[14] N. Sharma *et al.*, "Automated medical image segmentation techniques," *Journal of Medical Physics*, vol. 35, no. 1. Wolters Kluwer -- Medknow Publications, pp. 3–14, 01-Jan-2010, doi: 10.4103/0971-6203.58777.

[15] I. Freeman, L. Roese-Koerner, and A. Kummert, "EffNet: An Efficient Structure for Convolutional Neural Networks," *Proc. - Int. Conf. Image Process. ICIP*, pp. 6–10, Jan. 2018.

[16] H. Touvron, M. Cord, M. Douze, F. Massa, A. Sablayrolles, and H. Jégou, "Training data-efficient image transformers & distillation through attention," *arXiv*, Dec. 2020.

[17] A. Dosovitskiy *et al.*, "An Image is Worth 16x16 Words: Transformers for Image Recognition at Scale," Oct. 2020.

Appendix A

Supplementary Figures and Tables

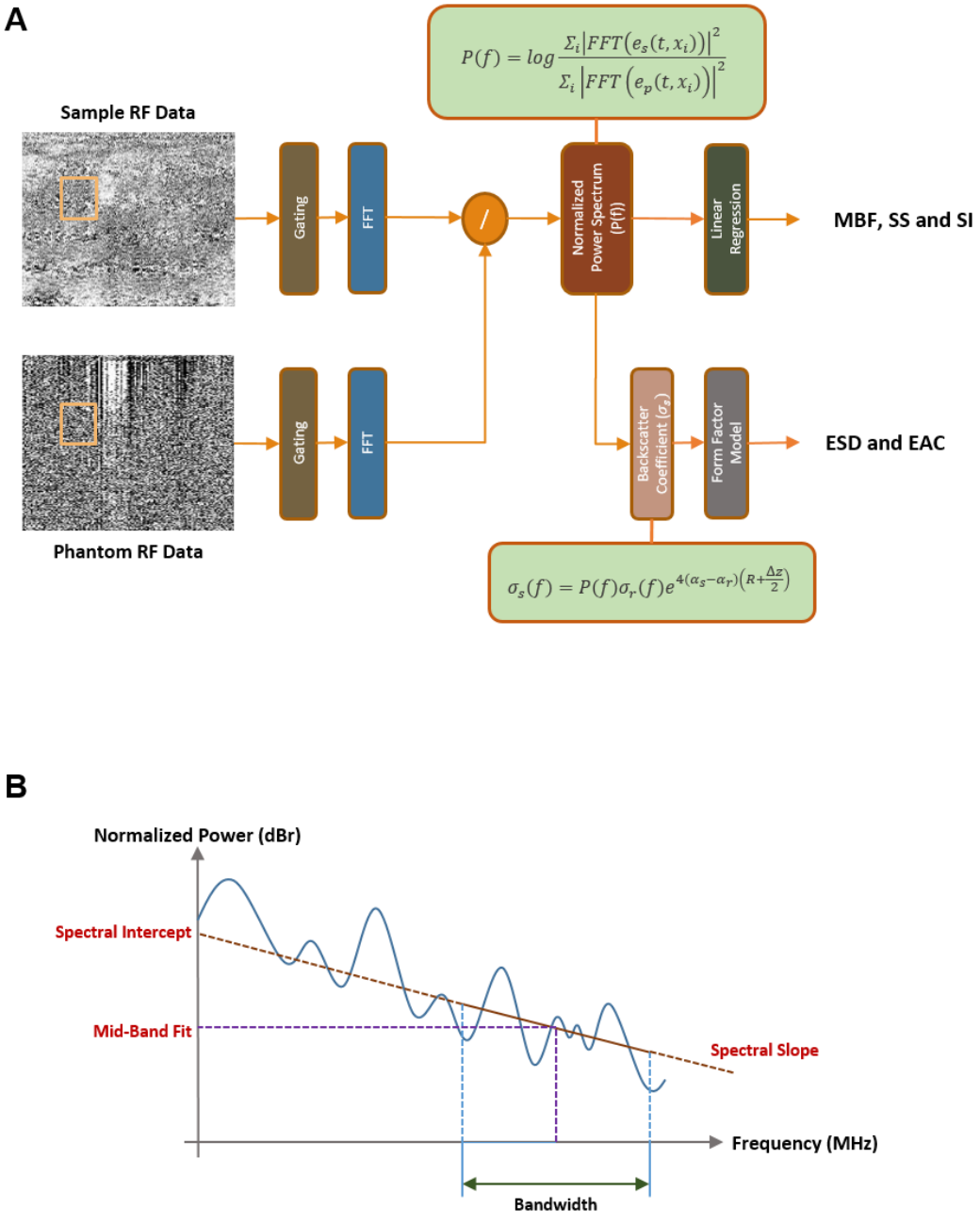

Figure A1.1. A: schematic diagram showing different steps to calculate QUS parameters for a window sliding through a frame of US RF data in the process of parametric map generation; B: descriptive image of linear regression analysis applied on the normalized power spectrum to obtain the mid-band fit (MBF), spectral intercept (SI), and the spectral slope (SS) parameters.

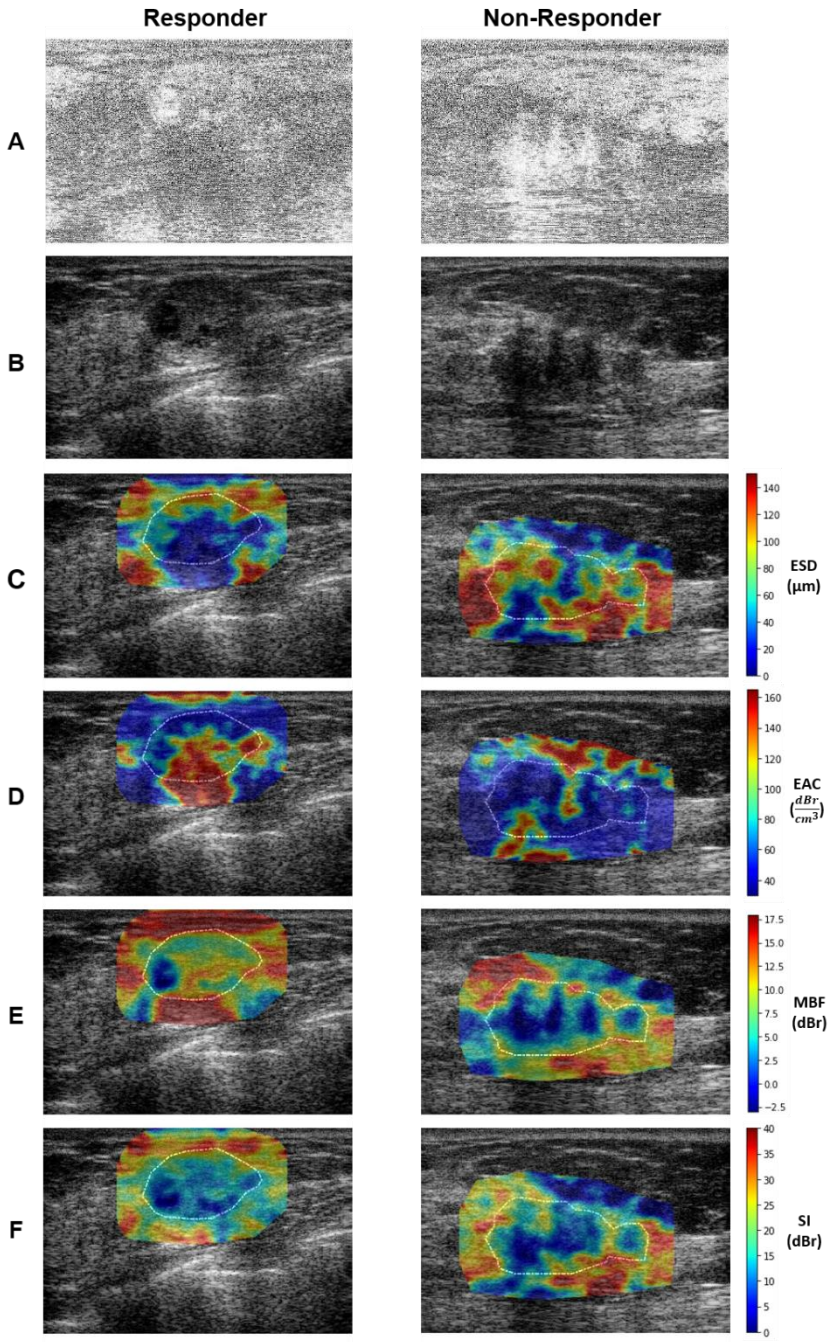

Figure A1.2. Ultrasound RF data (A), B-mode images (B), and QUS parametric images of ESD (C), EAC (D), MBF (E), and SI (F) obtained for a representative responder and non-responder to NAC. The tumor core has been outlined with white dashed line on the parametric images.

Table A1.1. Extended table 2.2 with the positive prediction value (PPV) and negative prediction value (NPV) for different experiments presented in Chapter 2

Feature Set	**Test Set**					
	Acc	**Sen**	**Spec**	**AUC**	**PPV**	**NPV**
Clinical Features: Tumor Size, ER/PR, HER2, Age	69.1%	40.0%	80.0%	0.6	42.9%	78.0%
Unsegmented Core: $M_C^{MBF}, SNR_C^{EAC}, SNR_C^{SI}, M_C^{SI}$	74.5%	66.6%	77.5%	0.79	52.6%	86.1%
Unsegmented Core and Margin: $M_C^{MBF}, SNR_m^{SI}, SNR_C^{EAC}, M_C^{SI}$	76.4%	66.6%	80.0%	0.76	55.6%	86.4%
Intra-Tumor Regions and Margin: $SNR_1^{SI}, SNR_m^{ESD}, M_{3-1}^{EAC}, M_1^{MBF}$	85.4%	86.6%	85.0%	0.89	68.4%	94.4%

Table A1.2. Extended table 3.2 with the positive prediction value (PPV) and negative prediction value (NPV) for different models presented in Chapter 3

Model	**Feature Network**	**Input Parametric Maps**	**Test Set**					
			Acc	**Spec**	**Sen**	**AUC**	**PPV**	**NPV**
1	ResNet	Core	80%	82.5%	70%	0.77	50%	91.7%
2	ResNet	Core + Margin	82%	85%	70%	0.83	53.8%	91.9%
3	RAN	Core	80%	80%	80%	0.82	50%	94.1%
4	RAN	Core + Margin	88%	92.5%	70%	0.86	70%	92.5%